Robust Polymer Electrolytes via Polymerization-Induced Microphase Separation

A DISSERTATION
SUBMITTED TO THE FACULTY OF THE GRADUATE SCHOOL
OF THE UNIVERSITY OF MINNESOTA
BY

Sujay A. Chopade

IN PARTIAL FULFILLMENT OF THE REQUIREMENTS
FOR THE DEGREE OF
DOCTOR OF PHILOSOPHY

Advised by:
Timothy P. Lodge
Marc A. Hillmyer

July, 2018

Acknowledgements

I would like to thank my advisors Professor Marc Hillmyer and Professor Tim Lodge for giving me the opportunity to work on a wide variety of projects and applications. They have always been approachable and patient especially during tough times. It has been a privilege to learn from both of them.

A part of the research in this thesis was done in close collaboration with Professor Phil Buhlmann and Evan Anderson, and I'm immensely grateful that they were willing to work with me. Evan, in particular, has been an excellent collaborator.

I am also grateful for the consistently friendly and collaborative culture of the Polymer Group. I would like to acknowledge the group members who have been generous with their time and always willingly participated in helpful discussions over the years. I am grateful to my mentors - Soonyong, Thomas, Jenny, Matt, Lucas who displayed saint-like patience, teaching me without hesitation. I am grateful to my friends in the lab for the wonderful time, softball games and fun conversations – Lindsay, Ralm, Annabelle, Guilhem, Angelika, Dan, Shuyi, Peter, Seyoung, En, Aaron, Ziang, Ceci, Boxin, Paul, Yuanchi, Andy, Rob; PIMS group – Stacey, Mike, Jon, Nick; my wonderful office neighbors – Wenjia, Julia, Aakriti, and Yaming. I had a great time working with Jesus and Mitsuo. A special mention to Julie, Teresa, Mollie, Jim, Letitia, CEMS and Chemistry office staff and Mrs. Lodge for all their help and consideration.

A big thanks to all my friends – Pranav, Abhinav, Chowdhary, Rohit, Nitish, Anurag, Biswa, Ami, Rishabh, Billi, Vikas, Shashank who provided me with wonderful and lifelong memories of the amazing time we spent together. Most importantly, I would like to thank my family who have always believed in me and supported me in every decision.

Dedications

To the fallen heroes and the bravehearts in the services.

Abstract

Polymer electrolyte membranes (PEMs) are polymeric matrices that facilitate efficient transport of charged species, and are critical components of various electrochemical devices, such as lithium (Li) ion batteries, flexible organic solar cells, and fuel cells. Irrespective of the application, the outstanding challenge in advancing PEM performance is to maximize the ionic conductivity while simultaneously addressing orthogonal mechanical properties, such as high modulus, toughness, or high-temperature stability. Nanostructured PEMs, such as block polymers selectively incorporating electrolytes into one of the domains, are capable of exhibiting the desired decoupled mechanical and conducting characteristics. This thesis details development of block polymer-based, robust, and high conducting PEMs targeted for specific applications, prepared via a versatile synthetic strategy–termed polymerization-induced microphase separation (PIMS). The PIMS route involves simultaneous growth and *in situ* crosslinking of the polystyrene (PS) block which kinetically arrests the emerging system in a co-continuous morphology that is locally correlated but does not exhibit long-range order. Chapter 2 discusses development and characterization of nanostructured PIMS PEMs with poly(ethylene oxide) (PEO) domains incorporating a protic ionic liquid. In addition to high proton conductivity, the PEMs exhibit high-temperature mechanical stability furnished by the cross-linked polystyrene (PS) scaffold, which is desirable for high-temperature, anhydrous fuel cell applications. Chapter 3 presents a design of robust PS-*b*-PEO PEMs based on the PIMS platform, incorporating a Li salt and succinonitrile plasticizer into the PEO domains. A systematic study of the PEM ionic conductivity demonstrated that network defects such as dead ends and isolated domains are rare in PIMS PEMs, and the PEMs manifest conducting nanochannels with long-range continuity. Finally, Chapter 4 details preparation of ready-to-use IL-based reference electrodes with a hydrophobic polymeric matrix. The solvent-

free, one-step design capitalized on another virtue of the PIMS strategy – the ease of processing a liquid reaction mixture, followed by *in situ* solidification to obtain solid PEMs. Throughout all this work, the goal is to better understand structure-property relationships in nanostructured PEMs in order to optimize the macroscopic performance in terms of conductivity and mechanical properties.

Table of Contents

List of Tables

List of Figures

Chapter 1 – Introduction

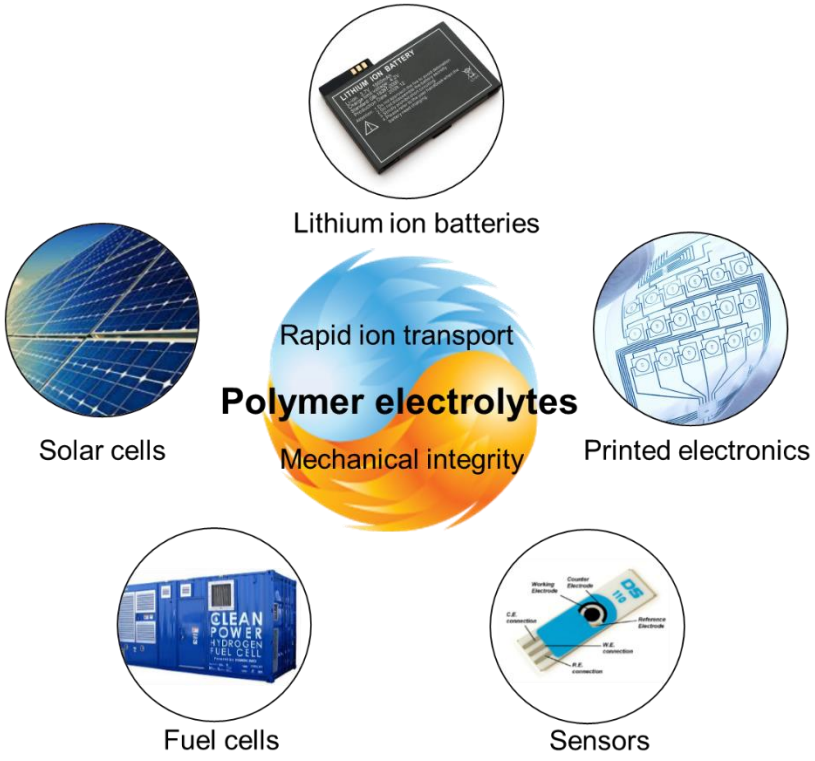

Polymer electrolytes employed in various electrochemical applications

The chapter introduces various aspects of polymer electrolytes and their applications. The chapter is organized as follows: the first section presents the role of polymer electrolyte membranes and the current status of lithium ion batteries and proton fuel cell membranes; the second section describes ion transport mechanisms in various homogeneous electrolytes; the third section elucidates the effects of morphology on ionic conductivity in nanostructured polymer electrolytes. The final section discusses various strategies employed to develop robust nanostructured polymer electrolyte membranes with bicontinuous morphologies.

1.1 Polymer Electrolytes

The advent of zero-emission hydrogen-powered cars like the Honda Clarity, emergence of private-sector space programs like SpaceX and Blue Origin, and the effort to increase power generation using renewable resources increase the demand for efficient and economical energy conversion and storage devices. This has prompted research efforts on proton exchange fuel cells and lithium ion batteries (LIBs), which have the highest energy densities amongst the known electrochemical storage systems.[1] The performance of both these technologies rely on polymer electrolyte membranes (PEMs) – polymeric matrices incorporating salts or liquid electrolytes. In some polymer electrolytes such as the perfluorosulfonic acid membranes used in fuel cells, one of the ions (the one not involved in energy-producing reactions) is tethered to the polymer backbone.

In electrochemical devices like fuel cells and LIBs, the PEMs facilitate ion transport between the electrodes. Since the ion transport through the PEM is the kinetic bottleneck compared to electrical conductivity in the external circuit, efforts have been devoted to the development of PEMs.[2] Irrespective of the application, the key challenge in advancing PEM performance is improving the ionic conductivity while simultaneously satisfying an orthogonal mechanical or thermal property (e.g., high modulus, elasticity, toughness, long-term creep resistance, or high temperature stability). In the light of this challenge, PEMs possessing nanoscale morphologies that allow independent control over the electrochemical properties and the structural integrity have received great attention.[3–12] The goal of this thesis is to develop a framework for building robust, nanostructured, high-performing polymer electrolytes targeted for specific applications. The following section discusses the role of PEMs in proton fuel cells and LIBs, the current status of PEMs, and the desired improvements.

Proton exchange fuel cells

The Gemini space program, was started in 1961 to develop space travel techniques to support the Apollo missions with the goal of landing man on the moon. The substitution of fuel cells for batteries as the prime source of electrical power was critical in allowing the long-duration space flights of Project Gemini.[13] In a proton exchange fuel cell (Figure 1.1a), the four major components are catalyst, cathode, anode, and the PEM sandwiched between the electrodes. At the anode-catalyst interface, protons are generated by the oxidation of the hydrogen fuel. The PEM facilitates the transport of the protons to the catalyst-cathode interface, where they react with oxygen to form water. The electrically insulating PEM separates the two electrodes and forces the electrons to travel through the outer circuit, thus converting the chemical energy stored in hydrogen into electricity. At present, most proton exchange fuel cells use a water-swollen, perfluorosulfonic acid (PFSA) polymer membrane (e.g., Nafion®, Figure 1.1b) as the PEM and platinum-based electrodes.[2,14] In humidified conditions, the sulfonic acid groups can dissociate, and the resultant hydronium cations conduct protons.

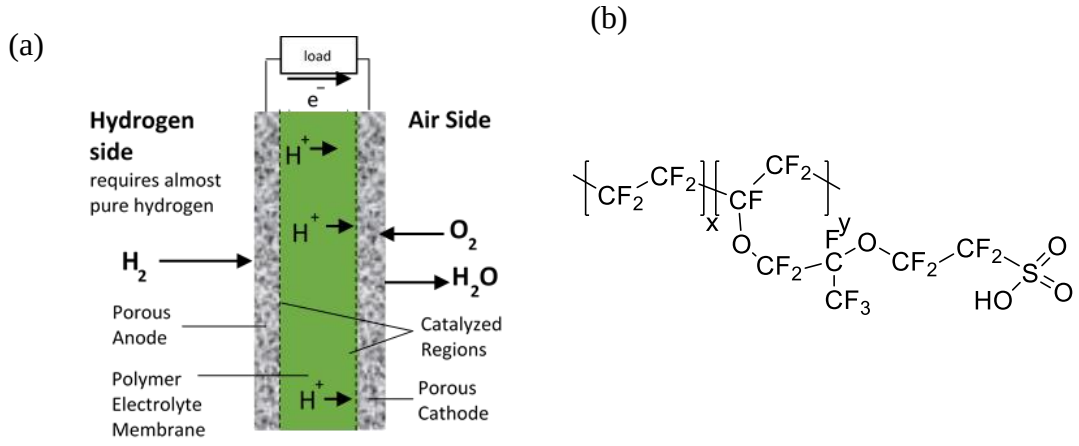

Figure 1.1: (a) Generic proton exchange membrane fuel cell. (b) Nafion® perfluorosulfonic acid (PFSA) polymer membrane.

The three most important transport properties for an electrolyte system are ionic conductivity, σ; ionic diffusion coefficient, D, and transference number (t^+ for a cation). For an electrolyte without a concentration gradient, σ is given by Nernst−Einstein equation:

$$\sigma = \frac{F^2}{RT}\left(z^+c^+D^+ + z^-c^-D^-\right) \tag{1.1}$$

where c^+ and c^- are the molar concentration of the cation and anion, respectively, z is the integer charge of the ion, F is Faraday's constant, R is the gas constant, and T is temperature. In the case of PFSA membranes, $D^- \approx 0$, since the anions are tethered to a high molar mass polymer backbone. Hydrated Nafion (water volume fraction ≈ 0.6) membranes exhibit a proton conductivity as high as 0.1 S/cm at 30 °C.[13] Another important parameter is the proton transference number (t^+), defined as the fraction of charge carried by the movement of protons and given by

$$t^+ = \frac{D^+}{D^+ + D^-} \tag{1.2}$$

For fuel cell applications, proton transference numbers approaching unity as observed in Nafion membranes are desirable, as only the transport of protons contributes to the current output.[15]

Some of the key issues associated with PFSA-based technologies include poor cathode performance and low tolerance to hydrogen fuel impurities, especially carbon monoxide (CO).[13,16,17] These limitations can be resolved by operating the fuel cell at elevated temperatures (100 °C to 200 °C),[16,17] which enhances the kinetics of electrode reactions. Likewise, the CO tolerance of the platinum electrode improves from 10 ppm at 80 °C to 30,000 ppm at 200 °C.[18] However, water-based PFSA membranes exhibit appreciable proton conductivity only under highly humidified conditions, which limits the upper operating temperature to around 80 °C.[17]

High-temperature fuel cell membranes

High temperature fuel cells require anhydrous proton conducting electrolytes. Phosphoric acid (PA) is one such proton conductor. Bulk PA partially self-dissociates (~ 15%) to form $H_4PO_4^+$ and $H_2PO_4^-$, giving rise to a high concentration of intrinsic protonic species.[19] Rapid proton transport via a hydrogen bonding network allows PA to exhibit a proton conductivity of 0.5 S/cm at 150 °C under anhydrous conditions.[16] The mechanism of proton transport in PA and other electrolytes is discussed in Section 1.2.

In the 1990s, PA-doped polybenzimidazole (PBI) membranes were first proposed as candidates for high temperature fuel cell polymer electrolytes (Figure 1.2).[16] The glassy PBI (glass transition temperature ≈ 425 °C) membrane acts as a proton acceptor in the PA/PBI system in addition to the role of host matrix polymer. PA/PBI systems exhibit high proton conductivity only at high acid loading (> 60% w/w).[16,20] In addition, Pt catalyst poisoning with PA prevents the operation at lower temperatures. Consequently, PA fuel cells operate at 200 °C. At this temperature, the PA/PBI system exhibits ionic conductivity ≈ 0.4-0.6 S/cm (PA content ≈ 65% w/w) and $t^+ \approx 0.98$.[16]

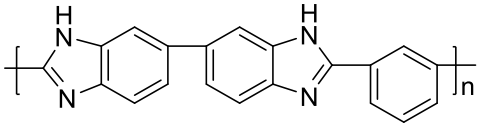

Polybenzimidazole (PBI)

Figure 1.2: Polybenzimidazole is able to complex with phosphoric acid to render a thermally stable proton-conducting polymer electrolyte.

Another class of anhydrous electrolytes with excellent thermal stability consists of ionic liquids. Ionic liquids (ILs) are molten salts with low melting temperatures (below 100 °C), exhibiting unique physicochemical properties such as negligible vapor pressure, non-flammability, a wide electrochemical window, and high ionic conductivity.[21–24] Noda and co-workers reported for the first time that thermally stable proton conducting or protic ILs can be prepared through neutralization reaction of a Brønsted acid and Brønsted base.[25]

For example, 1-ethylimidazolium bis(trifluoromethylsulfonyl)imide [HEIm][TFSI] (Figure 1.3) protic IL obtained with an equimolar mixture of 1-ethylimidazole (EIm) and bis(trifluoromethylsulfonyl)imide (HTFSI) acid exhibits high ionic conductivity (≈ 25 mS/cm at 120 °C) under non-humidified conditions, and is thermally stable up to 380 °C.[23,26] Therefore, mechanically robust, thermally stable PEMs incorporating protic ILs are a viable candidate for next generation high temperature fuel cells. This is the subject of Chapter 2.

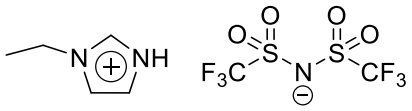

[EIm][TFSI]

Figure 1.3: Protic or proton conducting ionic liquid [HEIm][TFSI].

The above discussion focused on the proton conductivity and t^+ of the various fuel cell PEMs. However, in order to function as a proton exchange membrane in a high temperature fuel cell, an ideal PEM should also satisfy the following requisites – low gas permeability (low gas cross-over), chemical stability against peroxyl radical attack (•OH, •OOH), and exhibit facile electrode reactions (hydrogen oxidation reactions (HORs) and oxygen reduction reactions (ORRs)) at the electrode interface.[13,17,27–29]

Lithium ion batteries

In today's information-rich, mobile world, lithium ion batteries (LIBs) have become an integral part of our lives as key components in laptops, mobile devices and other personal electronics. LIBs are a popular choice for powering devices ranging from implantable medical devices to electrical vehicles due to desirable features including high energy densities, low self-discharge rates, high open-circuit potentials, and minimal memory effects.[30–32]

The construction of a LIB includes an electrolyte layer separating the cathode from the anode and providing Li^+ conducting pathways between the electrodes. Present technology

(Figure 1.4a) for a rechargeable LIB employs a Li-metal oxide cathode and a graphite anode. The electrolyte layer is composed of a liquid electrolyte of a Li salt and polar organic solvents like ethylene carbonate or propylene carbonate (Figure 1.4d).[30,33] The liquid electrolyte either swells a polymer membrane like polyacrylonitrile to form a gel electrolyte or resides in relatively large voids of a microporous polyolefin membrane (Celgard®, for instance) (Figure 1.4c).[34] Such systems exhibit ionic conductivities of order 1 mS/cm at 25 °C and lithium transference numbers (LTN) ≈ 0.4.[30] The above mentioned polymer/liquid electrolyte systems exhibit adequate mechanical robustness (modulus ≈ 1 kPa – 1 MPa) to prevent polymer creep when sandwiched between electrodes.[34]

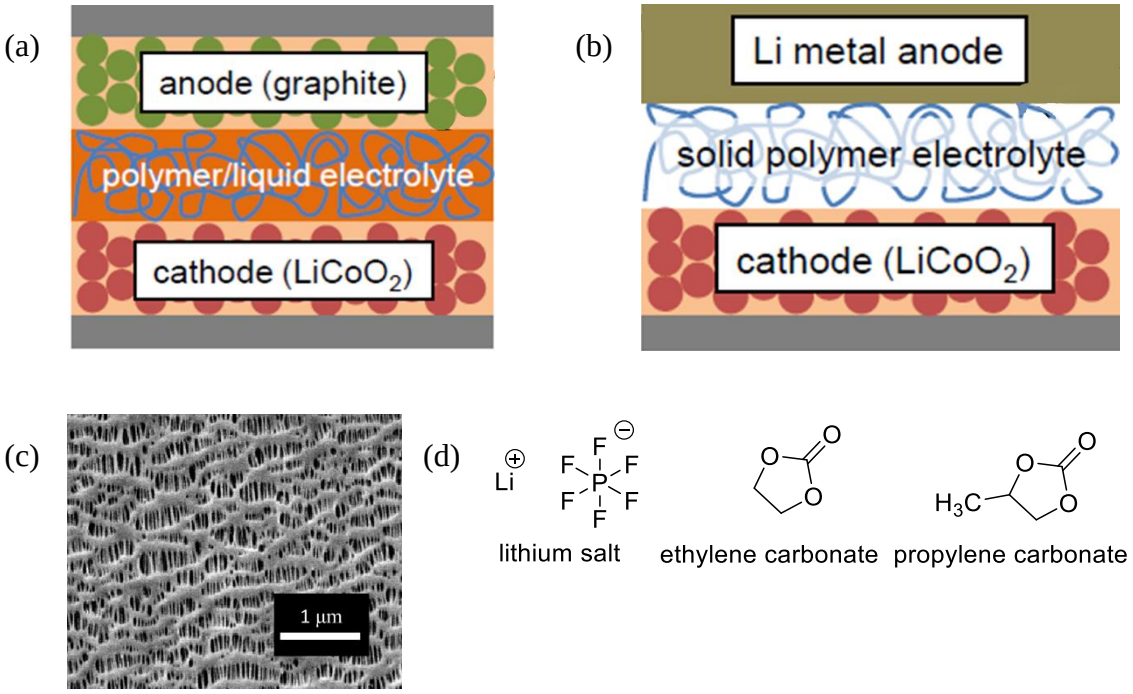

Figure 1.4: (a) Current design for lithium-ion batteries; (b) model lithium-ion battery with Li-metal anode and safer solid PEM; (c) microporous polyethylene membrane used as battery separator; (d) lithium salt ($LiPF_6$) and commercially used battery electrolytes – ethylene carbonate and propylene carbonate.

The use of flammable, volatile solvents in the current system gives rise to safety issues. For the next-generation LIBs, the goal is to build solvent-free, solid PEMs. Also, use of a Li metal anode in lieu of the currently used graphite anode has been extensively

investigated to increase energy density.[1,35,36] Unfortunately, during recharge cycles the Li metal anodes give rise to the formation of lithium metal dendrites that present serious safety hazards. Theoretical work by Monroe and Newman has shown that tuning the mechanical properties of PEMs may offer means to stop dendrite initiation and growth.[37–39] Studies indicated that if the intrinsic modulus of the PEMs is of the same order of magnitude as Li metal (1 GPa), the PEMs are stable against Li metal dendrite propagation.[40] These results combined with the conductivity data observed in commercial LIBs offer benchmark values to focus research efforts: a commercially viable solid PEM for LIBs should exhibit ionic conductivity in excess of 1 mS/cm and mechanical modulus of 1 GPa at 25 °C. PEMs also needs to be electrochemically stable, working with a highly oxidizing (>4V versus Li/Li^+) positive electrode material.[30]

Owing to their favorable electrochemical stability and ability to solvate Li salts, poly(ethylene oxide) (PEO) based materials are widely considered as promising candidates of polymer hosts in solid-state PEMs for LIBs.[41] Unfortunately, typical linear PEO/Li salt systems do not meet the mechanical robustness criteria and exbibit ionic conductivities in the range of 10^{-8} to 10^{-4} S/cm at room temperature.[41] Developing a nanostructured PEO-based PEM that satisfies the design criteria for the ionic conductivity and mechanical robustness is the subject of Chapter 3.

1.2 Homogeneous Electrolytes

This section discusses various single-phase, macroscopically homogeneous electrolyte systems that can be selectively incorporated into a nanostructured polymer framework to develop high conducting PEMs. This section elucidates the mechanism of ion transport in various homogeneous electrolyte systems such as ILs and PEO/Li salts.

Type I: Liquid Electrolytes

A. Acidic aqueous solutions

Sulfuric acid aqueous solution represents one of the most efficient ionic electrolytes. A 2 M solution exhibits the highest value of σ (≈ 0.6 S/cm at 25 °C) and high proton transference number ($t^+ \approx 0.8$).[11] In these systems, water molecules act as the base and are protonated to form hydronium (H_3O^+) cations. The proton transport is a combination of vehicular (migration of the hydronium cations) and Grotthuss or hopping mechanisms. The presence of hydrogen-bonding networks facilitates proton-exchange reactions between the hydronium cations and the water molecules; this rapid proton transport is called the Grotthuss or proton hopping mechanism.[42] The rapid Grotthuss mechanism allows these systems to exhibit high t^+, since anion transport occurs via vehicular (diffusion of anions) mechanism alone.

B. Lithium salts dissolved in organic solvents

At present, LIBs employ liquid electrolytes composed of Li salts and polar organic solvents like ethylene carbonate (EC) or propylene carbonate (PC) (Figure 1.4d).[43] In these systems, the use of Li salts with large, monovalent counter-anions like PF_6^- that reduce the lattice energy, and polar solvents (ε of EC ≈ 42), facilitates high concentrations of dissociated free Li^+.[11] However, in the absence of Grotthuss transport in EC/Li salt electrolytes, the slower vehicular mechanism ($D^+ \approx 3 \times 10^{-10}$ m^2/s) delivers $\sigma \approx 0.01$ S/cm at 25 °C, an order of magnitude lower than acidic aqueous solutions.[44] At a typical salt concentration of 1 M, EC/Li salt electrolytes exhibit lithium transference number (LTN) ≈ 0.4.[44]

C. Phosphoric acid

High proton conductivity of bulk phosphoric acid is attributed to its high degree of self-dissociation (~ 15%), which gives rise to a high concentration of intrinsic protonic species, and the amphoteric nature of the acid, i.e., it can act as a proton donor and an acceptor.[19] Specific hydrogen bond rearrangements in bulk phosphoric acid gives rise to Grotthuss-

type proton transfer mechanism.[19] Phosphoric acid is an ideal candidate for a high-temperature fuel cell electrolyte because of its unique physicochemical properties such as excellent proton conductivity under anhydrous conditions ($\sigma \approx 0.5$ S/cm at 150 °C), high proton transference number ($t^+ \approx 0.98$), and low volatility and stability at elevated temperatures.[16,45]

D. Ionic liquids

Ionic liquids (ILs) have received significant attention in multidisciplinary areas because of their unique physicochemical properties such as high ionic conductivity,[24,46] favorable chemical and thermal stability,[47] negligible vapor pressure, non-flammability, and a wide electrochemical window.[48,49] ILs are characterized by large constituents ions (Figure 1.5) with delocalized charges. The bulky nature of the ions impede crystallization, but results in slower diffusion coefficients ($D \approx 7 \times 10^{-11}$ m^2/s at 80 °C).[50] In contrast to the previous category of salts dissolved in organic solvents, ILs are composed entirely of ions and ion-aggregates (ion concentration ≈ 4 M) thus compensating for the lower diffusion coefficients and delivering appreciable ionic conductivity ($\sigma \approx 10^{-2}$ S/cm at 80 °C) and $t^+ \approx$ 0.46 in the case of 1-ethyl-3-methylimidazolium bis(trifluoromethylsulfonyl)imide [EMI][TFSI].[50]

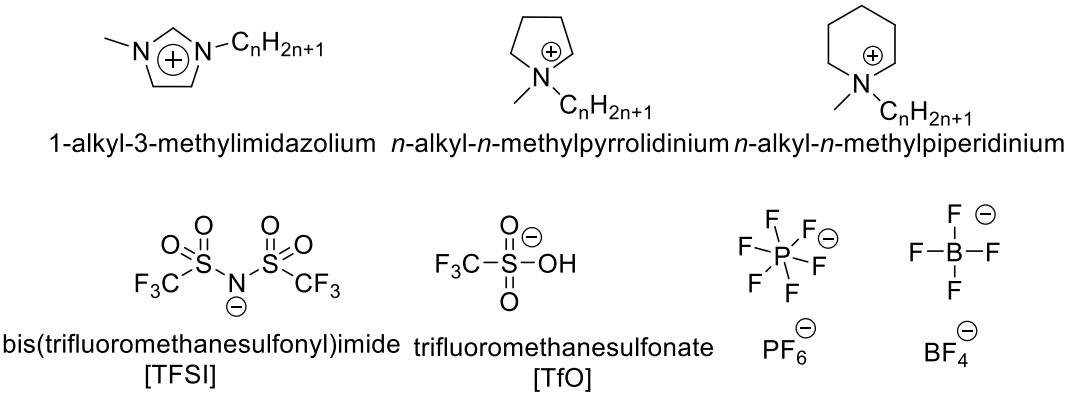

Figure 1.5: Ionic liquids: constituent cations and anions.

The virtually unlimited tunability of chemical structures (Figure 1.5) provides ILs with desired physicochemical properties. Alkylimidazolium-based [$C_n$mim] ionic liquids with bis(trifluoromethylsulphonyl)imide [TFSI] counter-anions are one of the most researched IL systems. This family of ILs is hydrophobic and exhibits high ionic conductivity owing to the plasticizing nature of the [TFSI] anion in which extremely electron-withdrawing CF_3SO_2 − groups are linked by flexible S–N–S bonds.[50,51] The delocalization of the ionic charges over the imidazolium ring and [TFSI] with multiple conformations results in low-lattice energy systems with high concentrations of free ions.[48,49] Favorable electrochemical properties of the ILs such as high ionic conductivity, high capacitance, and a wide electrochemical window have enabled their use as electrolytes in various applications including actuators, polymer gel electrolytes, supercapacitors, ion batteries, fuel cell membranes, sensors, printable plastic electronics, IL-based reference electrodes, and flexible displays.[48,49]

Proton conducting or protic ILs derived from Brønsted acid-base pairs have emerged as promising electrolytes for fuel cells operating at high temperatures and under anhydrous conditions.[5,15,22,23,52] As discussed earlier, equimolar [HEIm][TFSI] exhibits high ionic conductivity (≈ 25 mS/cm at 120 °C) and transference number ($t^+ \approx 0.6$).[23,26] For certain mixtures with excess base (EIm), the proton conductivity exceeds that of the equimolar mixture. In the base-rich compositions, proton conduction follows a combination of vehicular-type and proton-hopping or Grotthuss-type mechanisms (Figure 1.6).[22] For example, mixtures with [EIm]/[HTFSI] = 4/1 exhibit $\sigma \approx 50$ mS/cm at 120 °C and $t^+ \approx 0.72$.[22]

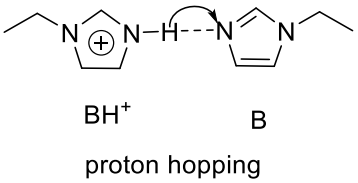

Figure 1.6: Proton hopping mechanism observed in non-stochiometric protic ILs.

Other fascinating physicochemical properties of ILs, such as negligible vapor pressure and large thermal and chemical stability has allowed ILs to be used in vacuum technologies, inorganic particle synthesis, and catalysis.[53] In addition to Coulombic interactions, the presence of directional interactions such as hydrogen bonding, and van der Waals interactions allow ILs to behave as an unusual solvent environment for low-solubility biopolymers, proteins, and as good dispersion media of carbon nanotubes, thus contributing to the field of advanced materials.[54] ILs with BF_4^- anions have been reported to exhibit significant solubility preference for CO_2 over other gases, presenting possibilities for inexpensive separation membranes and CO_2 sequestration.[21]

Type II: Polymer Electrolytes

This section discusses (a) polar polymers capable of dissolving Li salts, (b) homogeneous mixtures of polymers and ILs, and (c) polymerized IL systems.

A. Ion solvating polymers + Li salts

In 1973, Fenton et al. first reported the ionic conductivity of this class of dry polymer electrolytes – poly(ethylene oxide) (PEO) + Li salt mixtures.[55] Subsequently, interest in solvent-free polymer electrolytes intensified after Armand proposed to use the polyether/Li salt systems in lieu of gel electrolytes in Li-ion batteries.[56] In contrast to gel electrolytes, where the role of the polymer membrane is limited to providing mechanical support and acting as a container for the solvent, the ion motion in PEO/Li salt system is coupled to micro-Brownian polymer chain motion (Figure 1.7).

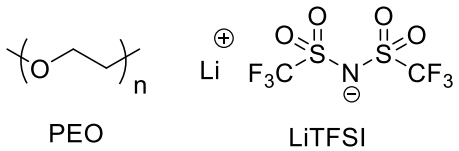

PEO LiTFSI

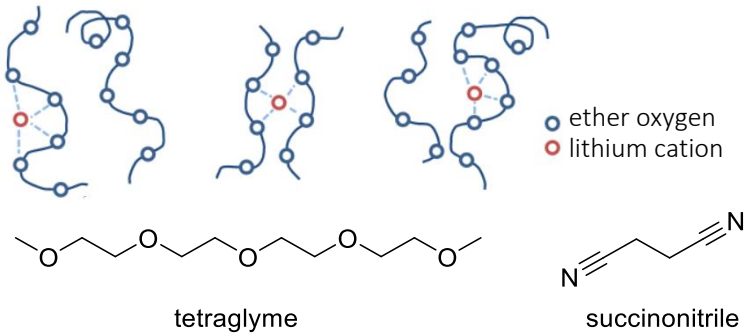

Figure 1.7: Ion transport in PEO+Li salt mixtures; tetraglyme and succinonitrile are used as plasticizers to suppress PEO crystallinity and enhance Li conductivity.

As discussed earlier, ionic conductivity of an electrolyte system is a function of the free-ion concentration and the ionic mobility. Salt dissociation in a host polymer is driven by a decrease in the overall Gibbs free energy, $\Delta G_{mixing} = \Delta H_{mixing} - T\Delta S_{mixing}$. Thus, the most important factors dictating salt dissociation are the lattice energy, ΔH_s, of the salt and the loss in entropy, ΔS, of the polymer chains involved in coordination of the solvated cation. Polymers with low glass transition temperatures such as PEO ($T_g = -70$ °C) possess enough chain flexibility at room temperatures to complex with cations without excessive strain.[41] Evidently, PEO ($\varepsilon \approx 7.5$) + LiTFSI (a low-lattice energy salt) has been the most researched dry polymer electrolyte system.[41]

In a PEO/Li salt mixture, the lowest free-energy configuration for a Li^+ consists of the ion in complexation with six ether oxygen of the PEO polymer chain.[57] The degree of Li salt dissociation has a strong decrease with salt concentration.[58] Ion-dipole complexation between Li^+ and the PEO chains gives rise to pseudo-physical cross-linking that lowers polymer chain flexibility, and is reflected in increase in the glass transition temperature (T_g) of the mixture.[59] The undissociated salt and the neutral ion-aggregates play the role of "filler", impeding the cation transport in the PEO/salt mixtures. As expected, the ionic conductivity (σ) of PEO/Li salt mixtures is a non-monotonic function of the salt concentration, and the maximum in σ is observed for [Li]/[EO] value of 0.085.[60]

As mentioned earlier, Li^+ transport is mediated by segmental motion of the PEO chains surrounding the Li^+, therefore only PEO chains in an amorphous state can participate in ion transport. High molar mass (> 10 kg/mol) PEO exhibits a high degree of crystallinity (≈ 70% w/w) and a melting temperature $T_m \approx 60$ °C.[60] As a result, PEO/Li salt mixtures exhibit appreciable ionic conductivity ($\sigma \approx 10^{-3}$ S/cm at 85 °C) only above the melting point of the mixture.[60] The ionic conductivity for PEO/Li salt mixtures even at 85 °C is a factor of two lower than that of the gel electrolytes at room temperature. For Li-batteries, it is essential that the polymer electrolyte delivers appreciable current at ambient and sub-zero temperatures.[1]

Many strategies have been explored to suppress PEO crystallinity, including incorporation of plasticizers like tetraglyme, low molar mass PEO oligomers, succinonitrile, and ionic liquids (Figure 1.7), and blending with poly(bisphenol A-co-epichlorohydrin) (PBE) or poly(vinyl ethyl ether) (PVEE).[41,61–63] Comb-branched polymers with short PEO side chains that eliminate PEO crystallization, such as poly(oligo(oxyethylene) methacrylate), have been used in lieu of linear PEO polymer to design dry polymer electrolytes.[64,65]

The strong ion-dipole complexation between the cation and PEO polymer chain has an adverse impact on the lithium transference number (LTN).[66–68] Most reports of LTN for Li salts in polymer systems are in the vicinity of 0.2.[11,66,69] Using a polymer electrolyte with low transference number in a Li battery results in lowered energy density and formation of concentration gradients that lead to growth of undesirable Li metal dendrites during the charge-discharge cycles.[70] Strategies to improve the LTN of PEO/Li electrolytes include addition of poly(acrylonitrile) (PAN) and poly(methyl methacrylate) (PMMA) polymers that form ion-dipole complexes with the anion and reduce its mobility.[67] Jo et al. studied nanostructured PEM poly(ethylene oxide-*b*-dithiooxamide) (PEO-*b*-PDTOA)

incorporating Li salts and observed enhanced cation transport and high Li^+ transference number facilitated by anion stabilization, a result of hydrogen bonding interactions between the thioamide moieties and the anions.[71]

Design of a single ion conductor, i.e., immobilization of the anionic moieties can deliver a high LTN (> 0.9).[70,72–74] However, current systems suffer from very poor ionic conductivity and involve complex synthesis, thereby limiting their implementation for a large-scale electrolyte development.[70] Single ion conductors will be discussed in greater detail in the following section.

B. Polymers + ionic liquids

In a previous section, various electrochemical aspects of ILs, their application as solvents and electrolytes were discussed. Design of free-standing membranes incorporating immobilized ILs is crucial for various applications including gas separation membranes, gate dielectrics for organic electronics, and IL-based reference electrodes.[21,25,75,76] This section discusses miscibility of various polymers in common ILs. In particular, systems of polymer + IL with imidazolium cations and TFSI, PF_6^-, and BF_4^- anions (Figure 1.5) are the focus of this sub-section. It has been observed that the Lewis basicity of the IL anion plays an important role in determining solubility of a polymer.[77] Temperature-dependent phase transitions, namely upper critical solution temperature (UCST)[77] and lower critical solution temperature (LCST)[78] phase separation, is observed in certain polymer/IL binary mixtures. LCST phase behavior refers to low-temperature mixing (solubility) and demixing at higher temperatures.

In IL/polymer mixtures, Coulombic interactions as well as other weaker but directional interactions such as hydrogen-bonding, cation-π, π -π, and van der Waals interactions may operate between the ions as well as between the ions and polymer moieties.[77,79] Rogers and co-workers in 2002 first demonstrated dissolution of cellulose (Figure 1.8.1) in ILs with

strong hydrogen-bond accepting anions such as chloride and acetate that can solvate the cellulose hydroxy groups.[80] Mixtures of another commercially significant random copolymer of vinylidene fluoride and hexafluoropropylene, P(VdF-*r*-HFP) (Figure 1.8.2) and ILs undergo sol-gel transition with decreasing temperature. The sol-gel transition holds huge potential in design of processable ion gels for use in electrochemical devices, e.g., "cut and stick" rubbery ion gels as high capacitance gate dielectrics.[75] Kakiuchi and co-workers[81] designed IL-based reference electrodes by preparing free-standing monoliths of P(VdF-*r*-HFP) and a hydrophobic IL. This system is discussed in Chapter 4.

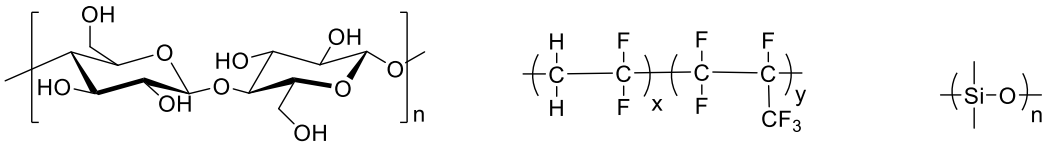

1. cellulose 2. poly(vinyl fluoride-*r*-hexafluoropropylene) 3. poly(dimethyl siloxane)

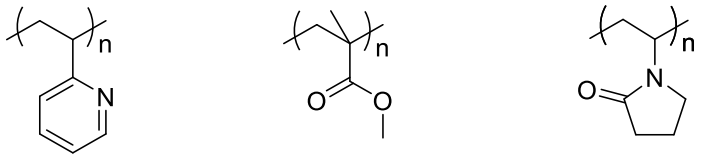

4. poly(2-vinylpyridine) 5. poly(methyl methacrylate) 6. poly(vinyl pyrrolidone)

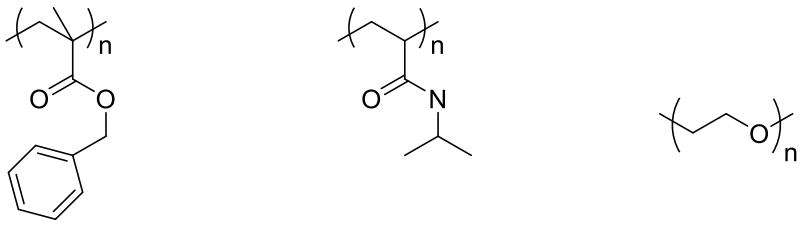

7. poly(benzyl methacrylate) 8. poly(*N*-isopropyl acrylamide) 9. poly(ethylene oxide)

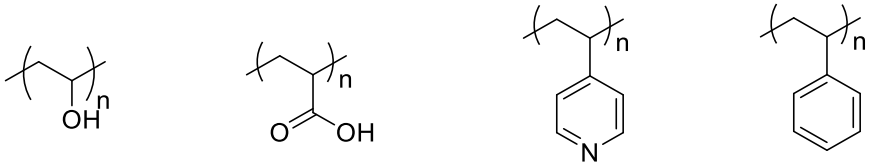

10. poly(vinyl alcohol) 11. poly(acrylic acid) 12. poly(4-vinylpyridine) 13. polystyrene

Figure 1.8: Combinations of polymer and ILs exhibit exciting behavior that can be tuned

for desired applications. Mixtures of PNIPAm and ILs exhibit UCST behavior, whereas PBnMA + ILs undergo LCST phase separation. Polymers like PS and P4VP (above certain molar masses) are immiscible in most ILs and thus are ideal candidates for the rigid, non-plasticized mechanical phase in developing nanostructured polymer electrolytes.

As shown in Figure 1.8, poly(dimethyl siloxane), PDMS, poly(2-vinylpyridine), P2VP, and poly(methyl methacrylate) are soluble in ILs with hydrophobic anions such as TFSI, TfO, and PF_6^-, but are insoluble in ILs with hydrophilic anions e.g. BF_4^-.[77] Poly(vinyl pyrrolidone), PVP on the other hand, is soluble in most of the ILs. A major distinction between PEO/Li salts and miscible-polymer/IL mixtures is that ILs self-dissociate and thus do not need strong coordination with the polar moieties of the polymer chains.[82] As a result ion transport in polymer/IL mixtures is much less coupled to the segmental dynamics of the polymer chains, compared to PEO/Li salt systems. Flexibility of the host polymer still has a huge impact on the conductivity of polymer/IL mixtures, e.g. [EMI][TFSI] mixtures (IL content 50% w/w) with poly(ethyl acrylate) ($T_g \approx -24$ °C) exhibit about five times higher conductivity than PMMA ($T_g \approx 105$ °C)/IL mixtures.[83]

Polymers such as poly(vinyl alcohol) and poly(acrylic acid) that exhibit strong intra- and inter-molecular hydrogen-bonding are insoluble in most ILs.[77] It should be noted that polymer solubility in IL is dependent not only on the nature of the polymer but also the molecular weight, molecular weight distribution, and the concentration of the polymer. For example, polystyrene, PS (Figure 1.8.13) of molar mass > 2 kg/mol is insoluble in almost every IL, whereas styrene monomer and even small PS oligomers are soluble in certain hydrophobic ILs. This molecular weight solubility dependence is exploited in developing PEMs via polymerization-induced microphase separation, as discussed further in Section 1.4.

The LCST behavior of PNIPAm in aqueous media has been used to develop thermo-responsive hydrogels with applicability in drug-delivery, actuators, and sensing devices.[84] Interestingly, PNIPAm/IL mixtures with TFSI anions exhibit UCST behavior.[77] As

discussed earlier, the Gibbs free energy of mixing (ΔG_{mix}) for the polymer and solvent determines the compatibility of the mixture, where $\Delta G_{mix} = \Delta H_{mix} - T\Delta S_{mix}$. For a LCST phase transition, essential requirements are a negative ΔS_{mix} in addition to a negative ΔH_{mix}, i.e. an exothermic solvation process should exist. With increasing temperature, the entropic term ($-T\Delta S_{mix}$) overwhelms the enthalpic term (ΔH_{mix}), and the mixture undergoes phase separation.

PEO/IL mixtures with BF_4^- anions exhibit observable LCST behavior.[78] Hydrogen-bonding interactions between the acidic protons of the cation (IL) and the ether oxygen appears to be responsible for the negative ΔH_{mix} and negative ΔS_{mix}.[78] Poly(benzyl methacrylate), PBnMA (Figure 1.8.7) is another polymer that exhibits LCST behavior when mixed with TFSI and PF_6^- ILs. A solvation shell formed by the IL around the aromatic side chain of the PBnMA is postulated as the reason for the negative ΔS_{mix}.[85] Watanabe and co-workers showed that stimuli-responsive materials with controlled LCST temperatures can be designed using an azobenzene-containing PBnMA copolymer (P(AzoMA-*r*-BnMA) and tuning the photoisomerization state of the azobenzene.[86]

C. Single-ion conductors

In conventional dual-ion conducting PEMs prepared by incorporating lithium salts into a PEO matrix, the Li^+ cations are less mobile than their anionic counterparts.[87] In LIBs employing these PEMs, the anions tend to accumulate at the anode, causing a concentration gradient that leads to cell polarization, and therefore poor cell performance, voltage losses, undesirable reactions, and ultimately cell failure.[88] On the other hand, it has been demonstrated that PEMs with lithium transference number (LTN) approaching unity with no concentration gradient successfully avoid Li dendrite growth.[89] One strategy to achieve a single-ion conductor is chemically tethering the anion to the polymer backbone. Feng et al. studied copolymers of lithium (4-styrenesulfonyl)(trifluoromethanesulfonyl)imide

(LiSTFSI) (Figure 1.9a) and methoxy-polyethylene glycol acrylate.[72] The highest ionic conductivity exhibited by the copolymer electrolyte reached 10^{-4} S/cm at 60 °C and LTN > 0.9, obtained at an ethylene oxide (EO):Li^+ ratio of 20.5.[72] In comparison, PEO/Li salt electrolytes reach $\sigma \approx 10^{-3}$ S/cm at 85 °C, however LTN ≈ 0.2.

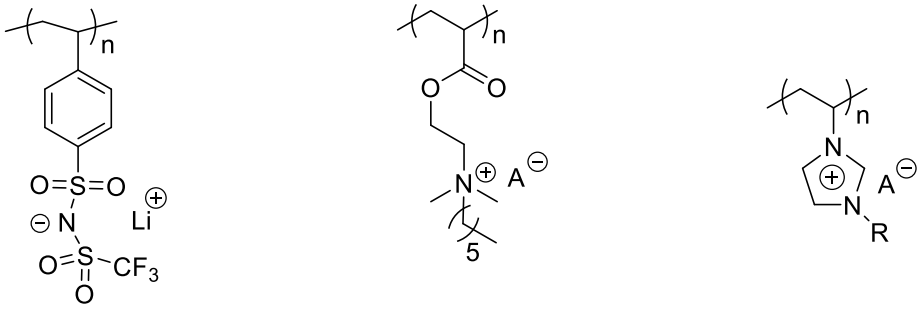

poly(4-styrenesulfonyl-(trifluoromethylsulfonyl)imide) poly(quaternary ammonium acrylate) poly(1-vinylimidazolium)

Figure 1.9: Polymerized single-ion conductors mitigate undesired cell polarization caused by the bulk movement of the counter-ions.

Another approach is to build single-ion polymer-grafted nanoparticles (NPs) or "salty" NPs. Villaluenga et al. built NPs composed of silsesquioxane cores with covalently bound polystyrenesulfonyllithium (trifluoromethylsulfonyl)imide (PSLiTFSI) chains (Figure 1.10) synthesized by nitroxide-mediated polymerization.[90] Similar to PEO/LiTFSI systems, the ionic conductivity of PEO doped with salty NPs optimized at an intermediate concentration at 1.1×10^{-5} S/cm at 90 °C and LTN ≈ 0.98, obtained at an ethylene oxide (EO):Li^+ ratio of 12.[90]

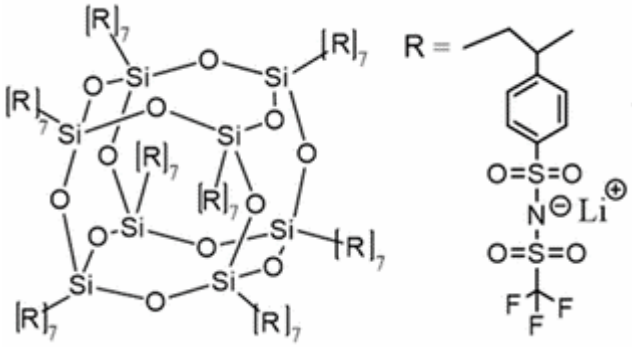

Figure 1.10: Chemical structure of the salty nanoparticles (POSS-PSLiTFSI). Reproduced

with permission from Ref. 90. Copyright 2017 American Chemical Society.

1.3 Nanostructured Polymer Electrolytes

Nanostructured polymeric materials including block polymers (BPs), cross-linked networks, and BP/nanoparticle hybrids permit design of microphase-separated soft materials satisfying competing constraints such as high conductivity and mechanical or thermal robustness. For instance, Nafion's (Table 1.1a) exceptional conductivity and mechanical properties have been attributed to its nanoscale morphology that consists of conducting, water-filled hydrophilic domains (terminal sulfonic acid groups) and structural, hydrophobic domains (perfluorinated polymer backbones).[91]

Table 1.1: Examples of nanostructed PEMs and their morphologies.

	Nanostructured PEMs	Morphology
a.	Hydrated Nafion 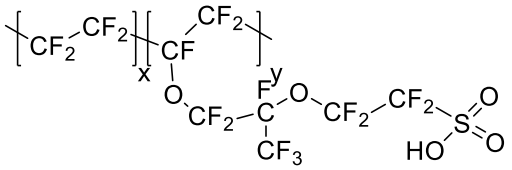 $\sigma \approx 0.1$ S/cm at 30 °C[13] (water content: 60% v/v) $G' \approx 0.12$ GPa	interconnected network morphology
b.	PS-*b*-PEO + LiTFSI 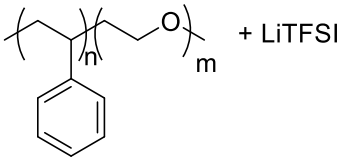 $\sigma \approx 0.1$ mS/cm at 90 °C (r = 0.085) $G' \approx 0.1$ GPa at 90 °C (r = 0.085)[92]	LAM

c.	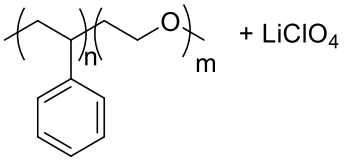	
	$\sigma \approx 3.5\times10^{-4}$ S/cm at 100 °C (r = 0.04)[93]	hexagonally perforated lamellae
	$\sigma \approx 4.5\times10^{-4}$ S/cm at 100 °C (r = 0.04)	HEX (conducting matrix)
	$\sigma \approx 8.8\times10^{-5}$ S/cm at 100 °C (r = 0.04)	LAM
d.	hydrated poly(styrenesulfonate-*b*-methylbutylene)	
	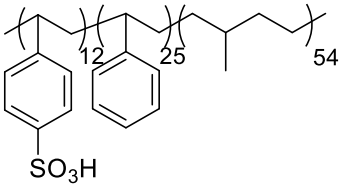	
	$\sigma \approx 0.045$ S/cm at 25 °C	LAM
	$\sigma \approx 0.06$ S/cm at 25 °C (in the direction of the aligned grains)[94]	LAM (grain alignment)
e.	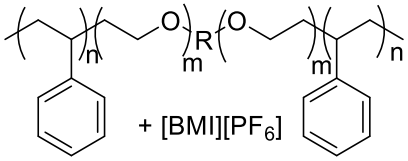	glassy PS micellar PS cores bridged with IL-swollen PEO midblock
	$\sigma \approx 1.1$ mS/cm at 25 °C[95] $G' \approx 1$ kPa at 25 °C.	

One of the most researched routes to nanostructured composite materials is through the use of block polymers. Block polymers, which are composed of two or more covalently connected homopolymers, exhibit microphase-separated ordered structures above a certain segregation strength (χN) (*e.g.* $\chi N \geq 10.5$ for a symmetric diblock copolymer within mean-field theory Figure 1.11), where χ is the Flory-Huggins interaction parameter between the copolymer blocks and N is the volumetric degree of polymerization of the block polymer.[96] A plethora of block polymer nanoscale morphologies (≈ 5 to 50 nm lengthscale) can be accessed by tailoring the chemistry, identity, and ratio of the constituent components. Commonly obtained morphologies for an A-B diblock copolymer system include alternating lamellae (LAM), gyroid networks (GYR), cylinders arranged on a hexagonal

lattice (HEX), and spheres arranged on a body-centered-cubic lattice (BCC) (Figure 1.11).[97] Recent work has found that some block polymers can form complex sphere phases such as a dodecagonal quasicrystal (DQC) or the Frank-Kasper σ phase.[98]

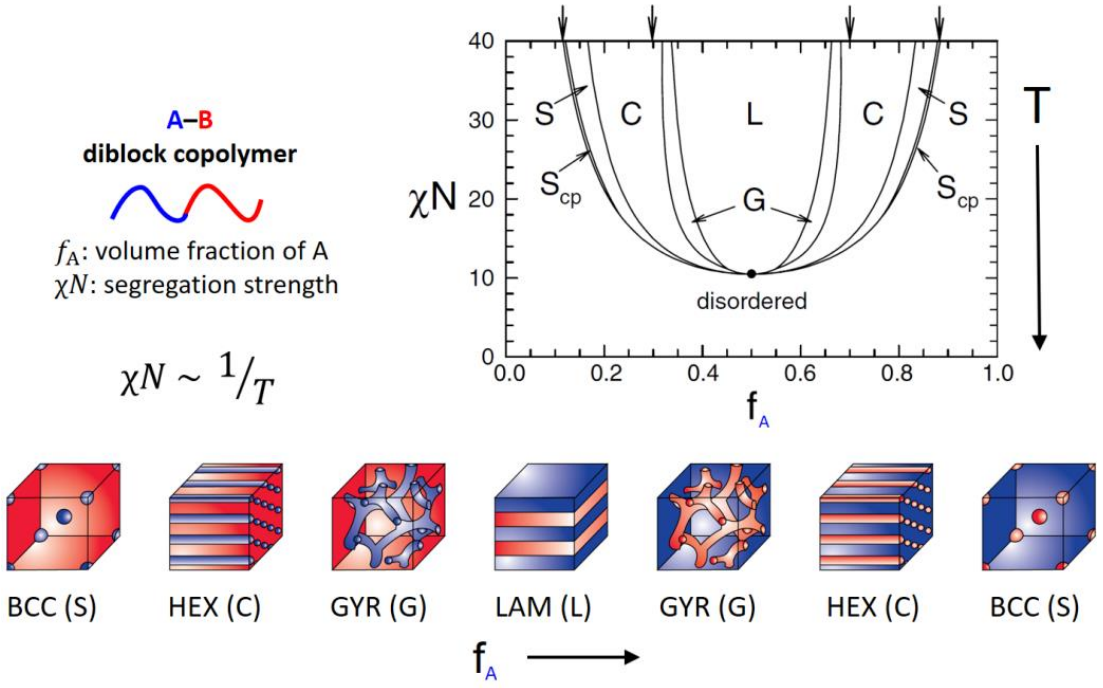

Figure 1.11: Mean-field theory phase portrait for an AB diblock copolymer. f_A is the volume fraction of block A. S_{cp} refers to close-packed spheres. The vertical lines above the phase portrait indicate phase-boundaries predicted by the strong-segregation theory. Phase portrait adapted from Ref. 97. Reproduced with permission. Copyright 2001 IOP Publishing.

Block Polymer Electrolytes

Over the last decade, block polymer systems wherein one of the microphases is selectively doped with ionic liquid or lithium salt have been extensively studied.[3–12] For the LIBs, the model block polymer electrolyte systems involve glassy polystyrene or poly(styrene-*co*-divinylbenzene) as the mechanically robust domain, and a polyether such as PEO or poly(oligo(oxyethylene)methacrylate) that is doped with low-lattice energy salt like LiTFSI.[12,99–104] Singh et al. demonstrated that lamellae–forming PS-*b*-PEO diblock polymers incorporating LiTFSI (Table 1.1b) exhibited reasonable mechanical rigidity (G'

≈ 0.1 GPa) below the T_g of PS.[92] However, due to the semi-crystallinity of the PEO/Li domain, the PEMs exhibited high conductivity (> 0.1 mS/cm) only above 90 °C.[92] Also, the observed ionic conductivity was lower than the anticipated, even after accounting for the tortuosity of lamellae, indicating the presence of dead-ends and network-defects in the conducting nanochannels.

Ionic conductivity of a nanostructured PEM is governed by the effective concentration of the free ions, the mobility of the ions that is strongly dependent on temperature and flexibility of the polymer, and the tortuosity and connectivity of the conducting pathways.[10,11,105,106] In the case of block polymer electrolytes with polyether/Li salt as the conducting phase, several studies have found that LiTFSI selectively partitions to the polyether microphase and that the segregation strength (χN) between the two microphases increases with salt content, thereby increasing the order-disorder temperature of the system.[57,58,103,107] In particular, the ionic conductivity, σ, for a PS-*b*-PEO/LiTFSI is observed to increase with molecular weight.[60] Gomez et al. demonstrated that the Li^+ are localized in the middle of the PEO domains.[107] The authors observed increased ion dissociation in PEO/LiTFSI microphases with larger domain sizes, elucidating the increase in σ with molecular weight.

Dimensionality and Continuity of the Micro-domains

A block polymer forms several grains within a typical thickness of a PEM (10-100 μm).[108] Therefore, the ion-transport can be divided in two categories, (i) inter-grain transport that depends on the connectivity of the conducting nanochannels across the grain boundaries, and (ii) intra-grain transport that depends on the dimensionality of the conducting pathways. For example, a lamellar morphology provides two dimensional (2D) conducting pathways and on average only 2/3 of the domains contribute to ion transport (Figure 1.12).[109] On the other hand, continuity of the matrix for HEX morphology (non-

conducting or mechanical phase cylinders) is not (or less) affected by grain orientation angle.[9,93,105]

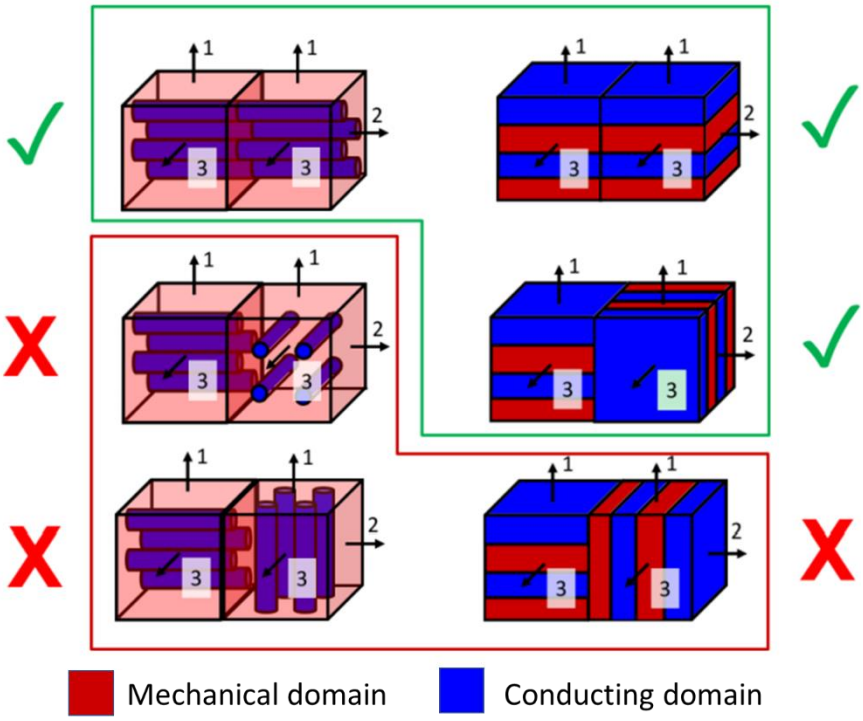

Figure 1.12: Dimensionality of conductivity pathways in HEX and LAM. The green check marks indicate grain orientation that facilitate continuous conducting channels. In HEX, on average, only one out of three grain orientation is effective in ion-transport compared to two/third for LAM. Reproduced with permission from Ref. 109. Copyright 2016 American Chemical Society.

Young and Epps studied PS-*b*-PEO doped with $LiClO_4$ (Table 1.1c) and observed that samples with 3D conducting pathways such as hexagonally perforated lamellae and HEX (PEO matrix) exhibited higher σ than samples with lamellar (2D pathways), even after correcting for domain orientation.[93] Simone and Lodge made similar observation in PS-*b*-PEO doped with IL [EMI][TFSI].[93] In another study, Park and Balsara observed that grain alignment in hydrated poly(styrenesulfonate-*b*-methylbutylene) (Table 1.1d) lamellar copolymer films induced by shearing[94] or magnetic or electric fields[94] provided highly

anisotropic proton conductivity; a 30% increase in σ in the direction of the grain alignment relative to the as-cast samples.

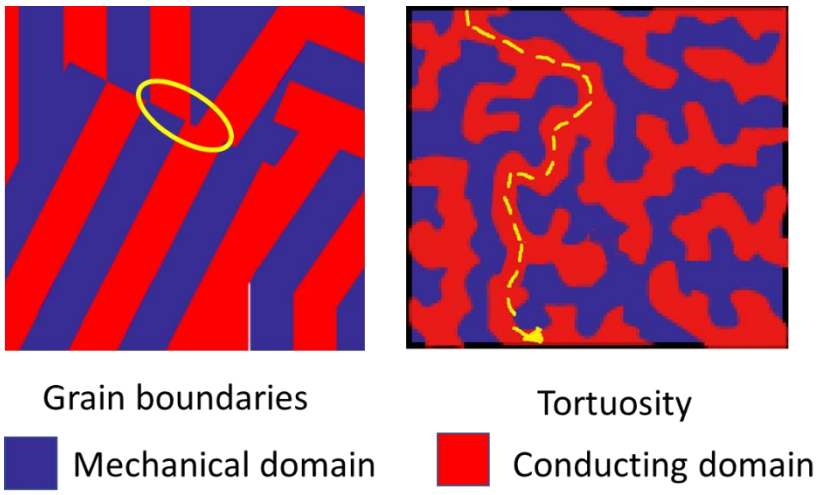

Figure 1.13: Morphological factors affecting ionic conductivity of nanostructured PEM. (a) Grain boundaries in "ordered" morphology (LAM, HEX) give rise to dead-ends in the conducting domains. (b) Tortuosity: increased path length ion must travel relative to a straight path.

For inter-grain transport, the bends and tortuosity of the conducting channels lower the ionic conductivity. Isotropic, bicontinuous morphologies (e.g., gyroid) featuring three dimensional ion transport pathways do not require domain alignment. However, the tortuosity of the transport pathways in such a bicontinuous morphology lowers the overall conductivity, in comparison to the straight conducting routes present in a well-aligned cylindrical morphology (Figure 1.13b).[102,110]

Similar to ionic conductivity, the mechanical properties are dictated by the dimensionality and continuity of the mechanical microphase. Several studies report that nanostructured materials with network morphologies such as the gyroid that have continuous supporting domains boast superior mechanical response relative to their 1D (non-conducting cylinders) or 2D (LAM) counterparts.[111,112]

"Ion gels" designed with ABA copolymers swollen with high IL contents exhibit excellent ionic conductivity.[113,114] He et al. first studied ion gels with poly(styrene-*b*-ethylene oxide-*b*-styrene) swollen with ionic liquid [BMI][PF_6] (Table 1.1e).[95] The incompatibility between the PS endblocks and the IL, drives the block polymer to self-assemble into discrete glassy cores of PS bridged with IL-swollen PEO midblock. Lack of long-range continuity in the mechanical phase restricts these ion-gels to moduli below 1 MPa.

In summary, long range connectivity in both the mechanical and conducting phases is critical in designing high-performance nanostructured PEMs. A block copolymer/IL system with the gyroid morphology might at first seem ideal for ion transport, as it offers two percolating domains; however, the gyroid phase occurs over a relatively narrow range of block volume fractions (Figure 1.11).[115] In the next section, various strategies that allow design of nanostructured materials with bicontinuous morphology are discussed.

1.4 Nanostructured Materials with Bicontinuous Morphology

Nanostructured polymeric materials with well-defined and three-dimensional percolating network-morphologies that exhibit high surface to volume ratios are crucial for developing ultrafiltration membranes,[116] heterogeneous catalysts,[117] and PEMs. In PEMs, a bicontinuous morphology ensures that the conducting pathways are uninterrupted in all directions. Synthetic strategies to access bicontinuous morphologies can broadly be categorized as follows: (i) equilibrium self-assembly, and (ii) kinetically trapping non-equilibrium, bicontinuous morphologies.

In the case of self-assembled block polymers, bicontinuous morphologies such as the gyroid phase occupies a small compositional window on the phase map (Figure 1.11), limiting the combinations of the polymer chemistry, molecular weights and temperatures.[115] Interestingly, Mahanthappa and co-workers observed that in ABA triblock

copolymers with a disperse midblock, the compositional dispersity and ABA triblock chain topology frustrate long-range ordering, facilitating expanded composition windows of disordered bicontinuous morphologies (Figure 1.14).[118,119] However, even in these systems, the LAM morphology still occupies a much larger range on the compositional spectrum.

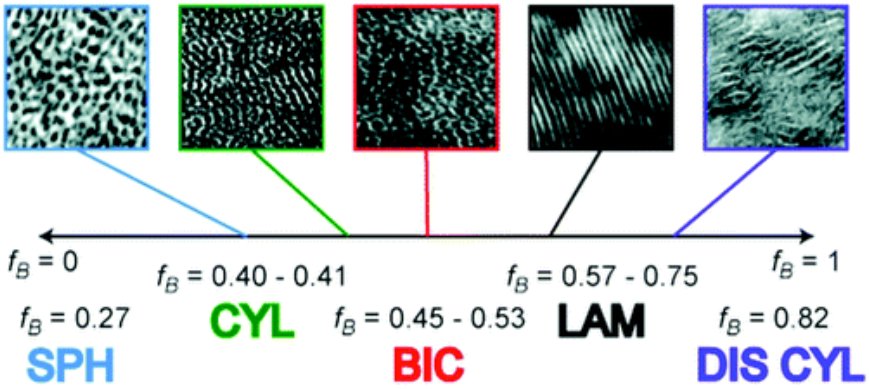

Figure 1.14: Self-assembly morphologies observed in SBS triblock copolymers (S = poly(styrene) and B = poly(1,4-butadiene)) composed of a broad polydisperse B block ($Đ$ = 1.73–2.00) flanked by relatively narrow dispersity S blocks ($Đ$ = 1.09–1.36). Composition window for the disordered bicontinuous morphology spans the range f_B = 0.45–0.53. Reproduced with permission from Ref. 118. Copyright 2012 American Chemical Society.

Ternary polymer blend systems consisting of a volumetrically symmetric A–B diblock copolymer and corresponding immiscible A and B homopolymers (typically 1/5 the molecular weight of the diblock) exhibit a variety of microstructured morphologies, such as lamellae, a hexagonal phase, and a bicontinuous microemulsion.[120] The homopolymers selectively swell the lamellar domains increasing the characteristic length scale. At homopolymer loadings near "Lifshitz composition", the bending energy of the interface becomes comparable to the energy of thermal fluctuations in the system, and the system transitions into a bicontinuous microemulsion (BμE) morphology, consisting of globally disordered co-continuous domains.[120]

Zhou et al. demonstrated a facile method for preparing nanoporous materials with isotropic, three-dimensionally continuous pore structures from polymeric bicontinuous microemulsion precursors.[121] The BμE precursor was prepared from ternary blends of polyisoprene (PI), polystyrene (PS), and a PI−PS diblock copolymer. Nanoporous materials were obtained by selective cross-linking of PI domain with the subsequent removal of the PS domain by solvent dissolution. Jones and Lodge followed a similar route to develop polymeric bicontinuous microemulsion templates that were used to prepare nanoporous ceramic materials.[122] In both these materials, pore structure is disordered and 3-D continuous.

Recently, Irwin et al. studied a pseudoternary polymer blend system containing PEO and PS homopolymers, a PS-*b*-PEO block copolymer, and LiTFSI and observed a bicontinuous microemulsion (BμE) in addition to other typical morphologies (Figure 1.15).[109] However, as seen in the figure, the bicontinuous morphology is apparently accessible only for a small compositional range.

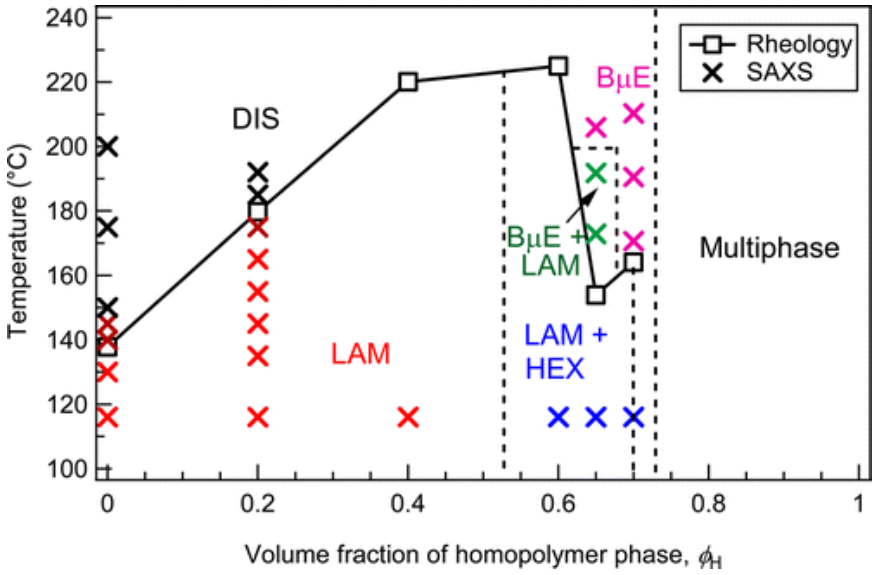

Figure 1.15: Phase diagram for a pseudoternary polymer blend system containing PEO and PS homopolymers, a PS-*b*-PEO block copolymer, and LiTFSI. Open squares represent order–disorder transition temperatures. The solid lines connecting data points are drawn to guide the eye, while the dashed vertical lines indicate approximate phase boundaries.

Reproduced with permission from Ref. 109. Copyright 2016 American Chemical Society.

Another strategy employed in preparation of samples with co-continuous nanodomains is building randomly end-linked copolymer networks (RECNs). The presence of random cross-links frustrates the formation of highly ordered phases, facilitating disordered bicontinuous structures under appropriate conditions.[123] Walker et al. employed high yield thiol–ene chemistry and norbornene end-functionalized PEO and PS polymer chains (in the presence of Li salt) to develop PEMs with microphase-separated co-networks (Figure 1.16).[124] Using ionic conductivity and mechanical properties as probe to determine connectivity of each microphase, the authors reported existence of a bicontinuous morphology over a wide range of compositions, spanning PEO volume fractions from ~ 0.3–0.65. Further, the variation of the precursor polymer molecular weight allowed control over the length-scale of the co-continuous structure and thus optimization of the conductivity and mechanical properties. As evident from the reaction scheme (Figure 1.16), building specialized polymers with end-functionalization (here thiol–ene chemistry) that can partake in chemical cross-linking are crucial for RECNs.

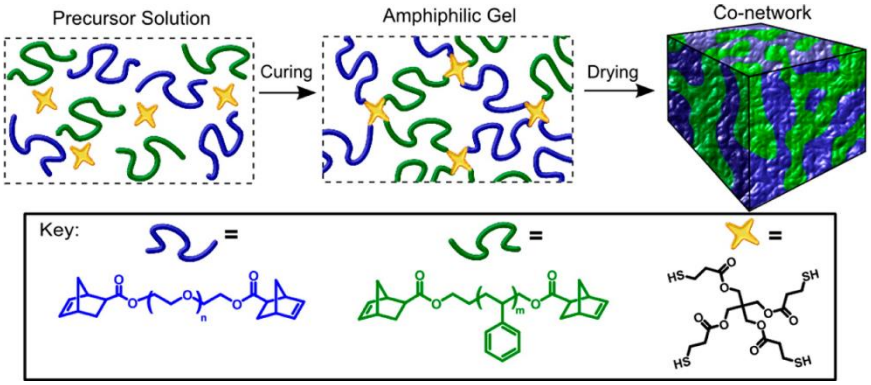

Figure 1.16: Reaction scheme for obtaining salt-loaded co-network samples from norbornene end-functionalized precursor polymers via RECNs strategy. Reproduced with permission from Ref. 124. Copyright 2014 American Chemical Society.

In block polymers, the approach of the order-disorder transition (ODT) from the disorderd state by lowering the temperature is characterized by composition fluctuation-

induced co-continuous morphology that is locally correlated despite the absence of global long-range order (Figure 1.17b).[125,126] Teran et al. studied a lamellar PS-*b*-PEO doped with LiTFSI in the vicinity of T_{ODT} (temperature for the ODT).[127] The authors observed that, at temperatures slightly above T_{ODT}, the change in the nano-scale morphology (studied by X-ray scattering) and the interconnectivity of conductive domains induced by composition fluctuations resulted in a sudden increase in the ionic conductivity.

A nanostructured polymeric material with continuous three-dimensional network morphology, therefore, can be achieved by kinetically trapping the block polymer morphology associated with the fluctuating disordered state. Following this approach, Vidil et al. studied a reactive diblock containing polylactide (PLA) and a cross-linkable block consisting of a statistical copolymer of styrene (S) and glycidyl methacrylate (GMA) [PLA-*b*-P(S-*s*-GMA)] (Figure 1.17) in the presence of a thermally latent initiator that can trigger cross-linking temperatures in the reactive polymer at curing temperatures $T_{curing} \sim T_{ODT}$.[128] As the diblock was heated above the T_{ODT}, the chemical cross-linking kinetically trapped the disorderd state. Subsequently, removing the chemically etchable (PLA) block delivered nanoporous materials exhibiting narrow pore-size distribution, high surface to volume ratio and is bicontinuous over a large sample area.

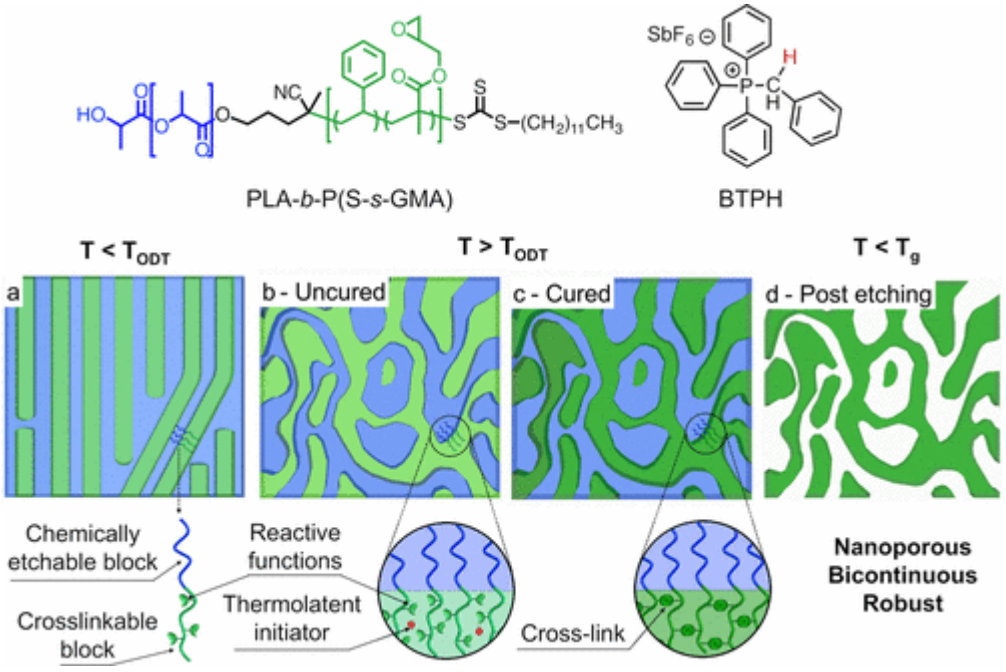

Figure 1.17: Chemical cross-linking of diblock polymer in the disordered state. (a) Lamellar diblock copolymer; blue: etchable block and green : a cross-linkable block containing a thermally latent cross-linking initiator. (b) Disordered bicontinuous morphology adopted by the diblock above T_{ODT}. (c) The thermolatent initiator triggers cross-linking reaction above the T_{ODT}. (d) After the cross-linkable phase is cured, the etchable block is removed to obtain well-defined percolating nanopores. Reproduced with permission from Ref. 128. Copyright 2017 American Chemical Society.

A salt/IL doped PEM with bicontinuous morphology can be developed following the approach developed by Vidil et al.[128] One could envision using [PEO-*b*-P(S-*s*-GMA)] polymer doped with Li salt, heating the system above the T_{ODT}, and quenching the disordered morphology. However, the incorporation of Li salt significantly increases the segregation strength between the PS and the conducting phase, raising the T_{ODT}, possibly beyond the thermal stability of the polymer itself. For example, a PS-*b*-PEO (PS: 6.4 kg/mol, PEO: 7.2 kg/mol) with modest mechanical properties and r =0.05 has $T_{ODT} \approx$ 180 °C.[129] A possible solution would be a two-step process: building a PS-PEO cross-linked membrane with bicontinuous morphology and then incorporating LiTFSI by soaking the cross-linked membrane in a salt/solvent bath. In this process, there is a poor

control over the amount of incorporated salt, which is crucial in optimizing conductivity. Also, the excessive swelling can strain the densely cross-linked framework and disintegrate the PEM.

As discussed earlier, the segregation strength (χN) of a block polymer can be tuned by controlling the system temperature (T) as $\chi \sim 1/T$ and by controlling the molecular weight of the polymer (i.e. N). Vidil et al.[128] utilized system temperature to control the morphology of the system; LAM below the T_{ODT} and a bicontinuous morphology above the T_{ODT}. Similarly, at a given reaction temperature, a diblock with a certain degree of polymerization such that χN is slightly less than the ODT segregation strength requirement would adopt a fluctuation-induced bicontinuous morphology, whereas higher molar mass polymers (higher N) would self-assemble into ordered morphologies.

Recently, Seo and Hillmyer[130] reported a facile, one-pot synthetic scheme to prepare cross-linked block polymer membranes exhibiting bicontinuous morphologies. Reversible addition-fragmentation chain-transfer (RAFT) polymerization was implemented for a controlled growth of styrene (S) and divinylbenzene (DVB) from a polylactide macro-chain transfer agent (PLA-CTA) (Figure 1.18). As polymerization proceeds, the molar mass and volume fraction of P(S-*co*-DVB) in the emerging PLA-*b*-P(S-*co*-DVB) block polymer increase, driving the system toward microphase separation. Simultaneous growth and *in situ* crosslinking of the polystyrene (PS) block due to the incorporation of DVB kinetically arrested the system in a co-continuous morphology that is locally correlated but does not exhibit long-range order, reminiscent of the fluctuation-induced structure observed just above the order-disorder temperature in lamellar-forming block copolymer melt.[131]

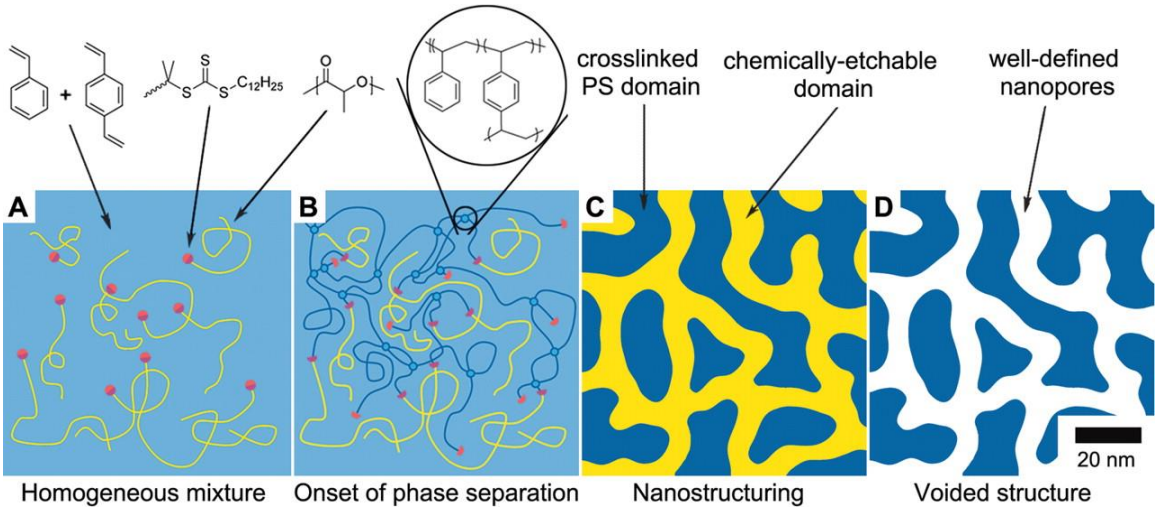

Figure 1.18: Nanoporous monolith generation by a controlled polymerization-induced microphase separation process. (A) A macro-CTA containing the etchable polymer (yellow) is dissolved in the mixture (light blue) of a monomer and a cross-linker. RAFT copolymerization allows controlled growth of chains (dark blue) generating a block polymer structure; the growing chains are also being cross-linked in situ (B). At a critical conversion, microphase separation occurs over a small time interval, and cross-linking arrests the emergent to generate and arrest a bicontinuous structure with a nanoscopic length scale (C). Subsequent removal of the etchable polymer produces percolating nanopores in a cross-linked and mechanically robust matrix (D). Reproduced with permission from Ref. 130. Copyright 2012 American Association for the Advancement of Science.

Schulze, et al.[12] extended the polymerization-induced microphase separation (PIMS) strategy to design PEMs by replacing the PLA-CTA with a PEO-CTA and adding IL to the reaction mixture. The key to the PIMS approach is ensuring that the matrix monomer (i.e., styrene and DVB) is compatible with the conducting block and the electrolyte (here PEO +IL) in order to produce a homogeneous reaction mixture, but also ensuring that the emerging matrix polymer (i.e., P(S-co-DVB)) is not, so that microphase separation can be induced during polymerization. The authors reacted the homogeneous liquid precursor of S/DVB monomers, IL, and PEO-CTA at 120 °C. During the reaction, IL becomes immiscible with the PS phase and partitions to the PEO-rich phase to form a conducting domain. The resultant PEM exhibited an exceptional combination of both high ionic

conductivity (in excess of 1 mS/cm) and high modulus (elastic modulus ≈ 10^7 Pa at 200 °C). The bicontinuous morphology yielded isotropic, continuous conducting pathways of PEO and IL, along with a cross-linked PS network that imparted mechanical integrity and thermal stability to the system well above the glass transition temperature of linear PS ($T_g \approx 100$ °C).

1.5 Thesis Outline

The goal of this thesis is to develop a framework for building robust, high-performing PEMs by decoupling the mechanical properties and ion transport. Motivated by the promise of PIMS PEMs exhibiting co-continuous network morphologies, in this thesis, we adapted the synthetic route developed by Schulze, et al.[12] to develop nanostructured PEMs targeted for various electrochemical applications. Chapter 2 presents preparation of nanostructured PEMs incorporating a protic ionic liquid (IL) into one of the domains of a microphase-separated block copolymer. The resulting PEMs exhibit high proton conductivity and thermal stability at elevated temperatures, desirable for high-temperature, anhydrous fuel cells. Chapter 3 details development of robust PS-*b*-PEO PEMs based on the PIMS platform, incorporating Li salt and succinonitrile plasticizer in the PEO domains. Chapter 4 focuses on design of ready-to-use IL-based reference electrodes. In particular, PIMS strategy allowed solvent-free, single-step fabrication of mechanically robust reference electrodes with controlled shape and size. Chapter 5 provides a brief summary of the research, and discusses proposed future directions. The Appendix details preparation and preliminary results of PIMS PEMs incorporating phosphoric acid.

Chapter 2 – Anhydrous Proton Conducting Polymer Electrolyte Membranes*

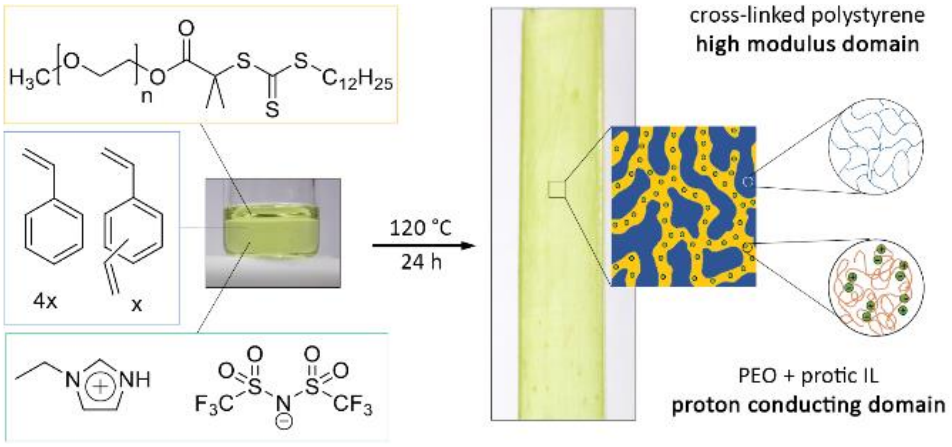

One-pot synthetic strategy transforms a homogeneous liquid precursor into robust and transparent monoliths.

This chapter presents in-situ preparation of nanostructured PEMs incorporating a protic ionic liquid (IL) into one of the domains of a microphase-separated block copolymer created via polymerization-induced microphase separation (PIMS). This facile, one-pot synthetic strategy transforms a homogeneous liquid precursor consisting of a poly(ethylene oxide) macro-chain transfer agent (PEO-CTA), styrene and divinylbenzene monomers, and protic IL into robust and transparent monoliths. The resulting PEMs exhibit a bicontinuous morphology comprising PEO/protic IL conducting pathways and highly cross-linked polystyrene (PS) domains. This approach is very promising for development of high-temperature, robust PEMs with excellent proton conductivities.

*Reproduced with permission from Chopade, S. A.; So, S.; Hillmyer, M. A.; Lodge, T. P. *ACS Appl. Mater. Interfaces* **2016**, *8*, 6200–6210.

2.1 Introduction

Polymer electrolyte membranes (PEMs) that facilitate efficient transport of charged species are critical components of various electrochemical devices.[23,25,48,132–138] Nanostructured PEMs exhibiting distinct structural and ion-conducting phases can offer high ionic conductivity, while simultaneously satisfying orthogonal mechanical and/or thermal property requirements (*e.g.*, mechanical robustness, long term creep resistance, or high-temperature stability).[3,139] One attractive route to such hybrid materials with optimized orthogonal properties involves self-assembled block polymer/ionic liquid mixtures.[5,10,52,93,105,140–144] In such systems, one of the domains selectively incorporates ionic liquid and facilitates ion-conducting pathways, while the other domain, typically glassy and insulating, serves as a mechanical framework providing strength and durability.

Ionic liquids (ILs) are molten salts with low melting temperatures (below 100 °C)[145] and have received significant attention owing to their unique combination of high ionic conductivity, excellent chemical and thermal stability, negligible vapor pressure, and wide electrochemical windows.[24,46,47] Proton conducting or protic ILs synthesized using Brönsted acid–base pairs exhibit excellent proton conductivity (≈ 25 mS/cm at 120 °C) under dehumidified conditions, and can be thermally stable even at temperatures in excess of 300 °C.[22,26,136,146] Accordingly, PEMs incorporating protic ILs are interesting candidates for fuel cells operating at elevated temperatures (100–200 °C) and low humidity. These conditions favor enhanced electrode reaction kinetics and higher tolerance of typical catalysts to carbon monoxide impurities in the hydrogen fuel.[15,23,25,147–150]

Extensive studies on protic ILs and ionic melts consisting of imidazole (Im) and bis(trifluoromethanesulfonyl)imide (HTFSI) demonstrated that the base-rich IL conducts protons via two mechanisms: vehicular transport of the protonated imidazolium cation and the faster proton-hopping or Grotthuss-type mechanism, involving proton shuttling

between protonated imidazolium cations (HIm^+) and neutral imidazole (Im) molecules.[22,52,146] However, the presence of the volatile, neutral Im (boiling point ≈ 256 °C) limits the thermal stability of this system.[15,22]

Ionic conductivity of a PEM incorporating an ionic liquid is governed by the effective concentration of free ions, the mobility of the ions (strongly dependent on temperature and flexibility of the polymer), and the connectivity of the conducting pathways.[10,11,105,106] As observed in conventional humidified Nafion membranes, strong segregation between the structural and conducting domains enhances PEM conductivity.[91] Likewise, in the case of block polymer/IL systems, IL selectivity for one of the domains could effectively enhance the conductivity.[10,151] Another structural factor imperative for high conductivity is the presence of well-connected conducting channels spanning the membrane. In a recent study, long-range proton conducting pathways in sulfonated poly(ether ether ketone) (SPEEK) membranes enriched with IL using functionalized graphene oxides significantly enhanced the membrane conductivity in comparison to a SPEEK control.[152]

In contrast, block polymer/IL membranes designed by solvent casting a mixture of polymer and IL frequently develop network defects such as grain boundaries, dead ends and isolated domains that disrupt the continuity of the conducting channels.[93,153] For example, block polymer PEMs with lamellar or conducting cylindrical domains essentially require the conducting pathways to be perpendicularly oriented to the electrode surface for optimal performance.[106] Grain alignment induced by shearing[94] or magnetic or electric fields[94] has been used to increase the conductivity of lamellar samples. On the other hand, isotropic, bicontinuous morphologies (*e.g.*, double gyroid) featuring three dimensional ion transport pathways do not require domain alignment. However, the gyroid phase occurs over a relatively narrow range of block volume fractions and is often difficult to access

experimentally.[115] In all cases, PEMS prepared with diblock copolymers are expected to be mechanically very weak.

The desired robustness, superior thermal stability, and high ionic conductivity in IL-containing block polymer membranes can be accomplished by designing the PEM with a bicontinuous morphology consisting of a crosslinked mechanical scaffold intertwined with continuous IL-rich conducting nanochannels.[12,124,149,154] This chapter presents development of a proton-conducting PEM using a simple yet versatile one-pot synthetic strategy involving a recently developed polymerization-induced microphase separation (PIMS) method.[12]

Bulk copolymerization of monofunctional and difunctional monomers in the presence of a macro chain transfer agent (macro-CTA) mixed with IL leads to *in situ* cross-linking that kinetically traps a disordered network structure adopted by the growing diblocks, thereby imparting a co-continuous network morphology to the resultant PEM.[131,155] Specifically, reversible addition-fragmentation chain-transfer (RAFT) polymerization was implemented for a controlled growth of styrene (S) and divinylbenzene (DVB) from a poly(ethylene oxide) macro-chain transfer agent (PEO-CTA) in the presence of a stoichiometric protic IL, 1-ethylimidazolium bis(trifluoromethylsulfonyl)imide, [HEIm][TFSI].

PIMS allows direct incorporation of the protic IL into the bicontinuous PEM matrix, yielding isotropic proton conducting pathways of PEO and IL, along with a cross-linked PS network that imparts mechanical integrity and thermal stability to the system. The morphology, ionic conductivity, and the proton transport characteristics of the PIMS PEM were explored. We conclude that the IL selectivity and increased effective segregation between the mechanical phase and the conducting domain enhance the overall conductivity. The PIMS PEMs exhibit long-range, isotropic, continuous conducting and

cross-linked domains with an exceptional combination of ionic conductivity, thermal stability and mechanical robustness, making them promising candidates for high-temperature proton transport applications.

2.2 Experimental Section

Synthesis and Characterization

Poly(ethylene glycol) methyl ether (M_n = 5 kg/mol, $Đ$ = 1.1) was purchased from Sigma Aldrich. The RAFT chain transfer agent *S*-dodecyl-*S*′-(*α*,*α*′-dimethyl-*α*′′-acetic acid)trithiocarbonate (DDMAT) was synthesized as previously reported.[156] The macromolecular PEO-CTA was synthesized by end-functionalization at the hydroxyl terminus of the polymer with DDMAT via an acid chloride intermediate (Figure 2.1). Polymers were characterized by ^{1}H NMR spectroscopy and size exclusion chromatography (SEC). NMR measurements were made on a 500 MHz Bruker HD-500 spectrometer equipped with a cryoprobe. SEC measurements were carried out on a system equipped with an Agilent 1260 pump, multiangle light-scattering detector (Wyatt Dawn DSP-F), and refractive index detector (Wyatt Optilab DSP) for absolute determination of the polymer molecular weights. Complete end-functionalization in PEO-CTA was confirmed through the controlled growth of PEO-*b*-PS linear diblocks ($Đ$ = 1.29), indicated by shift to higher molecular weight (Figure 2.3). The IL was prepared by neutralization of as-purchased (Sigma Aldrich) 1-ethylimidazole (EIm, ≥ 95%) with *N*,*N*-bis(trifluoromethylsulfonyl)imide (HTFSI, ≥ 95%). An equimolar mixture of EIm and HTFSI was heated at 100 °C for 2 to 3 h. Activated charcoal (10 wt%) was added to the IL and mixture was stirred for 24 h to remove impurities. Dicholoromethane was then added and the mixture was filtered. The IL was dried at 70 °C under dynamic vacuum for at least 2 d and was then transferred to an argon atmosphere glove box. The measured melting point of the IL (– 12 °C) agreed well with a previously reported value.[23]

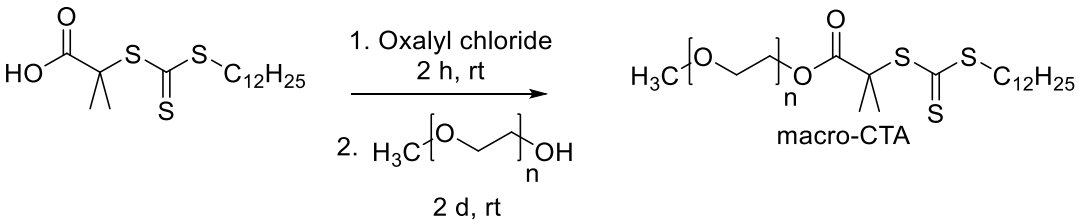

Figure 2.1: Synthesis of macro-chain transfer agent PEO-CTA

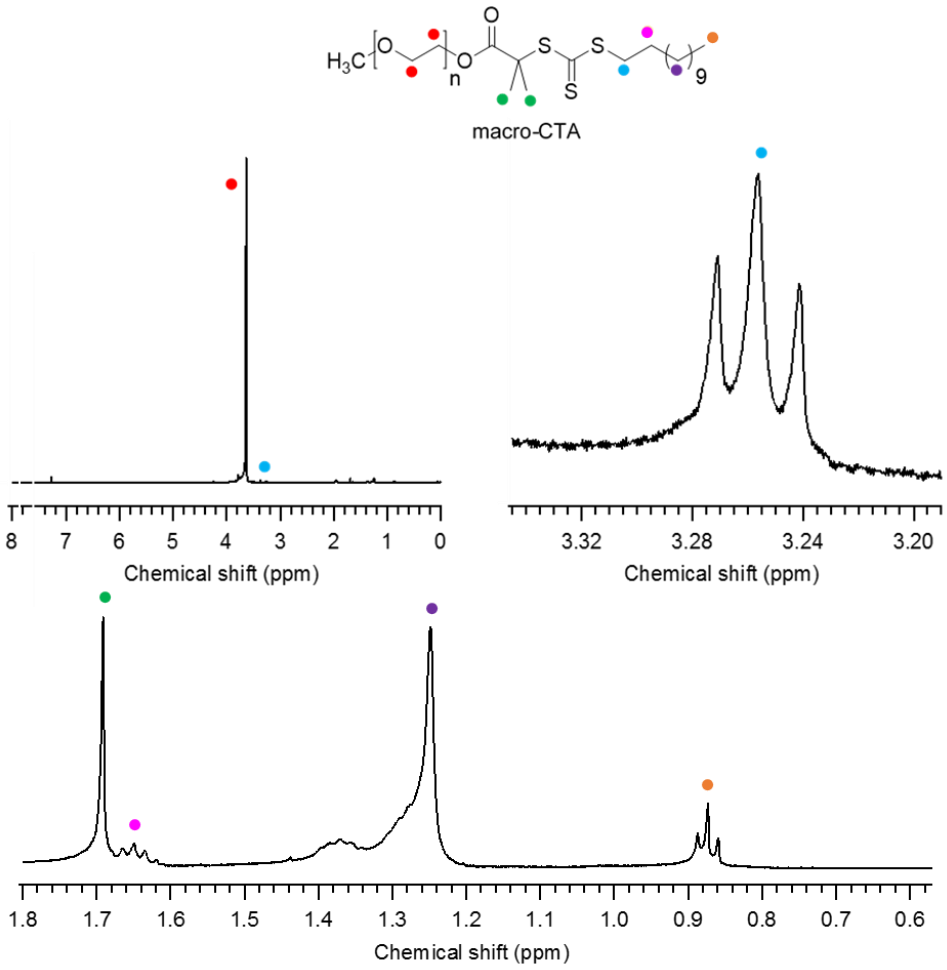

Figure 2.2: ^{1}H NMR ($CDCl_3$, 500 MHz) spectrum of PEO macro-CTA, end-functionalized with DDMAT.

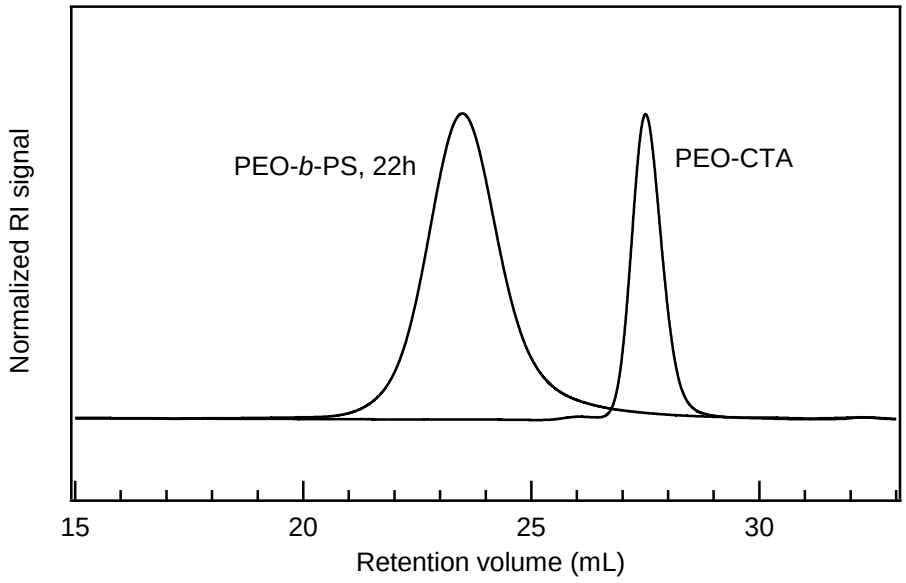

Figure 2.3: SEC chromatograms of PEO-CTA (5 kDa) and PEO-*b*-PS ($Đ$ = 1.29).

Preparation of Polymer Electrolyte Membranes (PEMs)

To develop nanostructured PEMs, reaction mixtures were prepared gravimetrically, typically containing 32 wt% PEO-CTA in a 4:1 molar mixture of styrene to divinylbenzene. A varying amount of IL was added to this reaction solution to achieve a 5–55 overall wt% IL concentration in the resultant PEM (Table 2.1). Styrene (S, 99%, Sigma Aldrich) and divinylbenzene (DVB, tech. grade 80%, Sigma Aldrich) were filtered through an activated alumina column prior to use. The liquid reaction precursor was prepared in glass vials by adding a predetermined amount of IL to PEO-CTA inside a glove box. The monomers (S and DVB) and 2,2′-azobisisobutyronitrile (AIBN) initiator (0.05 *eq*. relative to PEO-CTA) were injected through a rubber septum into the glass vials containing the IL+PEO-CTA mixture outside the glove box. The entire solution was stirred and then heated in sealed glass vials at 120 °C for 24 h (Figure 2.4). The resulting transparent yellow, solid monolith was obtained by breaking the glass vial (Figure 2.5).

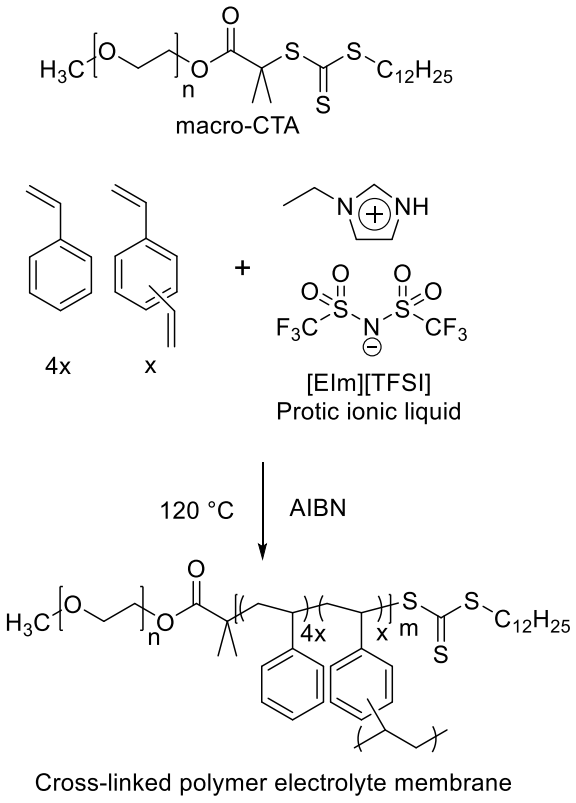

Figure 2.4: Reaction scheme used to synthesize a cross-linked PEM from a 5 kg/mol PEO-CTA and a protic IL [HEIm][TFSI], styrene/divinylbenzene monomer mixture.

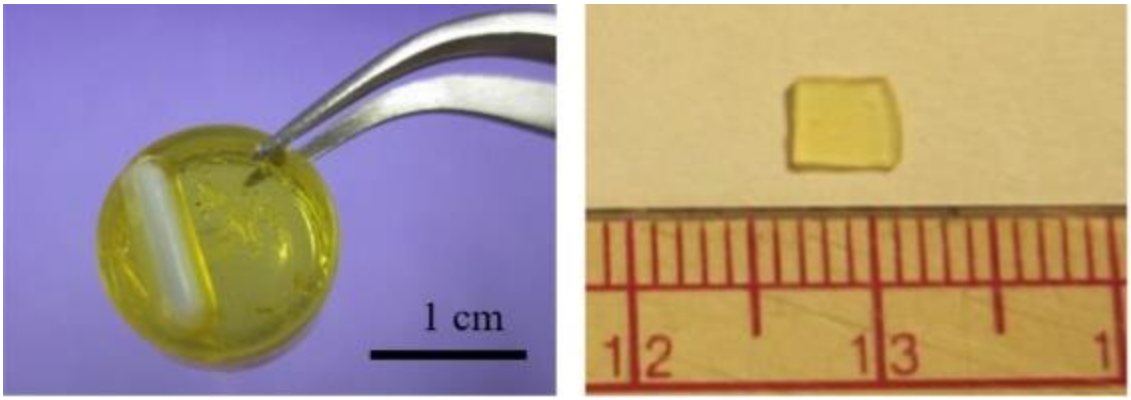

Figure 2.5: Left: Photograph of a typical PE monolith, right: sample used for conductivity experiments.

Differential scanning calorimetry (DSC) measurements were carried out using a TA Instruments Discovery DSC. Samples prepared using aluminum T-zero pans with hermetic

lids were annealed at 180 °C for 10 min, followed by subsequent cooling and heating ramps at 10 °C/min. Thermogravimetric analysis (TGA) of the PEM samples was performed on a TA Instruments Q500 under N_2 at a heating rate of 10 °C/min from room temperature to 450 °C. PEM samples were dried at 50 °C under dynamic vacuum overnight prior to the measurements.

Morphological Characterization

SAXS measurements were performed at the Advanced Photon Source at Argonne National Laboratory using beamlines 5-ID-D and 12-ID-B. The measurements were performed at room temperature using X-rays with a wavelength (λ) of 0.76 Å yielding scattering wavevectors q ($q = 4\pi \sin(\theta/2)/\lambda$, where θ is the scattering angle) in the range of 0.022–1.35 nm^{-1}. SAXS intensity as a function of q was obtained by azimuthally integrating the isotropic two-dimensional scattering patterns.

PEO and IL domains of the PEM were etched to create contrast for direct observation of the morphology via SEM. Following an established etching procedure,[157] chunks of the PEM monolith were immersed into an aqueous solution of 57 wt% hydroiodic acid at 60 °C for 5 d, removed and rinsed in methanol, and dried in an oven for 30 h. The etching procedure resulted in > 95% removal of the PEO and IL by gravimetric analysis, confirming the continuity of the PEO/IL nanochannels. The freeze-fractured surface of the SEM sample was sputter-coated with ~ 1–2 nm Pt and was imaged using high-resolution Hitachi S-4700 FEG-SEM at an accelerating voltage of 5 kV.

Ionic Conductivity

The ionic conductivity of the PEM samples was measured by 2-point probe impedance spectroscopy using a Solartron 1255B frequency response analyzer and an SI 1287 electrochemical interface. Samples for conductivity measurements were prepared by sanding bulk PEM monoliths to uniform thickness (*ca*. 0.5 mm, Figure 2.5) and stored in

an Ar-filled glovebox. Prior to the conductivity measurements, the thin samples were dried overnight at 80 °C under dynamic vacuum, then sandwiched between polished stainless steel electrodes (Figure 2.6a), held together with Kapton tape and inserted into a custom-built heating stage (Figure 2.6c). The heating stage was built using a copper block with a cavity for the sample holder (Figure 2.6d). The heating stage was heated using 90 W nichrome cartridge heaters. In order to minimize heat loss the surrounding, the heating block was insulated with Teflon sheets. A T-type thermocouple measured the temperature of the heating block. Based on the set temperature and the feedback temperature from the heating stage thermocouple, a programmable ramp/soak controller regulated the current supplied to the cartidge heaters using solid state relays. The heating stage and sample were kept in a desiccator to maintain a dry environment. Impedance was measured by applying an alternating voltage with an amplitude of 100 mV over the frequency range 1 – 10^6 Hz.

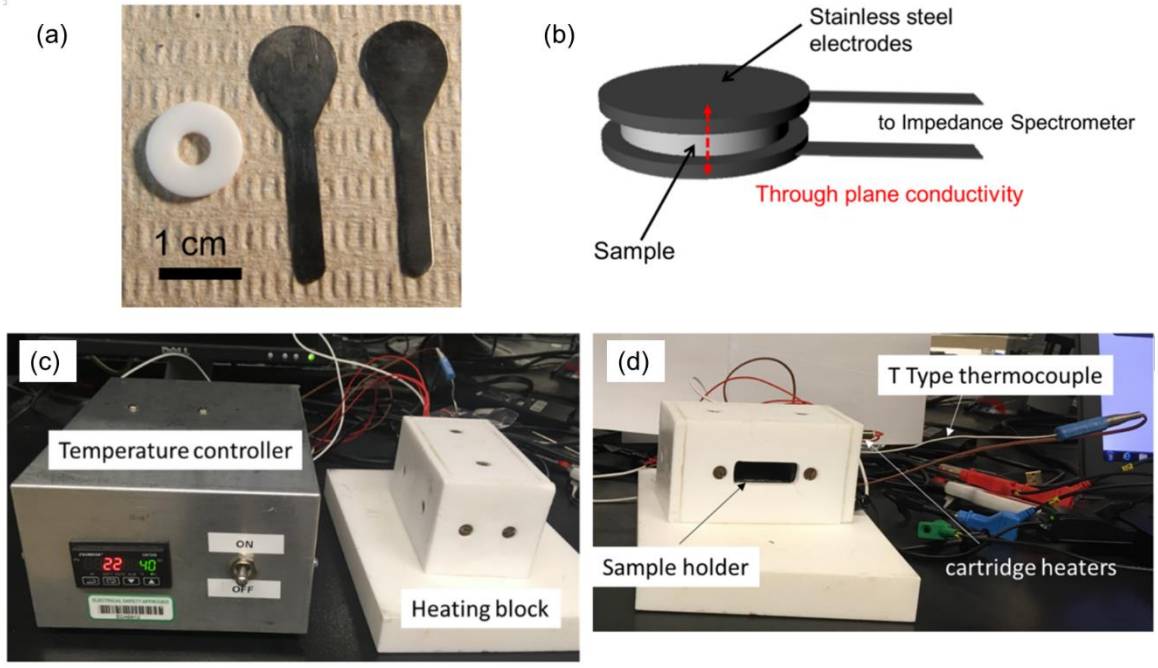

Figure 2.6: (a) Polished stainless steel electrodes used for conductivity measurements. (b) Sample was sandwiched between two stainless steel electrodes. (c) Programmable ramp/soak controllers regulated the current supplied to the resistance heaters of the heating block. (d) The heating stage was built using a copper block with a cavity for the sample holder and insulated with Teflon sheets. The heating stage was heated using 90 W nichrome

cartridge heaters.

Ionic conductivity, σ, was calculated as $t/(Ra)$, where t and a are the thickness and superficial area of the sample and R is the bulk resistance. Bulk resistance was determined from the frequency independent plateau of the real component of the impedance (Z') (representative raw impedance data are shown in Figure 2.7). The measurements were performed starting from 180 °C and cooling to 40 °C in 10 °C decrements. At each temperature the samples were maintained for at least 1 h to allow for thermal equilibration before measurements. Replicate conductivity experiments were performed both for heating (40 to 180 °C) and cooling (180 to 40 °C) cycles to determine whether any water absorption affected the conductivity of the PEMs. The replicate measurements confirmed thermal reversibility for the PEM samples. Ionic conductivity of the IL and a PEO homopolymer + IL mixture was measured using a custom-built conductivity cell, which was maintained under positive Ar atmosphere. In this case σ was calculated as κ/R, where R is the bulk resistance and κ is the cell constant for the conductivity cell, which was calibrated using 0.01 M KCl standard (Fluka, 1.41 mS/cm at 25 °C).[155]

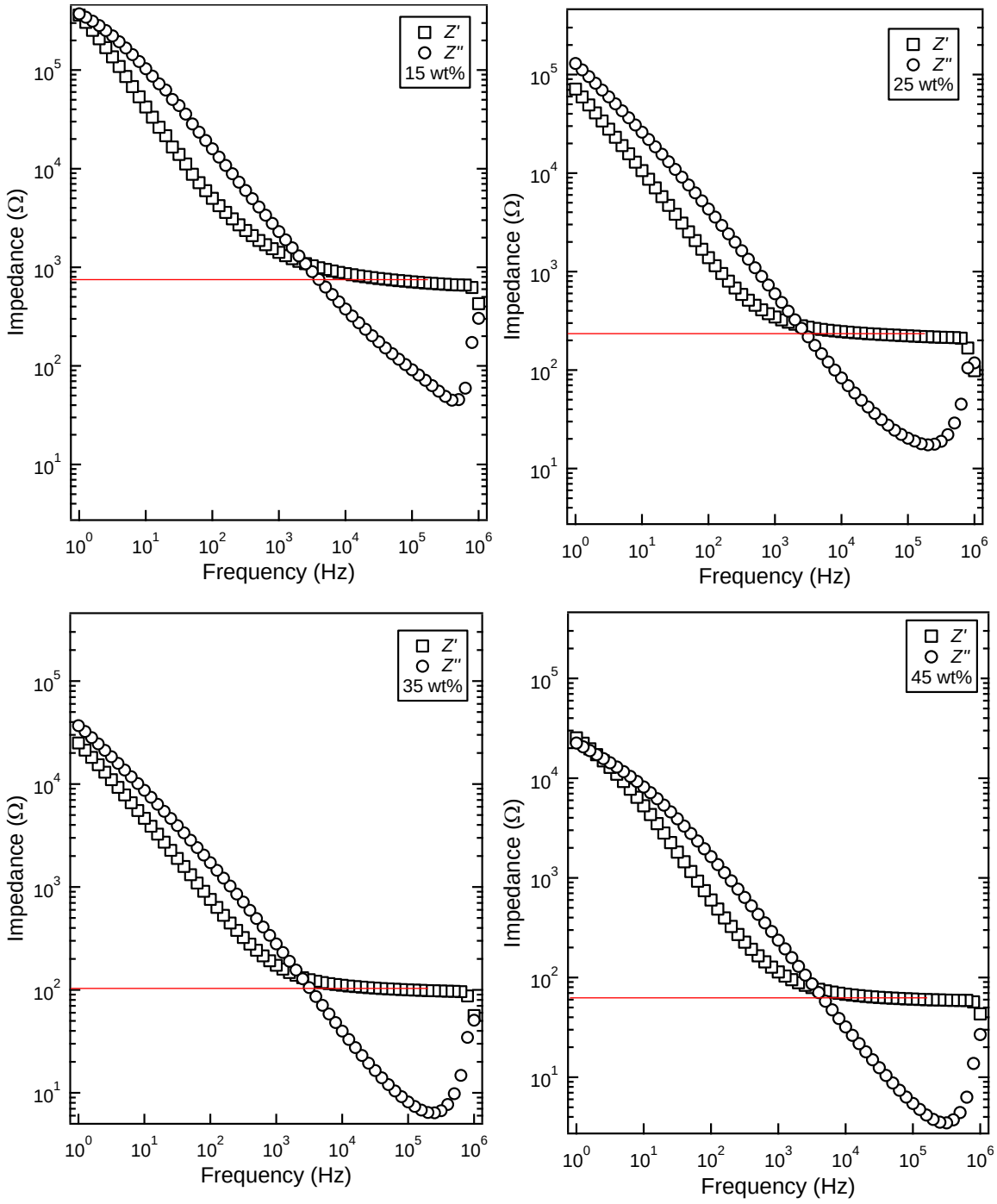

Figure 2.7: Raw impedance data for the PEM samples collected at 60 °C. Squares (□) are *Z′*, circles (○) are *Z″*. The red line denotes the bulk resistance, *R*, used to calculate the conductivity.

Diffusion Coefficient Measurements

A Bruker Avance III 500 MHz NMR spectrometer equipped with a 5 mm Triple Resonance Broadband (TBO) pulsed field gradient (PFG) probe was used to determine the self-diffusion coefficients of $HEIm^+$ and $TFSI^-$ ions confined inside the PEM. The PEM samples were ground into fine powders and loaded into NMR tubes along with d_{26}-dodecane, a poor solvent for the IL. For the PFG-NMR experiments, the "ledbpgp2s" pulse sequence (longitudinal eddy current delay experiment using bipolar gradients acquired in 2D)[158] was used with two different nuclei, ^1H for $HEIm^+$ and ^{19}F for $TFSI^-$ at different temperatures from 298 to 348 K. At each temperature, the sample was equilibrated for at least 30 min before conducting the NMR experiment. The translational diffusion coefficients were obtained by using eq. 2.1:

$$\frac{I}{I_0} = \exp(-\gamma^2 \delta^2 G^2 D(\Delta - \delta/3)) \qquad (2.1)$$

where I/I_0 is the attenuated intensity (I) at various gradient strengths (G) from 2 to 98% of the maximum G (0.47 T/m) normalized to I_0 at $G = 0$, and γ is the gyromagnetic ratio. γ of ^1H and ^{19}F are 42.6 and 40.1 MHz/T, respectively. The diffusion time (Δ) was 100 or 150 ms, and the gradient pulse time (δ) was 4 or 2 ms for both nuclei. The PFG-NMR results were processed by the TopSpin software package (version 3.1) and fitted with eq. 2.1.

Mechanical Response

Tensile bar shaped PEM samples were synthesized by reacting the liquid precursor in Teflon molds at 120 °C. Mechanical response (extensional rheology) of these tensile bars, measuring approximately $50 \times 10 \times 0.8$ mm^3, was analyzed using a TA Instruments RSA-G2 Solid Analyzer. The linear viscoelastic regime was determined by strain sweeps performed at a frequency of 10 rad/s at various temperatures. Frequency sweep experiments were performed at fixed strain amplitude over the frequency range 1 – 100

rad/s for the temperature range 30 – 210 °C under N_2; the sample was equilibrated at a given temperature for at least 10 min. A time-temperature superposition (tTS) master curve was developed by horizontally shifting and aligning the frequency sweep data for the elastic modulus, E'.

2.3 Results and Discussion

Characterization of PEM Morphology

This synthesis strategy enables PEM preparation over a wide IL composition range (5–55 overall wt% [HEIm][TFSI]), thus facilitating optimization in terms of mechanical properties, ionic conductivity and morphology.

Table 2.1: Composition of PEM samples

Sample name	IL (overall wt%)	Composition (vol %)[a]		
		IL	PEO + IL[b]	IL in PEO + IL domain[c]
PIMS-55	55	45	61	74
PIMS-45	45	35	54	65
PIMS-35	35	27	48	56
PIMS-25	25	18	42	43
PIMS-15	15	10	36	28

[a] Composition was calculated based on the following densities (g/cm^3) : ρ_{PSDVB} = 1.05, ρ_{PEO} = 1.06, $\rho_{EImTFSI}$ = 1.43. [b] Volume content of the conducting phase [c] Volume content of the IL in the conducting phase.

Typical room temperature SAXS profiles as shown in Figure 2.8 exhibit a broad principal scattering peak at q^* and a weak higher order shoulder at approximately $2q^*$ in most cases, characteristic of a structured morphology with microphase separated domains, but without long-range periodic order.[130] The position of the primary scattering peak corresponds to the structural length scale of compositional heterogeneities ($d = 2\pi/q^*$). In PEM samples prepared with [HEIm][TFSI] the characteristic length scale between the PEO/IL and P(S-*co*-DVB) domains is 20 – 24 nm, significantly higher than the domain spacing between the PEO and cross-linked PS phase (≈ 12 nm) in samples without the IL.

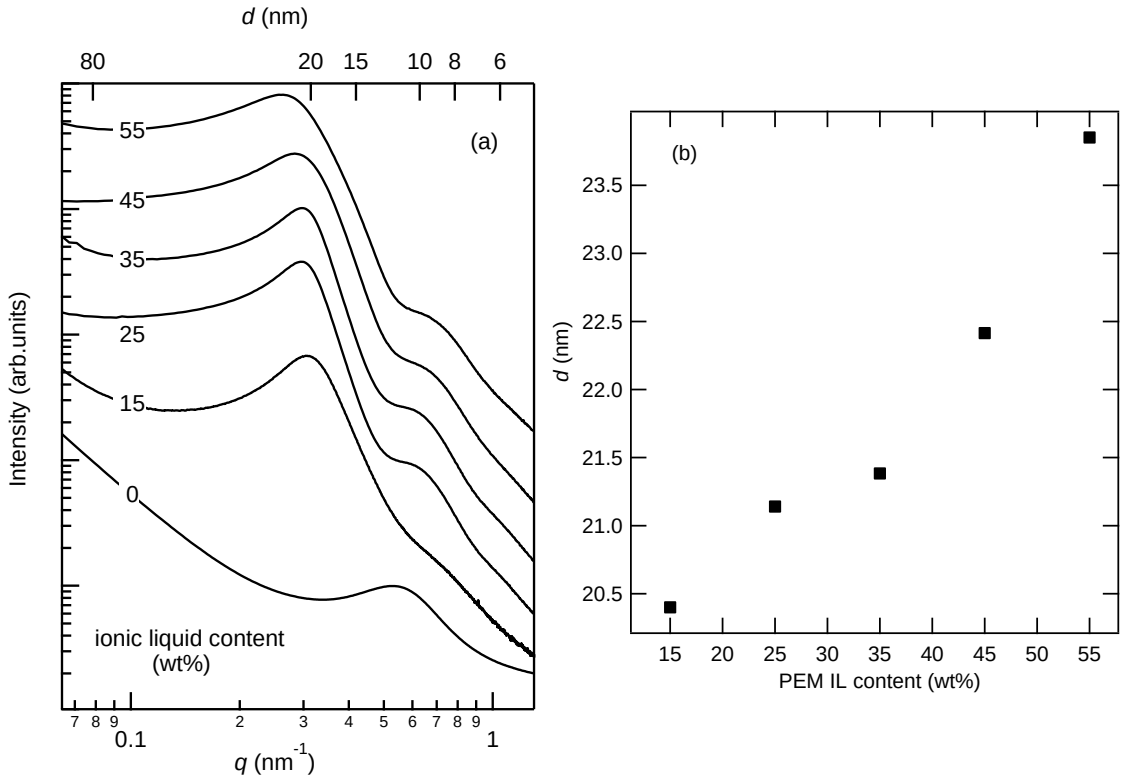

Figure 2.8: (a) Small angle X-ray scattering for PIMS PEM samples prepared with 5 kg/mol PEO-CTA and varying protic IL [HEIm][TFSI] content. (b) The length scale of compositional heterogeneities increases slightly with IL content (reported as overall wt%).

On increasing the IL concentration in the PEM an increase in the average domain spacing between the conducting phase and the cross-linked PS phase was observed, consistent with selective swelling of the PEO domains by the IL and increasing chain stretching at the (PEO+IL)/P(S-*co*-DVB) interface to reduce the unfavorable interactions.[142,159] The interfacial chain stretching can be ascribed to this selective incorporation of the IL and the resultant increase in the effective interaction parameter, χ_{eff}, between P(S-*co*-DVB) and the conducting phase (PEO+IL), compared to between P(S-*co*-DVB) and pure PEO.[103] Higher segregation strength also leads to an increased local order, as indicated by the appearance of a more pronounced shoulder at *ca*. 2q* at higher IL concentrations.

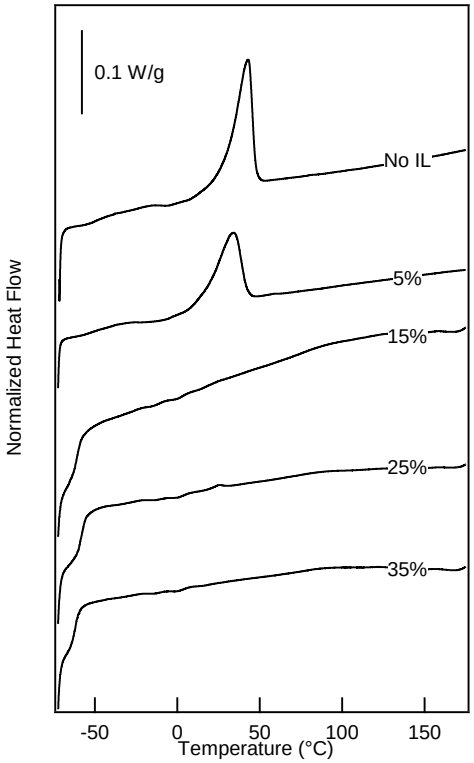

Figure 2.9: DSC thermograms for PEMs with varying IL content (overall wt%). The traces represent the second heating cycle (exothermic flow down). PEO crystallization is suppressed on increasing IL content in the PEM. A distinct glass transition is not observed for the cross-linked PS phase up to 180 °C. The lack of distinct T_g is likely a result of the high cross-link density.

The DSC data for the PEMs are consistent with the protic IL partitioning to the PEO phase to form conducting nanochannels. In PEM samples with low IL content (5 overall wt%) the presence of PEO crystals is evident from the prominent endothermic peak in the DSC traces (Figure 2.9). On increasing the IL content, the suppression of PEO crystallinity is evident from the absence of any endothermic peaks; in addition, the DSC results reveal the T_g of the PEO + IL phase (*ca*. –60 °C). The melting point of the protic IL was not detected in the DSC traces, presumably due to the crystallization suppression caused by the confinement of the IL into nanodomains.

SEM micrographs (Figure 2.10) of freeze-fractured surfaces of PEMs subjected to PEO/IL etching conditions and coated with ~ 1–2 nm Pt layers show uniformly distributed,

interconnected pores, consistent with the formation of a bicontinuous morphology with interpenetrating domains of cross-linked PS and PEO/IL conducting phases. The pores/voids correspond to regions of PEO/IL prior to etching, whereas the bright regions represent the unetched cross-linked PS domains. As expected, the pore volume in the etched samples increases with the IL content (panels (b) and (c) of Figure 2.10). The absence of long-range order is in agreement with the absence of higher order SAXS scattering peaks. The sample spanning bicontinuous nature of the PIMS PEM morphology was also confirmed by the agreement (within experimental error) between the weight loss during the etching process and the corresponding mass fraction of PEO + IL phase in the PEM. The SEM images thus corroborate the SAXS results, highlighting the existence of a bicontinuous morphology in the PEM system consisting of microphase separated domains that lack long-range order.

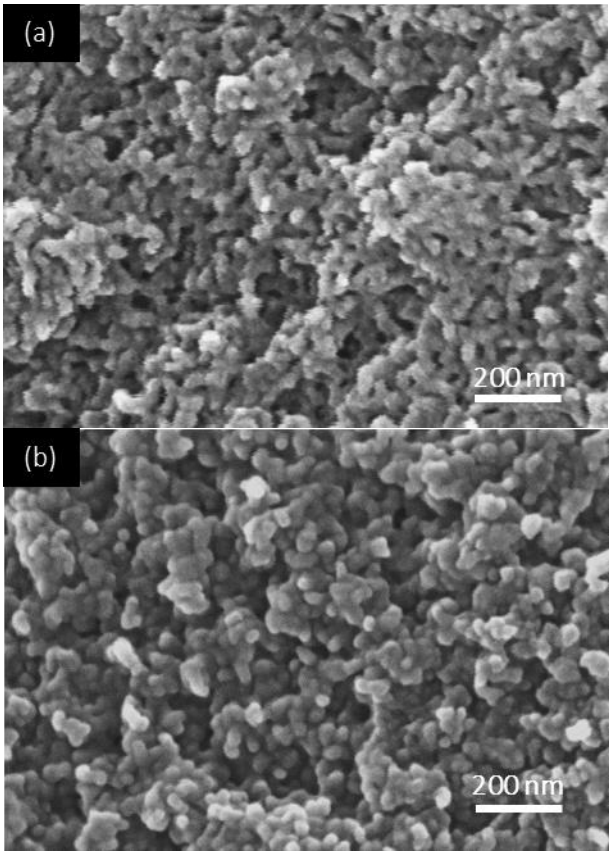

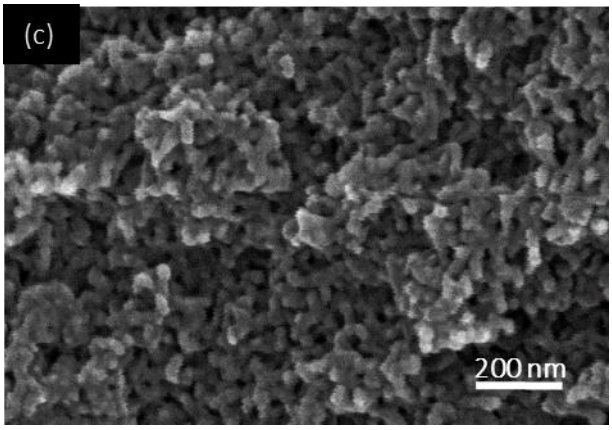

Figure 2.10: Scanning electron micrographs of PIMS PEM samples after etching the PEO domains and the protic IL [HEIm][TFSI]. PEM with IL content of (a) 0 wt% (No IL), (b) 35 overall wt% and (c) 55 overall wt%. Freeze-fractured samples were coated with 1 – 2 nm of Pt prior to imaging. The bright regions in the micrographs are the unetched polystyrene domains. Uniformly distributed, interconnected pores are indicative of the bicontinuous morphology.

Ionic Conductivity

The ionic conductivity of PEM samples prepared with overall IL concentrations of 15 to 45 wt% was measured as a function of temperature (Figure 2.11). Conductivity of the PEMs increases with both increasing temperature and IL content. Table 2.1 summarizes the concentrations of all the species in the various samples and the composition of the PEM in terms of the vol. % of the conducting phase (PEO + IL) and the vol. % of the IL in the overall PEM and in the conducting phase. The conductivity data were fit to the Vogel-Fulcher-Tammann (VFT) relationship,

$$\sigma = \sigma_0 \exp\left(\frac{-B}{T - T_0}\right) \tag{2.2}$$

where the pre-factor, σ_0, represents the asymptotic conductivity of the PEM system at infinite temperature, B is a pseudo-activation energy, and T_0 is the Vogel temperature, at which all the molecular motion is frozen and the conductivity approaches zero.[11]

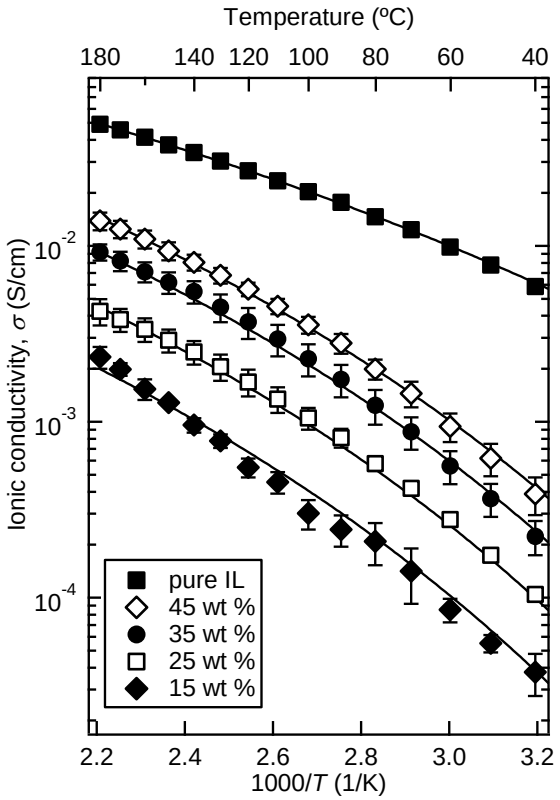

Figure 2.11: Ionic conductivity of PIMS PEM samples with varying content of the protic IL, [HEIm][TFSI] (reported as overall wt%). Solid lines are fits to the VFT functional form; VFT parameters are provided in Table 2.2. Error bars (in some cases smaller than the data points) are one standard deviation based on at least three measurements. The IL conductivity (■) of pure [HEIm][TFSI] is also shown for reference.

Figure 2.11 summarizes the ionic conductivity of PEMs in comparison to the protic IL. The choice of [HEIm][TFSI] as a model protic IL was motivated by its favorable thermal properties (glass transition temperature $T_g \approx -89$ °C,[23] high decomposition temperature $T_d \approx 385$ °C) and high ionic conductivity. PIMS-45 (a PEM sample with 45 wt% IL) exhibited an impressive ionic conductivity, on the order of 14 mS/cm at 180 °C. It is noteworthy that PIMS PEMs with even lower IL content showed appreciable ionic conductivity, in contrast to some reports in the literature.[10,25] For example, PIMS-15 consists of 10 overall vol % IL, which is lower than the theoretical percolation threshold (≈ 15 vol %) required to form a sample-spanning network.[9] Nevertheless, this PEM exhibited substantial ionic conductivity (◆ in Figure 2.11). This result highlights the fact

that network defects such as dead ends and isolated domains are rare in PIMS PEMs, and the PEO + IL phase form continuous conducting nanochannels.

Table 2.2: VFT Parameters of the conductivity profiles in Figure 2.11

IL	VFT Parameters		
(overall wt%)	σ_0 (S/cm)	B (K)	T_0 (K)
[HEIm][TFSI]	0.75	871	135
PEO + IL*	0.45	955	148
45	0.54	1068	167
35	0.40	1076	168
25	0.15	1033	170
15	0.11	1163	172

To assess the long-range connectivity of the conducting channels as suggested by the SEM images, the conductivity of the PIMS-35 PEM sample was compared to σ_h, the conductivity of a bulk, homogeneous PEO + IL electrolyte (⊗ in Figure 2.12). In the absence of any network defects and IL dead pockets, the PEM conductivity (σ) can be expressed using a tortuosity model as a fraction of the conductivity of a bulk, homogeneous electrolyte (σ_h) with same PEO/IL composition as the conducting phase of PEM, by

$$\sigma = \sigma_h \frac{f_c}{\tau} \tag{2.3}$$

where f_c and τ are the volume fraction and the tortuosity of the conducting phase (PEO + IL), respectively. In the case of PIMS-35, $f_c = 0.48$ (Table 2.1). The tortuosity parameter, τ, accounts for the relatively longer path ions have to travel in comparison to the distance between the electrodes. τ values for molecular transport in a co-continuous network are expected to be between 1.5 and 3.[110,160,161] As seen in Figure 2.12, the measured ionic conductivity of PIMS-35 (●) is generally consistent with eq 2.3 (represented by the red-shaded region) and the expected range of the tortuosity ($1.5 \leq \tau \leq 3$). This result indicates that the conducting nanochannels are predominantly continuous, with few network defects

such as dead-ends or grain boundaries. The result also highlights that the rigid cross-linked PS phase does not significantly impede the ion transport, implying a relatively narrow interface between the domains.

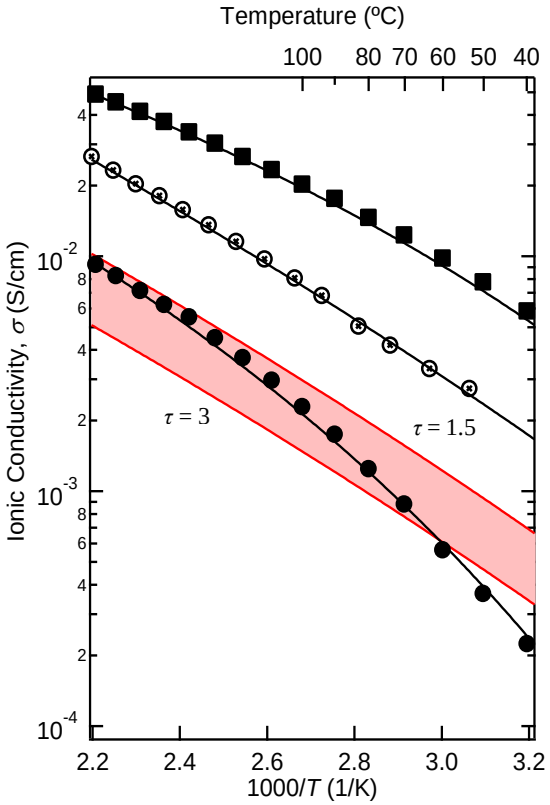

Figure 2.12: Comparison of PIMS-35 (35 wt% IL) conductivity (●) to the tortuosity model (eq. 2.3). The homogeneous electrolyte (⊗) was prepared with a 5 kg/mol PEO homopolymer/[HEIm][TFSI] mixture with the same composition as the conducting phase (PEO+IL) in PIMS-35 at 56 vol % IL. The red region is defined according to eq. 2.3 with f_c = 0.48 (vol. fraction conducting phase in PIMS-35) and $1.5 \leq \tau \leq 3$. IL conductivity (■) of pure [HEIm][TFSI] is also shown for reference.

The ionic conductivity of the PEM is proportional to that of the homogeneous electrolyte at higher temperatures (> 100 °C), but drops more quickly at lower temperatures. The tortuosity model ignores the fact that the PEO chains in the PEM are tethered to the cross-linked PS domains. At lower temperatures, the close proximity of the glassy PS phase likely slows down the relaxation dynamics of the PEO chains in the PEM conducting phase, and therefore lowers the ion mobility and the overall conductivity

further. Nevertheless, the long-range connectivity of the conducting nanochannels as corroborated by the tortuosity model imbues the PIMS PEM with an exceptional ionic conductivity.

Continuous Conducting Pathways

The model protic IL [HEIm][TFSI] was selected based on (a) its miscibility with S/DVB monomers to form a homogeneous reaction precursor, and (b) the desired incompatibility with polystyrene. Polystyrene with $M \geq 3$ kg/mol has been reported to be immiscible with 1-ethyl-3-methylimidazolium bis(trifluoromethylsulfonyl)imide, [EMI][TFSI] (Figure 2.13), an aprotic IL chemically similar to [HEIm][TFSI].[113,142] Reacting the liquid precursor at 120 °C results in controlled growth of P(S-*co*-DVB) from PEO-CTA by RAFT polymerization, that leads to partitioning of the IL into microphase separated domains. Simultaneous growth and crosslinking of the polystyrene (PS) block kinetically arrests the system in a co-continuous morphology that is locally correlated but does not exhibit long-range order.[131,155] During the reaction, IL becomes immiscible with the PS phase and partitions to the PEO-rich regions to form sample spanning continuous conducting nanochannels.

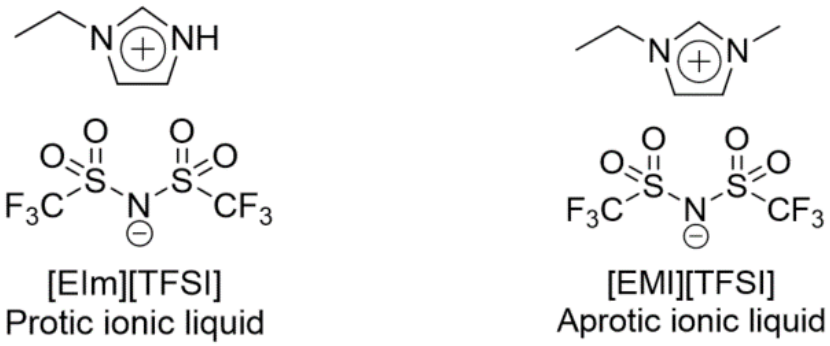

Figure 2.13: Ionic liquids used in the comparative study.

In contrast to most block polymer/IL electrolyte systems,[6,151] the PIMS strategy allows direct incorporation of the IL into conducting nanochannels, thus eliminating post-

polymerization steps such as IL doping and domain alignment to achieve appreciable ionic conductivity. The conductivity of self-assembled diblock PEMs is often compromised by grain boundaries and isolated domains.[162] Lee, et al. developed PEMs by incorporating a protic IL, diethylmethylammonium trifluoromethanesulfonate into a sulfonated polyimide matrix.[25] The authors observed that PEM with 33 wt% and 55 wt% IL content membranes exhibited low conductivities and a sudden rise in the conductivity of the system for IL contents above 67 wt%. The authors attributed this sudden rise to the establishment of well-connected ion-conducting channels in membranes with IL content higher than 67 wt%. In contrast, these PIMS PEMs exhibited excellent ionic conductivity at IL contents as low as 15 wt%. In addition, the gradual increase in the ionic conductivity with the IL content highlight that sample spanning continuous conducting channels are present in the system, irrespective of the IL content.

PIMS PEMs exhibit among the highest ionic conductivities compared to other systems designed using non-ionic polymer matrices and equivalent IL content, such as poly(styrene)-*b*-poly(2-vinyl pyridine) (PS-*b*-P2VP) diblocks incorporating a protic IL, imidazolium bis(trifluoromethylsulfonyl)imide [Im][TFSI],[10] and poly(vinylidene fluoride-*co*-hexafluoropropylene)/ionic liquid mixtures.[23] Sulfonated PEMs are fundamentally different from PIMS PEMs, as the chemically tethered sulfonic groups along the polymer backbone facilitate proton exchange with the IL and enhance the overall conductivity of the system.[5] In contrast, the PEO domains in the PIMS PEMs appear to be just a “container” for the protic IL, and the proton transport in the composite material must be predominantly via the vehicular mechanism.

Sulfonated PEMs in the hydrated form, such as commercial humidified perfluorosulfonic acid polymer membranes like Nafion®, have the sulfonate groups affixed to the polymer backbone and therefore have proton transference number $t^+ = 1$. It

is noteworthy that PIMS PEMs also exhibit a high proton transference number, on the order 0.7. Furthermore, the anhydrous nature of PIMS PEMs facilitates proton transport even at elevated temperatures where humidified membranes encounter difficulties. The proton transference number of PIMS PEMs can be raised further by introducing excess Brönsted base (1-ethylimidazole), thus increasing the extent of proton transport by the faster proton-hopping or Grotthuss mechanism. However, IL systems with base-rich compositions have relatively poor thermal stability, and are therefore less suitable for high-temperature operation.

Another issue encountered by PEMs incorporating ILs for fuel cell applications is the possible leaching of the electrolyte by the water, a by-product of the electrode reactions and resultant decrease in the ionic conductivity.[15,163] [HEIm][TFSI], used in the current study, and other ILs with $TFSI^-$ anions are expected to be more stable during a fuel cell operation as they are relatively more hydrophobic than ILs designed with tetrafluoroborate, BF_4^- and hexafluorophosphate, PF_6^- anions.[79] Leaching of the ionic liquid from the PIMS PEMs was studied by immersing the membranes in de-ionized water at room temperature. PEM samples were dried in a vacuum oven at 80 °C for 1d, weighed and then immersed in 20 ml water for certain time. At the end of the test, the PEM samples were thoroughly dried in a vacuum oven at 80 °C for 2d and then weighed to determine the weight loss in the sample. PEM samples lose all the ionic liquid after 300 minutes of immersion time (Figure 2.14).

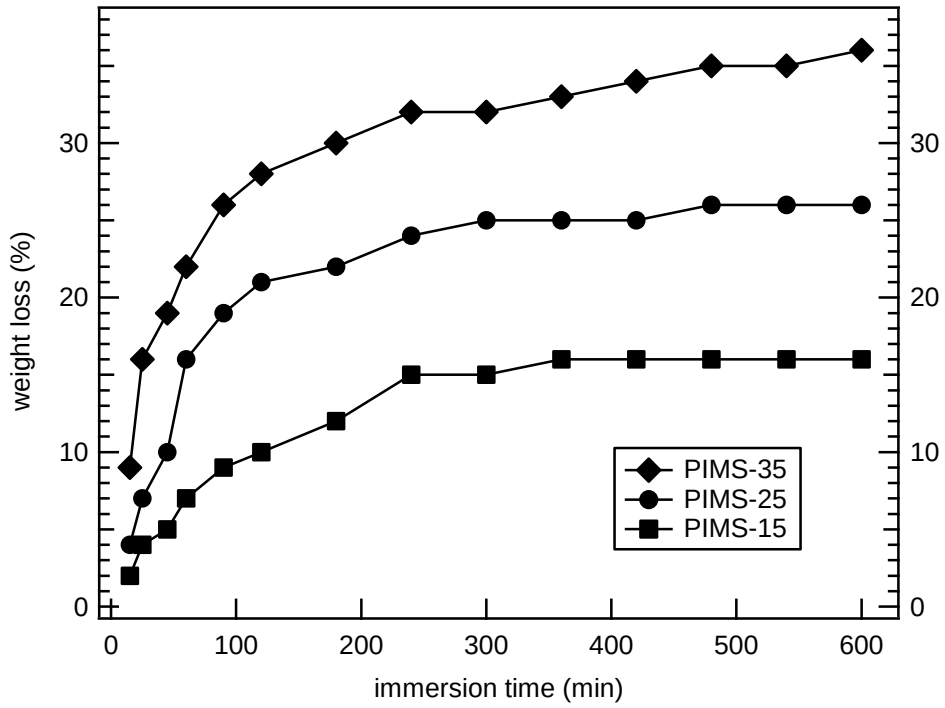

Figure 2.14: Weight loss observed in PIMS PEM samples as a function of immersion time in water.

Proton Transport Characteristics

Impedance spectroscopy reflects the contributions of both ions to the overall ionic conductivity of the PEM sample, whereas only the cation contributes to the desired proton conduction. The proton conductivity can be estimated by identifying the proton transference number, t^+, given by

$$t^+ = \frac{D^+}{D^+ + D^-} \tag{2.4}$$

where D^+ and D^- are the diffusion coefficients of the proton and the anionic species.[25] Owing to the highly acidic nature of HTFSI ($pK_a = -10$),[164] it is reasonable to assume that all EIm species in a IL mixture with stoichiometric amounts of acid and base are in the protonated form.[15] The PFG-NMR experiments with a ^{1}H probe provided the diffusion

coefficients of the C–H proton, and the exchangeable N–H proton of the $HEIm^+$ cation or the D^+ in PIMS PEM (Figure 2.15). In the absence of any free base (*i.e.*, EIm) the proton conduction in the stoichiometric protic IL predominantly occurs via a vehicle mechanism governed by the transport of the $HEIm^+$ cations.[23,25]

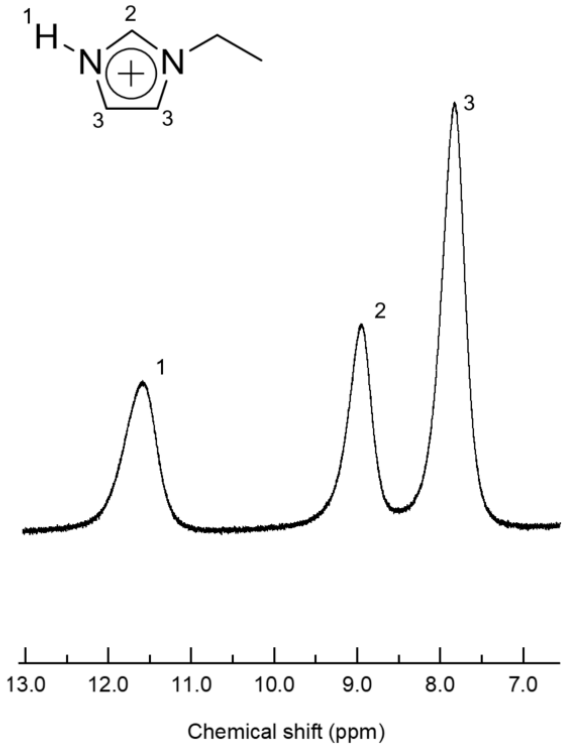

Figure 2.15: ^1H NMR spectrum of PIMS-35 PEM at 53 °C. The spectrum exhibits three distinct chemical shifts for the $HEIm^+$ protons: one for the exchangeable N–H proton (1) and two for C–H protons (2,3).

In the case of the PIMS-35 sample, the measured diffusion coefficients of the C–H and N–H protons of the $HEIm^+$ are almost the same (Figure 2.16), indicating that proton transport in the PEM basically occurs via the vehicle mechanism. PFG-NMR experiments with a ^{19}F probe provided the diffusion coefficient of the fluorine atoms on the $TFSI^-$ anion, D^-. A typical example of I/I_0 as a function of $\gamma^2\delta^2G^2D(\Delta - \delta/3)$ is shown in Figure 2.17a, where the slopes of the plots provide the D^+ and D^- diffusion coefficients.

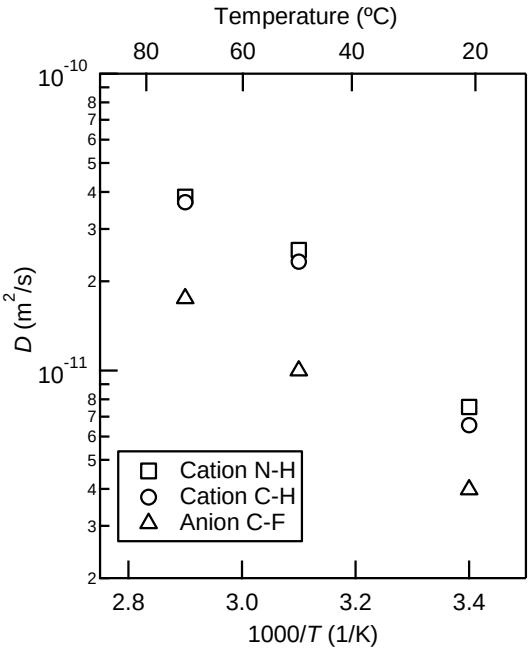

Figure 2.16: Diffusion coefficients, *D*, of cation C–H and N–H protons and anion ^{17}F as a function of temperature for a PIMS PEM with 35 overall wt% IL measured with PFG-NMR. The graph represents the diffusion coefficient data enumerated in Table 2.3.

In all the PFG-NMR experiments, d_{26}-dodecane was added to a NMR tube loaded with a fine powder of PEM to achieve better locking and shimming. d_{26}-dodecane is a poor solvent for the IL, the cations and the anions were therefore trapped inside the conducting phase of the PEM, and the measurements represent the diffusion coefficients of the ionic species in a PEM environment with tortuous conducting pathways. In case of the experiments performed using d_{26}-dodecane solvent, the IL is contained inside the PEM. The log signal attenuation decays linearly with $\gamma^2\delta^2G^2D(\Delta - \delta/3)$ (Figure 2.17a), i.e., a single diffusion coefficient value is observed for the ionic species. In contrast, using D_2O, two apparent diffusion coefficients are obtained from the initial and the final slopes of the decay curve (Figure 2.17d). The two diffusion values indicate that some IL leaches into the solvent. The slower diffusion coefficient represents the cations present inside the tortuous

conducting pathways of the PEM, whereas the cations leaked into the solvent diffuse at a higher rate.

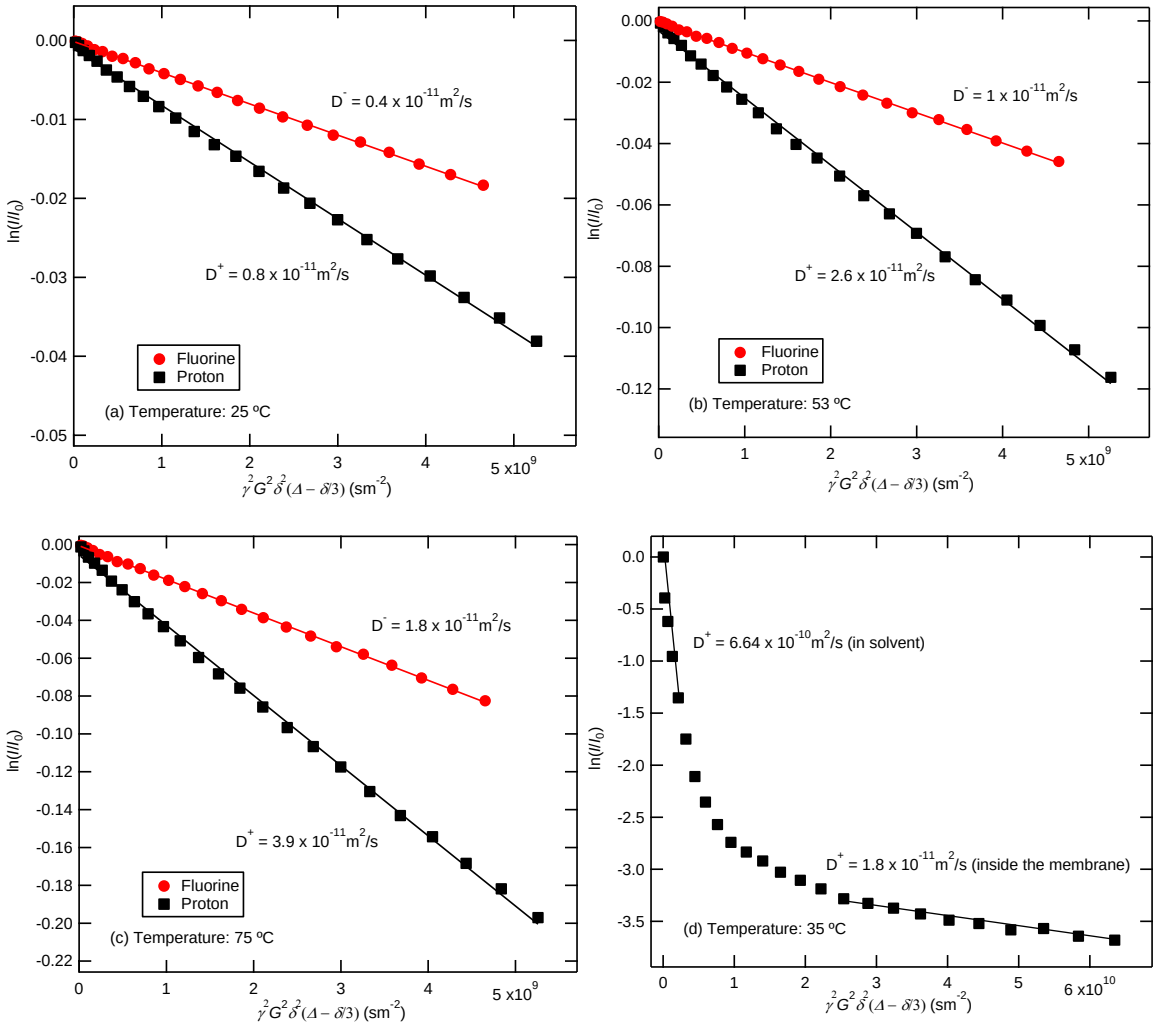

Figure 2.17: PFG-NMR data and fits for the IL cation and anion in (a) d_{26}-dodecane solvent at 25 °C, (b) d_{26}-dodecane solvent at 53 °C, (c) d_{26}-dodecane solvent at 75 °C, and (b) D_2O solvent at 35 °C.

D^+, D^- and the calculated t^+ of PIMS-35 are listed in Table 2.3. As expected, the cation diffuses more rapidly than the bulky anion at all experimental temperatures.[165] The proton transference number of the PEM is a weak function of temperature, indicating that the activation energy for the diffusion of the cation and the anion is similar (Figure 2.16). In a separate experiment, t^+ of pure [HEIm][TFSI] at 25 °C was calculated to be 0.62. PIMS-

35 exhibits an average transference number of about 0.7, which is slightly higher than the IL, possibly due to the presence of anionic aggregates in the PEM system.[52,151] The ionic conductivity of PIMS-45 at ~180 °C is ≈ 14 mS/cm (◇ in Figure 2.11). After accounting for t^+ (≈ 0.7), the highest proton conductivity at ~180 °C of the samples prepared to date is nearly 10 mS/cm.

Table 2.3: Proton and anion diffusion coefficients, and transference number of PIMS-35

Temperature (°C)	D^+ (m^2/s) ($\times 10^{-11}$)	D^- (m^2/s) ($\times 10^{-11}$)	t^+
25	0.8	0.4	0.67
53	2.6	1.0	0.72
75	3.9	1.8	0.68

Figure 2.18 compares σ of PIMS-35 (○) measured by impedance spectroscopy and σ calculated using diffusion coefficients (■) from PFG-NMR experiments via the Nernst−Einstein equation:

$$\sigma = \frac{F^2}{RT}\left(c^+ D^+ + c^- D^-\right) \tag{2.5}$$

where c^+ and c^- are the molar concentration of $HEIm^+$ and $TFSI^-$, respectively, F is Faraday's constant, R is the gas constant and T is temperature. In the calculation of σ using eq. 2.5 we assume that all the ionic species are fully dissociated. The Nernst−Einstein equation over-predicts the measured total conductivity of the PEM by a factor of 3 to 4. The discrepancy is likely attributed to formation of ion pairs and aggregates with zero effective charge that do not contribute ion conduction.[151] At lower temperatures, the increased overestimate of the PEM ionic conductivity suggests higher extent of ionic aggregation in the conducting phase.

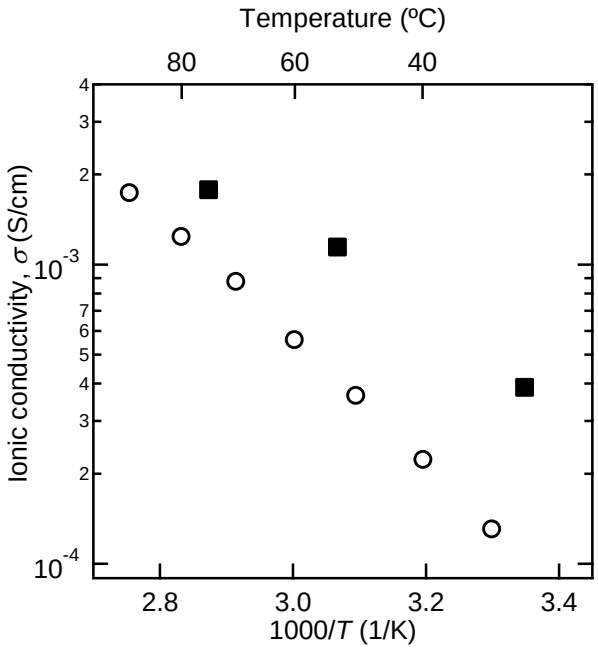

Figure 2.18: Measured ionic conductivity σ (○) and σ calculated using PFG-NMR diffusion coefficients via the Nernst−Einstein equation (■)of PIMS-35, a PEM with 35 wt% IL overall content.

Segregation Strength and IL Selectivity

To assess the effect of the nature of the IL on the PEM morphology, a comparative study was performed with PEMs incorporating an aprotic IL, [EMI][TFSI] (Figure 2.13). Key observations made from the comparative SAXS data (Figure 2.19) are as follows: (i) For the same IL content, the characteristic length-scale is larger for the protic IL PEMs, and (ii) protic IL PEMs exhibit more prominent higher-order features. These observations indicate that the effective interaction parameter between the conducting phase and the cross-linked PS phase is larger in the case of a protic IL PEM. Consequently, the more hydrophilic IL [HEIm][TFSI] partitions more strongly into the PEO phase, increasing the interfacial chain stretching to minimize the unfavorable interactions between the IL and the PS phase, thereby yielding a larger average domain spacing.[166]

Similarly, increases in the domain purity and the scattering intensity result in more pronounced higher order features in the scattering profile. Hoarfrost and Segalman made a

similar observations about the domain spacing while examining poly(styrene)-*b*-poly(2-vinyl pyridine) (PS-*b*-P2VP) diblocks incorporating a protic IL, [Im][TFSI] and an aprotic IL, [EMI][TFSI].[10] The domain spacing in PIMS PEM is ultimately determined by the type and concentration of the IL, the molar mass of the polymer blocks, and the extent of cross-linking. In addition to larger domain spacings, the relatively higher degree of segregation in PIMS PEMs with a protic IL ensures narrower interfaces, thus facilitating ion transport and enhancing the overall performance.

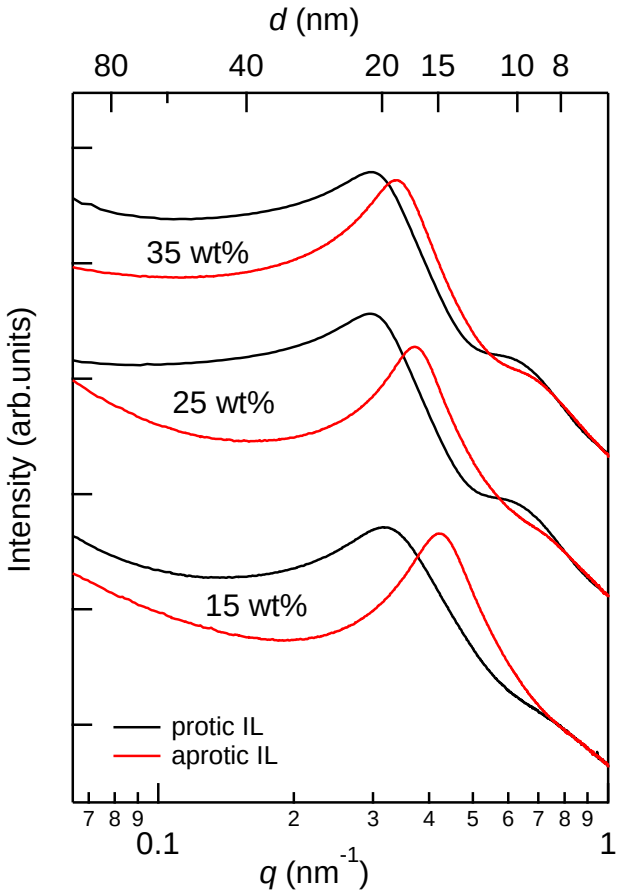

Figure 2.19: Small angle X-ray scattering data for PIMS PEM samples prepared with 5 kg/mol PEO-CTA and varying protic IL [HEIm][TFSI] (black traces) and aprotic IL [EMI][TFSI] (red traces) (overall wt%) content.

The ionic conductivity of a PIMS PEM is determined by the number of the dissociated ions, ionic mobility and the charge on the ionic species. The measured ionic conductivity

of the PEMs increases more rapidly in comparison to the increment in IL concentration (Figure 2.11). For example, the overall IL concentration in the PEM increases about 3.5-fold from PIMS-15 to PIMS-45, while the conductivity increases by a factor of *ca*. 12 at 100 °C. The observed increase in the conductivity is likely due to a combination of factors. The volume fraction of the IL in the conducting phase increases from 28 % for PIMS-15 to 65% for PIMS-45, thus diluting the PEO chains and increasing the ionic mobility and the intrinsic conductivity of the PEO/IL phase. Another important factor is the increase in domain purity, a consequence of increase in the segregation strength between the conducting PEO/IL domains and the glassy PS domains with increasing IL content.[10] At low IL concentrations, a diffuse interface between the PS domains and conducting phase might increase the effective viscosity of the conducting channels. Overall, increasing the IL content increases the mobility and concentration of the ionic species, while concurrently leading to a narrower interface between the insulating and conducting pathways.

Mechanical Response and Thermal Stability

The highly cross-linked PS mechanical scaffold provides the PIMS PEMs with superior mechanical properties in comparison to analogous block polymer systems incorporating ILs or other salts.[92,114] Figure 2.20 shows the elastic modulus of the PEM samples (at 10 rad/s frequency) as a function of temperature. Throughout the experimental temperature range (30 – 210 °C) the PEM samples behave as high modulus solids. The tensile elastic modulus (E') of the PIMS-35 PEM sample gradually drops from about 110 MPa at 30 °C to about 7 MPa at 210 °C. Samples with lower IL content (15 and 25 wt%) were glassy and very brittle. As the IL content in the PEM samples increases, the volume fraction of the mechanical phase decreases, softening the PEM samples, as evident from the drop in tensile elastic modulus (E') especially at lower temperatures.

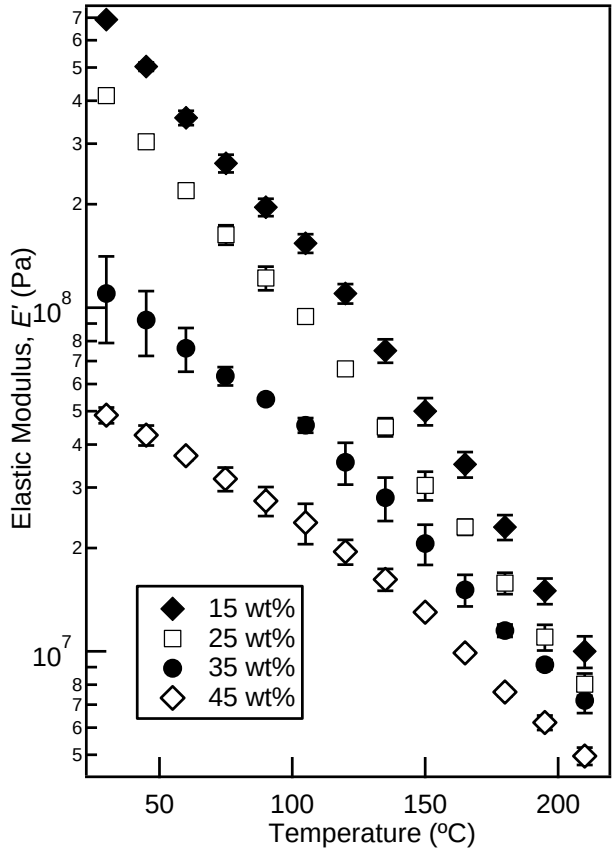

Figure 2.20: Linear elastic tensile modulus of PEM samples with varying IL content. The data points represent *E′* at 10 rad/s, and were extracted from isothermal frequency sweeps.

The tTS master curves (Figure 2.21a), developed by horizontally shifting the raw frequency sweep data, highlights that the mechanical response of the composite PEMs is primarily governed by a single phase, the cross-linked P(S-*co*-DVB) network. The mechanical response corroborates the presence of an isotropic sample spanning continuous PS network. The frequency sweeps (Figure 2.21a) do not exhibit any distinct T_g corresponding to the cross-linked PS phase, consistent with the DSC measurements up to 175 °C (Figure 2.9).

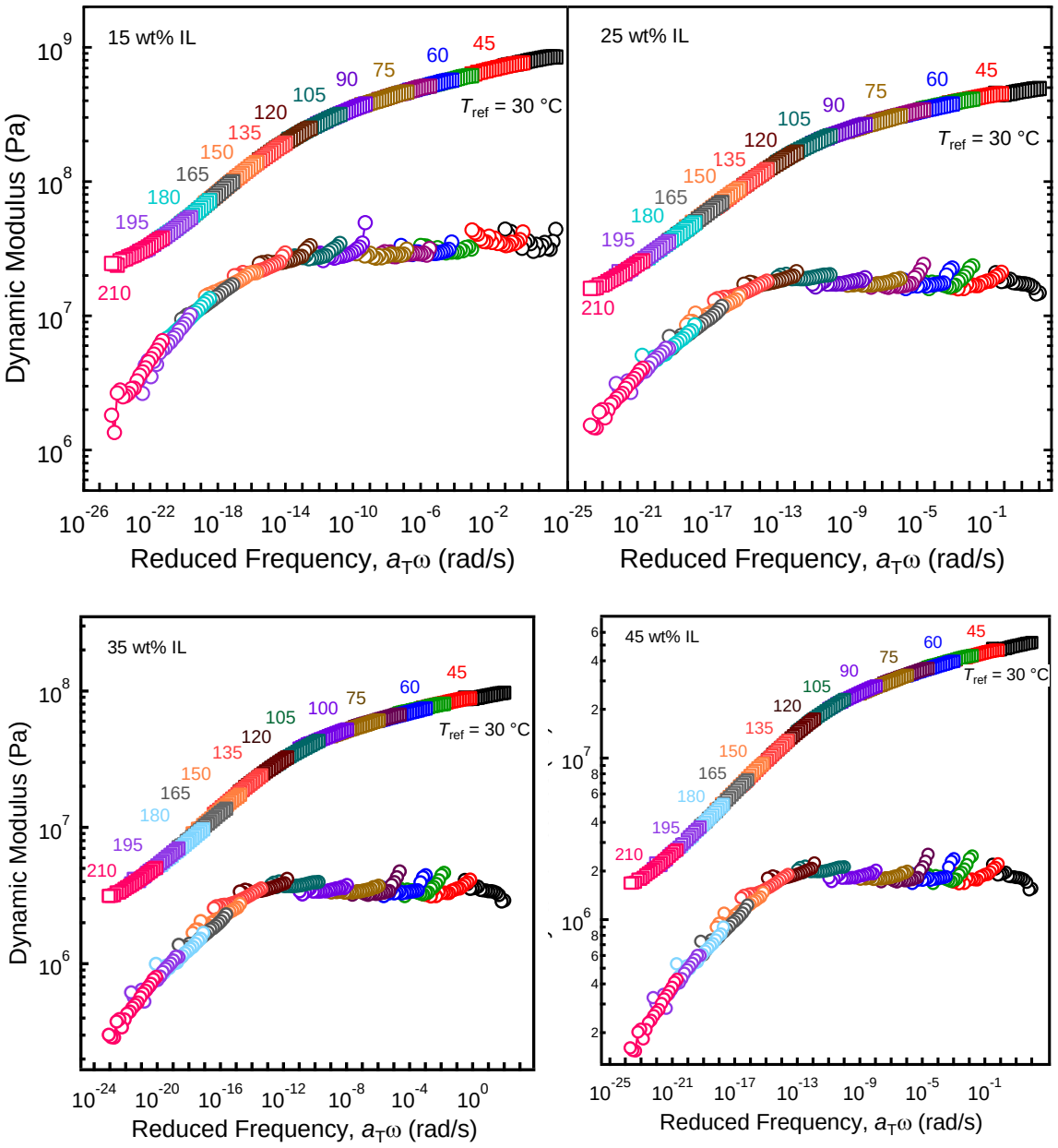
15 wt% IL
25 wt% IL
35 wt% IL
45 wt% IL
T_{ref} = 30 °C
Dynamic Modulus (Pa)
Reduced Frequency, $a_T\omega$ (rad/s)
45
60
75
90
105
120
135
150
165
180
195
210

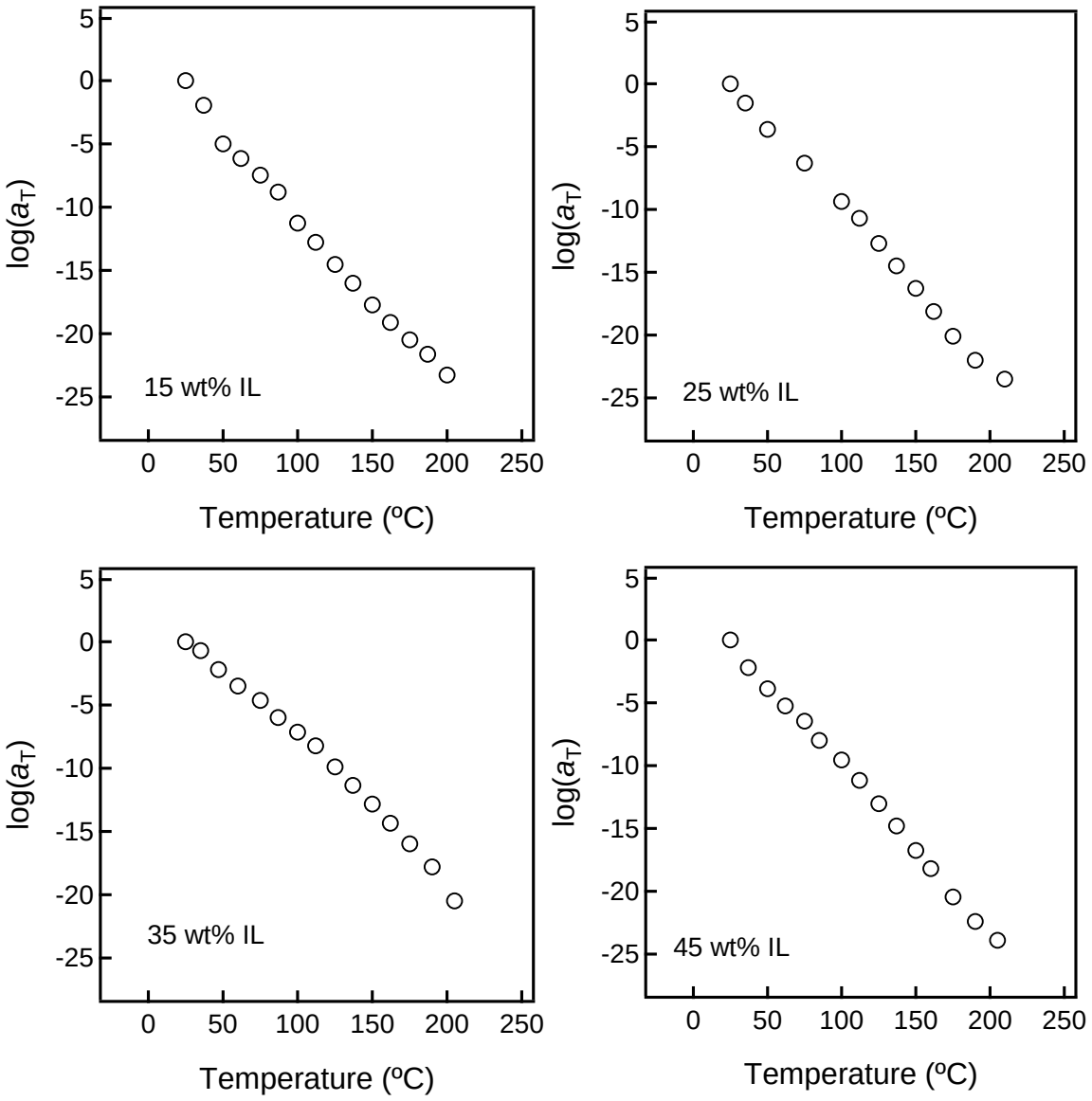

Figure 2.21: (a) Time-temperature superposition master curves for the PIMS PEM samples with varying protic IL content. The elastic (E', □) and viscous (E'', ○) moduli were measured as a function of angular frequency at the indicated temperatures. (b) Shift factors, a_T, for time-temperature superposition master curves.

Figure 2.21b shows the shift factors, a_T, used for the tTS master curves. For all samples, the shift factors exhibit an approximate linear dependence on the temperature and therefore the temperature dependence cannot be modeled by the Williams-Landel-Ferry (WLF) relationship.[167] However, it should be noted that the WLF behavior is applicable only above

T_g, where the free volume varies linearly with temperature.[167] The mechanical response was studied for the temperature range of 30–210 °C. As discussed earlier, the dense chemical cross-linking raises the T_g of the cross-linked PS block above this measurement temperature range (Figure 2.9), and therefore the non-WLF relationship is not surprising.

The thermal stability of the PEM samples was assessed using thermogravimentric analysis (TGA) under a nitrogen atmosphere. As shown in Figure 2.22, the neat cross-linked PEO-*b*-PS system has excellent thermal stability, ($T_d \approx 350$ °C), whereas PEMs are thermally stable up to approximately 270 °C. These PIMS PEMs exhibit thermal stability on a par with other high temperature fuel cell membranes such as phosphoric acid doped polybenzimidazole membranes.[17]

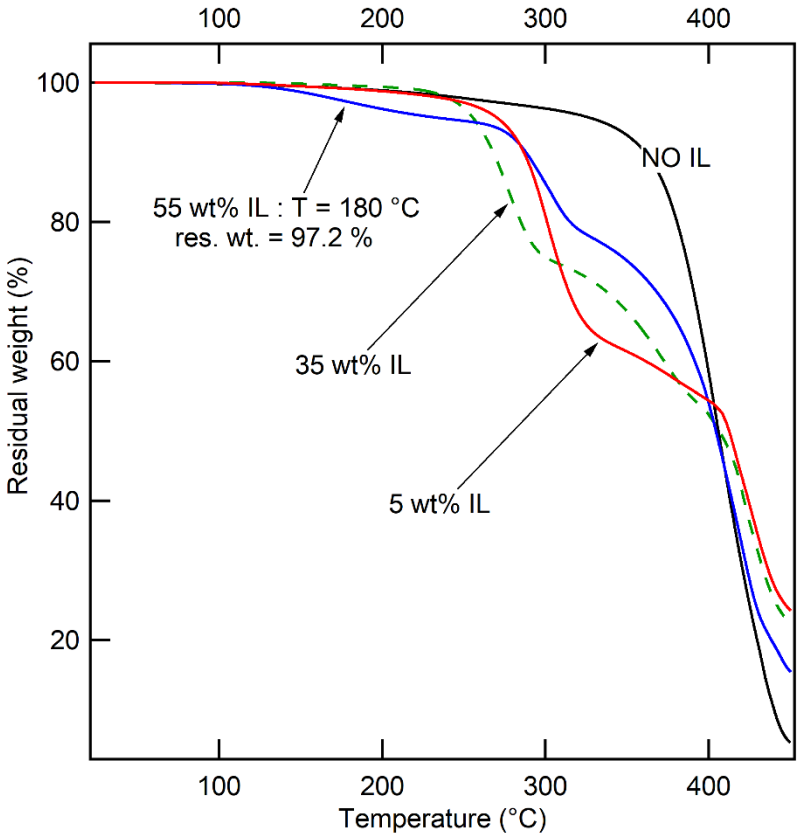

Figure 2.22: Thermogravimetric curves under nitrogen of the PIMS PEM samples with varying amount of protic IL (heating rate: 10 °C/min).

For temperatures above 300 °C, the %wt. loss in PEM samples decreases with increasing IL concentration, highlighting the superior thermal stability of the IL ($T_d \approx$ 385 °C)[23] compared to the polymer matrix. In contrast, at temperatures below the T_d of the PEMs, the thermal stability of the PEM decreases with increasing IL concentration. Similar observations were made during the impedance experiments, where high IL-content PEMs showed visible degradation when subjected to repeated heating and cooling cycles from 30 °C to 180 °C. These results can be attributed to the instability of PEO domains in presence of acidic salts like [HEIm][TFSI].[168] The weight loss in each sample is roughly consistent with the weight fraction of the PEO component in the PEM sample, and can reasonably be ascribed to the thermal degradation of PEO (see Table 2.4).

Table 2.4: Weight loss in the TGA experiments.

Sample name	TGA measurements (% wt loss at first step)	PEO content in the PEM (overall wt%)
PIMS-55	20	16
PIMS-35	25	21
PIMS-15	29	26
PIMS-5	34	31

Cross-linked, Mechanically-robust Scaffolds

Ion gels designed with ABA copolymers swollen with high IL contents exhibit excellent ionic conductivity.[113,114] However, increasing the polymer content to improve the modulus severely decreases the ionic conductivity of the system, and the lack of long-range continuity in the mechanically robust phase restricts these PEMs to moduli below 1 MPa. In contrast to ABA triblock ion gels, diblock PEMs like PS-*b*-P2VP/IL with lamellar or cylindrical morphologies are capable of exhibiting decoupled mechanical and conducting characteristics owing to the higher extent of continuity present in both the phases.[10,140] However, polymer electrolytes relying on the glassy polymer backbones experience a sudden drop in the mechanical integrity above the glass transition temperature of the glassy polymer, and even in the bulk diblock copolymers exhibit poor toughness.[5,113,169]

In the case of PIMS PEMs we overcame these limitations by designing a PEM with a co-continuous morphology and a chemically cross-linked robust insulating phase. Uniform growth of P(S-*co*-DVB) from PEO-CTA is critical to impart robustness to the system well above the glass transition temperature of linear PS ($T_g \approx 100$ °C). Long-range continuity of the cross-linked mechanical domain results in a robust, high-modulus PIMS-45 sample, even though more than half of the volume consists of the PEO/IL conducting phase. The absence of any loss of conductivity of high IL content membranes even at elevated temperatures underscores the high thermal stability of these PIMS PEMs. Consistent measurements of ionic conductivity on heating and cooling cycles further confirm the superior thermal response of the PEMs (Figure 2.23).

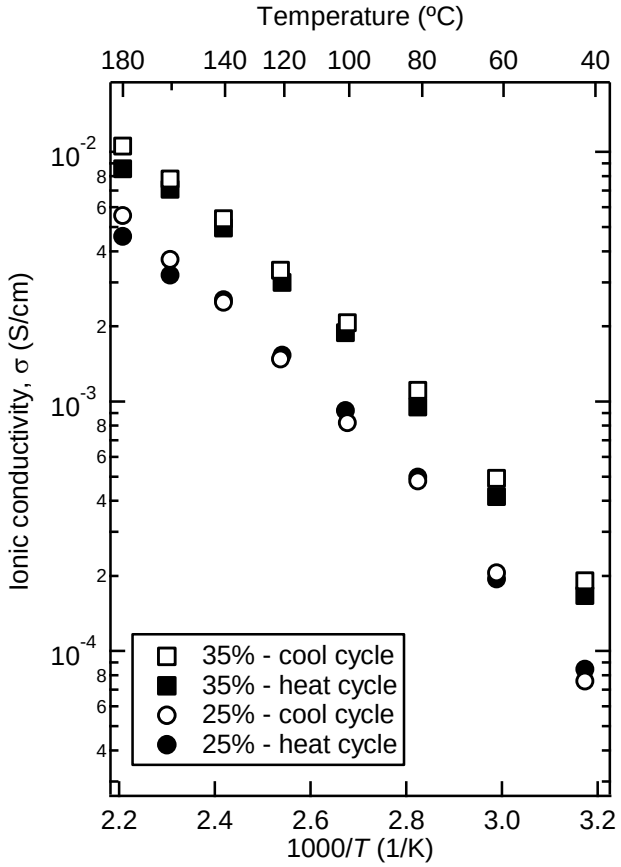

Figure 2.23: Ionic conductivity of the PIMS-25 and PIMS-35 samples during the heating and cooling cycles. Temperature varied from 40 to 180 °C.

2.4 Conclusions

Mechanically-robust and thermally stable polymer electrolyte membranes were synthesized by incorporating a protic IL into a cross-linked block polymer matrix. The simultaneous growth of the diblocks and crosslinking arrests the local segregation between the cross-linked PS phase and the conducting phase (PEO/IL), imparting a bi-continuous morphology to the nanostructured PEM. The long-range continuity of the conducting and mechanical phase allows PIMS PEMs to achieve exceptional ionic conductivity without compromising the mechanical stability of the system, even at elevated temperatures. The measured PEM conductivity as a function of IL concentration highlights the existence of isotropic continuous conducting nanochannels even at low IL content. The high selectivity of the protic IL for the PEO phase leads to increased domain purity and narrower interfaces between the PEO/IL conducting domains and the rigid cross-linked PS phase, minimizing the diffusive resistance to ionic transport.

In the absence of any proton donating groups on the polymer backbone, the proton transport mechanism in the PEMs may be described as vehicular transport of the protons associated with the cations of the IL. PIMS PEMs incorporating protic ILs are very promising for high temperature, anhydrous proton transport applications. Further study in terms of developing membrane electrode assemblies and measuring current densities and fuel crossover rates will be necessary to establish the true potential of the PIMS PEM as proton exchange membranes for high-temperature fuel cells.

Chapter 3 – Robust Polymer Electrolyte Membranes with High Ambient-Temperature Lithium Ion Conductivity*

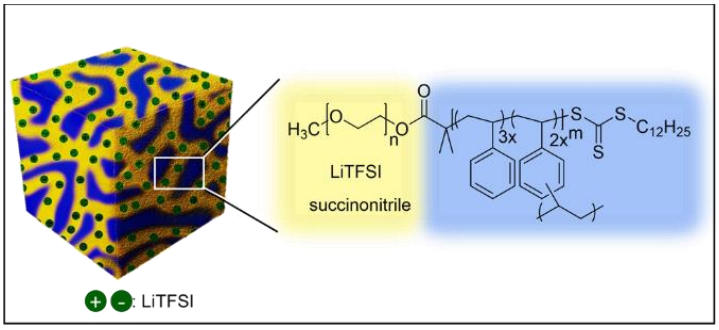

A nanostructured PEM composed of continuous conducting nanochannels intertwined with a mechanically and thermally robust crosslinked polymeric framework.

This chapter presents preparation of Li^+ conducting nanostructured PEMs via a polymerization-induced microphase separation (PIMS) strategy. Addition of succinonitrile (SN) rendered the poly(ethylene oxide)/lithium (Li) salt conducting domains completely amorphous, resulting in outstanding conductivities (~ 0.35 mS/cm) at 30 °C. Concurrently, a densely cross-linked polystyrene framework provided mechanical robustness (modulus E' ~ 0.3 GPa at 30 °C) to the hybrid material. This work highlights a facile, single-pot strategy involving a homogeneous liquid reaction precursor that yields a high-performance ion conducting membrane attractive for lithium battery applications.

3.1 Introduction

Design of robust solid-state polymer electrolyte membranes (PEMs) is a central challenge for the development of safer lithium (Li) ion batteries.[30,36] Block-polymer-based systems have been pursued as promising candidates because of their potential to simultaneously satisfy orthogonal property requirements such as high ionic conductivity and mechanical robustness.[3,12,92] Poly(ethylene oxide) (PEO) has been extensively studied as the conducting domain due to its capability to solvate a wide variety of Li salts.[41,55] In general, cation transport in PEO/Li salt systems is coupled with polymer chain segmental motion, and therefore only the amorphous PEO fraction contributes to ion conduction.[55] Consequently, PEO-based electrolytes with high degrees of crystallinity result in low ionic conductivity at ambient operating temperatures below the PEO melting point (*ca*. 65 °C for high molar mass PEO).[92] Ionic conductivity in block-polymer-based PEMs can be further compromised by network defects such as grain boundaries, dead ends and isolated domains that disrupt the connectivity of conducting pathways, and therefore such PEMs typically require post-processing steps that facilitate grain alignment to achieve appreciable conductivity.[93,170,171]

Polymer electrolytes also rely on glassy or semicrystalline polymeric sub-domains or cross-linked matrices for mechanical robustness. Newman and Monroe predicted that stiff PEMs with shear moduli $G' > 7$ GPa can suppress Li-dendrite growth, a major safety concern for systems with metallic Li anodes.[39] Hallinan et al. designed a PEM based on a diblock polymer where the glassy polystyrene (PS) domains imparted mechanical rigidity ($G' \approx 0.1$ GPa) and offered high resistance to Li dendrite growth.[40] However, due to the semi-crystallinity of the PEO/Li domain, the PEMs exhibited high conductivity (> 0.1 mS/cm) only above 90 °C.[92] Another noteworthy PEM reported by Khurana et al. consisted of semicrystalline polyethylene (PE) chains cross-linked by PEO segments that gave

membranes with high conductivity (10^{-4} S/cm) at room temperature and remarkable dendrite growth resistance, despite a low modulus ($G' \approx 0.1$ MPa) at 90 °C.[100]

Schulze et al. recently reported a single-pot strategy for mechanically robust nanostructured PEMs with bicontinuous morphology by arresting microphase separation during the growth of a diblock copolymer.[12] This polymerization-induced microphase separation (PIMS) approach involves controlled reversible addition-fragmentation chain-transfer (RAFT) polymerization of a styrene/divinylbenzene mixture from a PEO macro-chain transfer agent (PEO-CTA) in the presence of an ionic liquid. During the reaction, simultaneous growth and cross-linking of the PS domains kinetically arrests the evolving disordered network structure adopted by the growing diblock chains,[155] to produce co-continuous PEMs with locally correlated domains but no long-range order. Given its incompatibility with PS, the ionic liquid partitions exclusively to the PEO phase to form conducting nanochannels. Here, we have advanced this PIMS approach to prepare PEMs consisting of completely amorphous PEO + Li salt conducting nanochannels percolating in a cross-linked PS mechanical framework.

3.2 Experimental Section

Synthesis of PEO-CTA

Poly(ethylene glycol) methyl ether (M_n = 5 kg/mol, $Đ$ = 1.11) was purchased from Sigma Aldrich. The RAFT chain transfer agent *S*-dodecyl-*S*′-(*α*,*α*′-dimethyl-*α*″-acetic acid) trithiocarbonate (DDMAT) was synthesized as per previously reported procedures.[156] DDMAT was then coupled to the hydroxyl terminus of PEO methyl ether via an acid-intermediate to obtain the RAFT macro-CTA (Figure 3.1). Polymers were characterized by ^{1}H NMR spectroscopy and size exclusion chromatography (SEC). NMR measurements were made on a 500 MHz Bruker HD-500 spectrometer equipped with a cryoprobe. SEC measurements were carried out on a system equipped with an Agilent 1260 pump,

multiangle light-scattering detector (Wyatt Dawn DSP-F), and refractive index detector (Wyatt Optilab DSP) for absolute determination of the polymer molecular weights. Complete end-functionalization in PEO-CTA was confirmed through the controlled growth of PEO-*b*-PS linear diblocks (M_n = 30 kg/mol, $Đ$ = 1.29), indicated by shift to higher molecular weight (Figure 3.2).

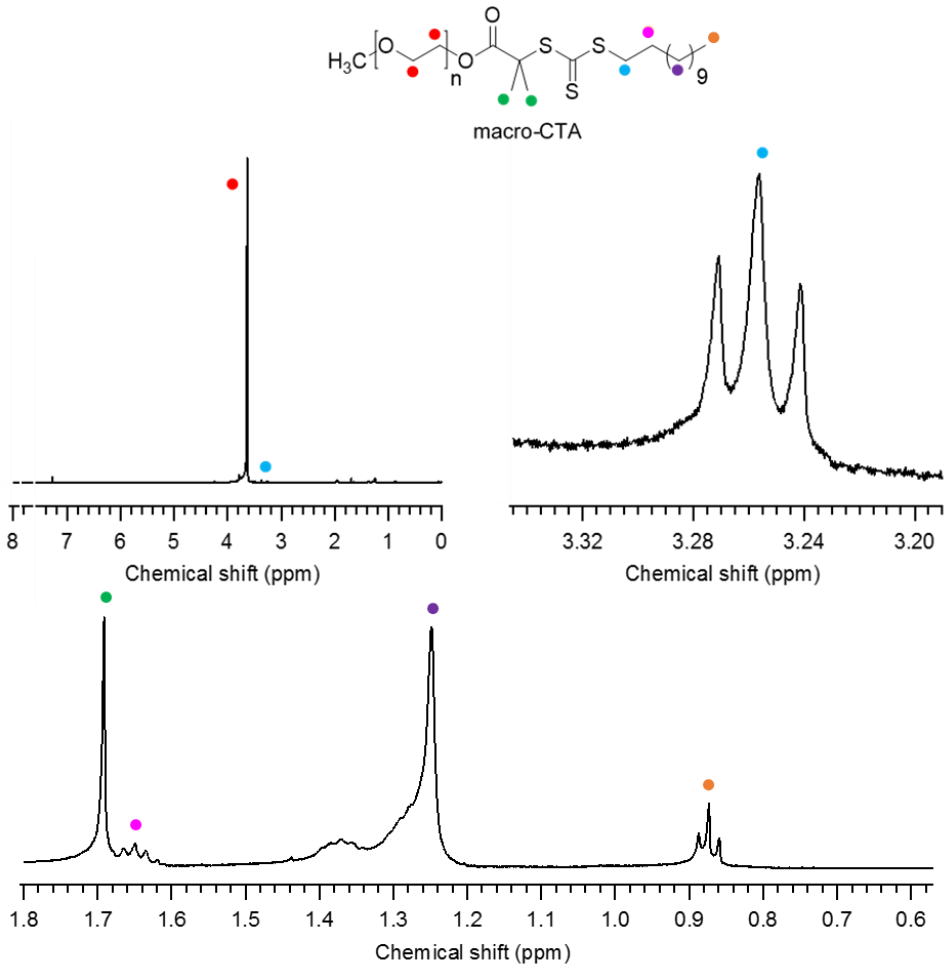

Figure 3.1: ^{1}H NMR ($CDCl_3$, 500 MHz) spectrum of PEO macro-CTA, end-functionalized with DDMAT.

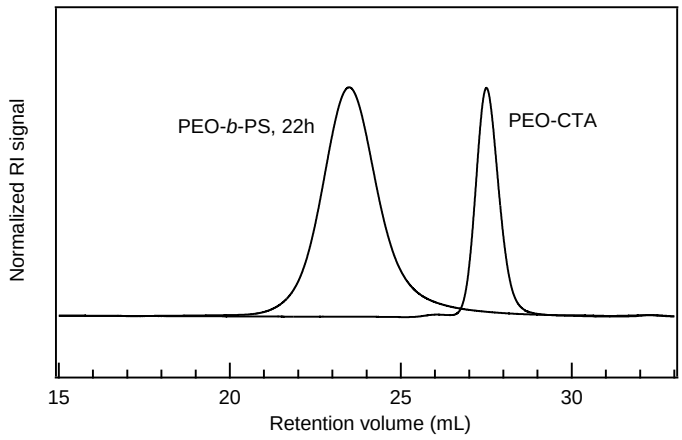

Figure 3.2: SEC chromatograms of PEO-CTA (5 kg/mol) and linear PEO-*b*-PS (30 kg/mol) diblock polymer.

Design and characterization of the PEMs

LiTFSI salt (99%) was obtained from 3M Corporation and was rigorously dried at 120 °C under vacuum for 3 days, then stored in the glove box. Succinonitrile (SN, 99%, Sigma Aldrich) was stored in the glove box and was used without further purification. Styrene (S, 99%, Sigma Aldrich) and divinylbenzene (DVB, tech. grade 80%, Sigma Aldrich) were filtered through an activated alumina column prior to storage in a glove box.

The liquid reaction precursor was prepared by combining the required amounts of PEO-CTA, LiTFSI, and SN in a glass vial with a rubber septum. The PEM samples are identified by the Li salt concentration, r = 0.05, 0.08 or 0.1, where r is the molar ratio of salt to ethylene oxide repeat units. The mixture was warmed to 70 °C and stirred to ensure uniform mixing. Next, S, DVB and benzoyl peroxide (radical initiator) were added to the glass vial through the rubber septum at the top. The mixture was further stirred and warmed at 90 °C to obtain a homogeneous mixture. The viscous reaction mixture was then cast onto a clean glass plate. Another glass plate was used to cover the bottom glass plate, separated by a thin Teflon sheet with a square-shaped cut-out (Figure 3.3a). To ensure that the glass-plate sandwich is securely sealed, vacuum grease was applied to the thin Teflon separator

beforehand and the setup was manually pressed using metal plates. The glass plate sandwich containing the reaction mixture was quickly removed from the glove box and placed in an oven pre-heated to 110 °C. Heavy metal plates were placed onto the glass plates ensuring an excellent seal.

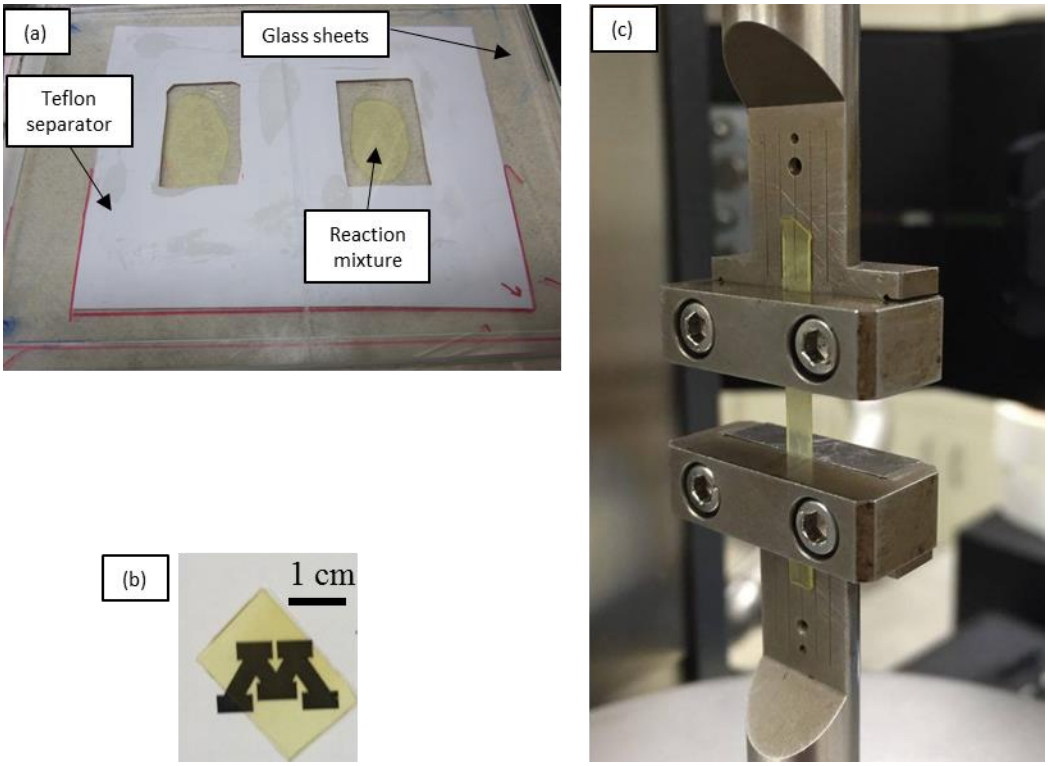

Figure 3.3: (a) Setup used to design thin PIMS PEMs. Sample thickness was determined by the Teflon separator thickness. (b) PIMS PEM-0.08 sample, thickness = 0.4 mm, and (c) PEM tensile bar loaded on RSA-G2 Solid Analyzer. The RAFT-CTA imparts the yellow color to the reaction mixture and the PIMS PEMs.

After 24 h the oven was turned off and the glass plates along with the PEM were taken to the glove box. The PEM sample was carefully removed from the glass plate and taken into the glove box-antechamber to remove any minor amount of unreacted monomer. PEM samples were stored in the glove box, and conductivity cell assembly and sample preparation for small-angle X-ray scattering (SAXS) and differential scanning calorimetry (DSC) experiments were done inside the glove box.

DSC measurements were carried out using a TA Instruments Discovery DSC. Samples were prepared using aluminum T-zero pans with hermetic lids. The samples were cooled to –90 °C, equilibrated for 10 min, then ramped up to 180 °C at the heating rate of 5 °C/min. Thermogravimetric analysis (TGA) of the PEM samples was performed on a TA Instruments Q500 under N_2 at a heating rate of 10 °C/min from room temperature to 500 °C.

Morphological Characterization

SAXS experiments were performed at beamline 5-ID-D at the Advanced Photon Source, Argonne National Laboratory. Room-temperature measurements were performed using X-rays with a wavelength (λ) of 0.76 Å yielding scattering wavevectors q ($q = 4\pi \sin(\theta/2)/\lambda$, where θ is the scattering angle) in the range of 0.022–1.35 nm^{-1}. Two-dimensional scattering data were azimuthally integrated to obtain one-dimensional intensity, I, versus q profiles. PEM samples for the SAXS experiments were sealed inside a sample holder with Kapton windows. A blank sample for background subtraction was prepared in a similar manner.

Sample preparation for scanning electron microscopy (SEM) imaging involved etching out the conducting phase (PEO + LiTFSI + SN) to achieve the necessary contrast. PEM samples were immersed in 57 wt% hydroiodic acid at 60 °C for 5 days, rinsed with methanol-water solution, then dried in an oven for 2 days. The etching conditions resulted in >95% removal of the conducting phase, as determined by gravimetric analysis. Freeze-fractured samples were coated with ~ 1 nm of platinum and imaged using a high-resolution Hitachi S-4700 FEG SEM at an accelerating voltage of 5 kV.

For transmission electron microscopy (TEM) imaging, thin sections with nominal thickness of 70 nm were obtained by cryo-microtoming at –120 °C on a Leica UC6 ultramicrotome. Sample sections were transferred to a 300 mesh copper grid and were

stained in RuO_4 vapor for 10 minutes. TEM imaging was performed on an FEI Tecnai G2 Spirit Bio-TWIN using an accelerating voltage of 120 kV.

Ionic Conductivity

Ionic conductivity of solid PEMs was measured by 2-point probe AC impedance spectroscopy using a Solartron 1255B frequency response analyzer and an SI 1287 electrochemical interface in the frequency range of $1 - 10^6$ Hz with oscillating voltage of 100 mV. A thin PEM sample (thickness ≈ 400 μm, Figure 3.3b) was sandwiched between polished platinum electrodes in a home-built sealed conducting cell (Figure 3.4a). The cell assembly was performed inside the glove box. The cell was then taken outside and inserted in a custom-built heating block (Figure 2.6c). The conductivity measurements were performed starting from 90 °C and cooling to 30 °C in 10 °C decrements, holding at each temperature for at least 1 h. Experiments were also performed while heating, by increasing temperature from 30 °C to 90 °C in steps of 10 °C. The ionic conductivity, σ, was calculated as $l/(RA)$, where l and A are the sample thickness and superficial area of the sample and R is the bulk resistance. Bulk resistance was determined from the frequency independent plateau of the real component of the impedance (Z') (Figure 3.4b). In the case of PEO + LiTFSI mixtures, a Teflon spacer was used to hold the electrolyte inside the conductivity cell. Sample preparation was done inside the glove box.

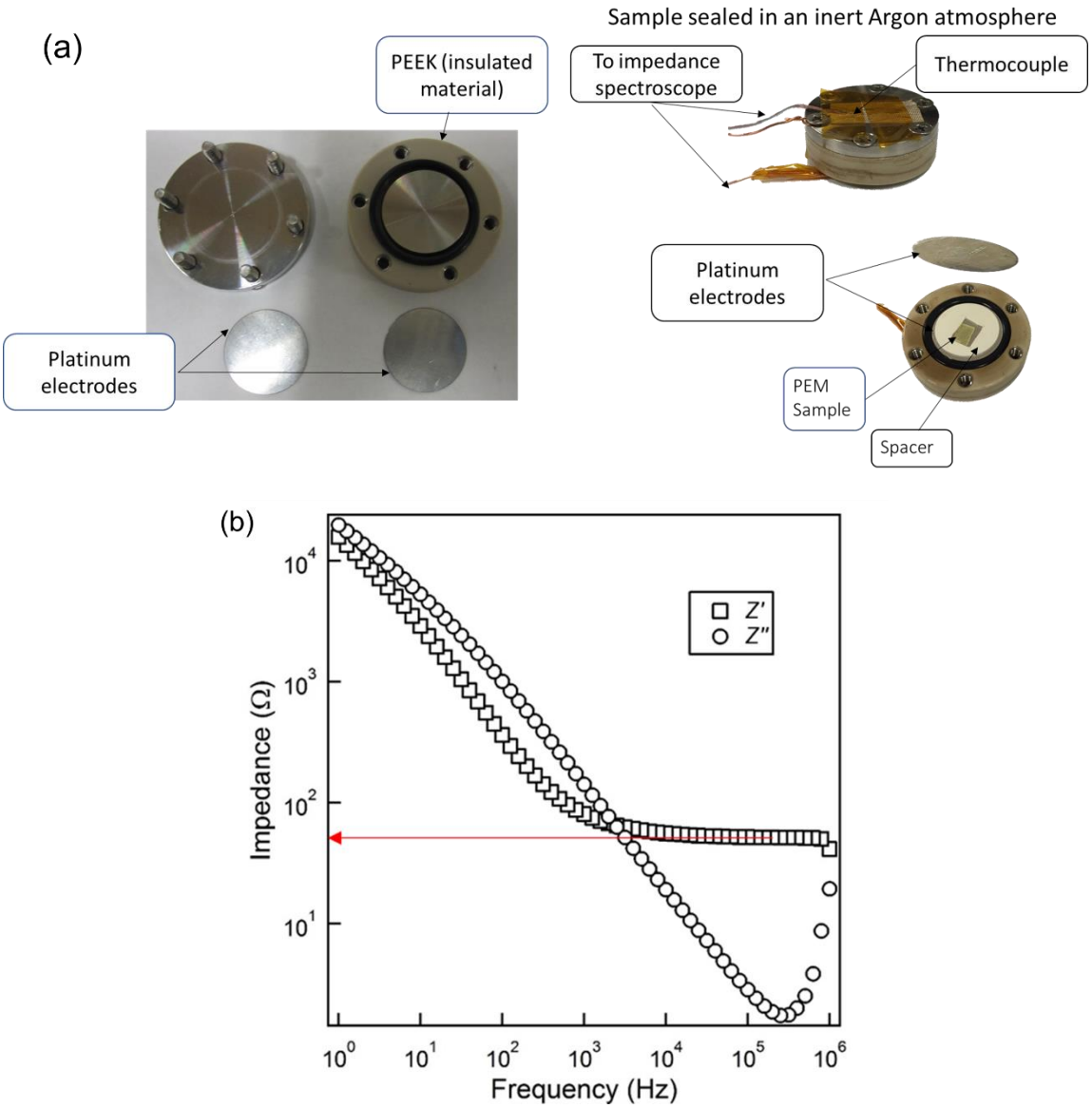

Figure 3.4: (a) Sealed conductivity cell. (b) Representative raw impedance data for a PEM-0.08 sample collected at 60 °C. Squares (□) are *Z′*, circles (○) are *Z″*. The red line denotes the bulk resistance, *R*, used to calculate the conductivity.

Diffusion Coefficient Measurements

The self-diffusion coefficients of Li^+ and $TFSI^-$ ions confined inside the PEM conducting nanochannels were measured using a Bruker Avance III 500 MHz NMR spectrometer equipped with a 5 mm Broadband Fluorine Observe (BBFO) probe. The PEM samples were ground into fine powders and loaded into the outer tube of a double tube

NMR setup; d_6-dimethyl sulfoxide filled the inner tube. For the PFG experiments, the "ledbpgp2s" pulse sequence (longitudinal eddy current delay experiment using bipolar gradients acquired in 2D) was used with two different nuclei, ^{7}Li for the cation and ^{19}F for $TFSI^-$ anion at 348 K. The translational diffusion coefficients were obtained by using eq. 3.1:

$$\frac{I}{I_0} = \exp(-\gamma^2\delta^2G^2D(\Delta - \delta/3)) \qquad (3.1)$$

where I/I_0 is the attenuated intensity at various gradient strengths (G) from 2 to 98% of the maximum G (0.47 T/m) normalized to I_0 at G = 0, and γ is the gyromagnetic ratio. γ of ^{1}Li and ^{19}F are 16.6 and 40.1 MHz/T, respectively. The diffusion time (Δ) was 100 ms, and the gradient pulse time (δ) was 2 ms for fluorine nuclei, while Δ was 700 ms and δ was 4 ms for lithium experiments.

Mechanical Response

To evaluate the mechanical properties, PEM tensile bars were designed measuring ≈ 50×10×0.4 mm^3 (Figure 3.3c). A TA Instruments RSA-G2 Solid Analyzer was used to perform strain sweeps at frequency of 10 rad/sec (1.6 Hz) to determine the linear viscoelastic regime. Frequency sweep experiments were performed at constant strain amplitude over the frequency range of 1–100 rad/s. The mechanical response was analyzed over the temperature range of 30 – 90 °C under nitrogen; the sample was equilibrated at a temperature for 10 min. Mechanical strength of the PEMs was measured from the stress-strain tests at a tensile speed of 1 mm/min.

3.3 Results and Discussion

Preparation of Polymer Electrolyte Membranes (PEMs)

The homogeneous liquid reaction precursor (Figure 3.5) consisted of styrene and divinylbenzene (S/DVB) monomers, lithium bis(trifluoromethanesulfonyl)imide (LiTFSI), a reactive PEO-CTA macro chain transfer agent, and the plasticizer succinonitrile (SN).

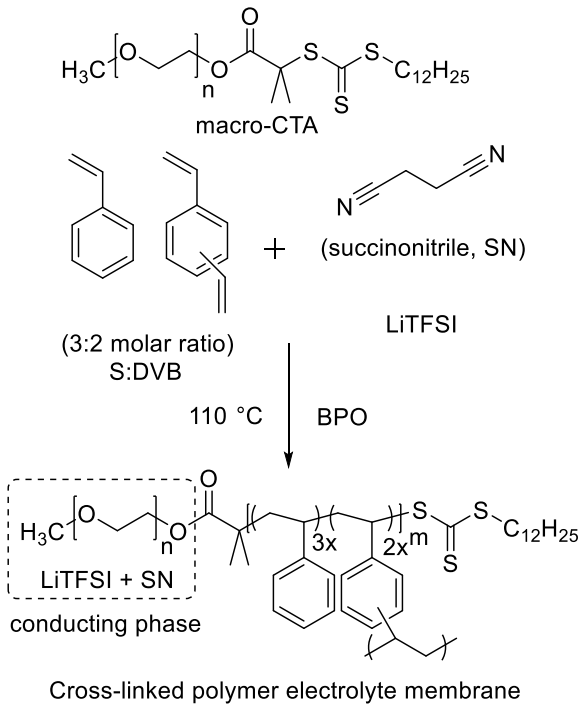

Figure 3.5: Reaction scheme used to synthesize polymerization-induced phase separation polymer electrolyte membranes.

Homogeneity of the liquid reaction precursor (*i.e.*, macro-CTA, S/DVB monomers, and Li salt) is critical for the PIMS design strategy.[12,130,172] Previous attempts to incorporate substantial LiTFSI into a PIMS PEM were severely limited by the immiscibility of PEO + salt with S/DVB monomer mixtures (Figure 3.6a). Schulze et al. added a 1 molar mixture of LiTFSI in ionic liquid to the reaction precursor, preparing PEMs with 3 volume %

LiTFSI.[12] Further increasing the salt concentration rendered the reaction mixture inhomogeneous. Also, in these PEMs the contribution of Li salt to the overall conductivity could not be quantified. Here, we improved the miscibility of the reaction components by adding the highly polar SN (dielectric constant $\varepsilon \approx 55$ at 25 °C) (Figure 3.6b), thus enabling the PIMS route to nanostructured PEMs while simultaneously enhancing Li conductivity.

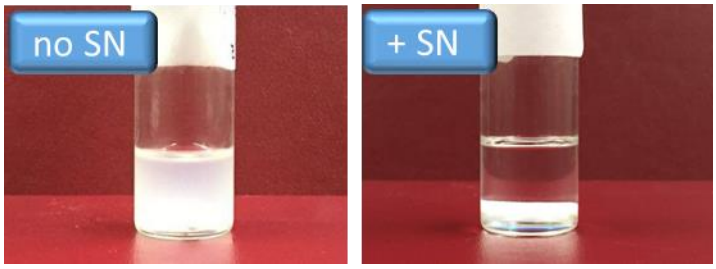

Figure 3.6: Effect of SN addition. (a) Macrophase-separated (cloudy) mixture of PEO + LiTFSI (r = 0.08) + S/DVB monomers. (b) The mixture turns optically clear (complete miscibility) upon addition of SN (z = 6). Miscibility tests were performed at 120 °C.

The PEM samples are identified by the Li salt concentration, r = 0.05, 0.08 or 0.1, where r is the molar ratio of salt to ethylene oxide repeat units (Table 3.1). The SN concentration is denoted by z, the molar ratio of SN to Li. Values of z = 5 for r = 0.05 and z = 6 for r = 0.08 or 0.1 denote the minimum amount of SN necessary to achieve miscibility of the reaction components. The lower z values were chosen so that the volume fraction of the cross-linked PS phase ≈ 0.5, ensuring mechanically robust PEMs.

Table 3.1: Composition of PEM samples

Sample name	r	z	Composition (vol %)[a]				
			PEO	LiTFSI	SN	Mech. Phase (cross-linked PS)	Cond. phase[b] (PEO+SN+Salt)
PEM-0.05	0.05	5	0.25	0.06	0.12	0.57	0.43
PEM-0.08	0.08	6	0.21	0.09	0.20	0.50	0.50
PEM-0.1	0.1	6	0.20	0.10	0.23	0.47	0.53

[a] Composition was calculated based on the following densities (g/cm^3) : ρ_{PSDVB} = 1.05, ρ_{PEO} = 1.06, ρ_{LiTFSI} = 2.02, ρ_{SN} = 0.99. [b] Volume content of the conducting phase.

Characterization of PEM Morphology

Small-angle X-ray scattering (SAXS) scattering profiles for the PEMs showed a single broad scattering peak (q^*), characteristic of nanostructured morphology with microphase-separated domains (Figure 3.7a). Given the nearly equal volume fractions of the two phases, and the absence of higher order scattering peaks, these data are consistent with other reported systems exhibiting a microphase-separated bicontinuous network morphology without long-range order.[124,130]

Further electron microscopy images and conductivity measurements confirm the bicontinuity of the morphology. The characteristic interdomain length-scale ($d = 2\pi/q^*$) is approximately 12–13 nm in these PEM samples. The domain spacing in the PIMS PEMS is determined by the molar mass of the polymer blocks, the degree of cross-linking, and the type and content of the salt/ionic liquid. With increasing *r*, the domain spacing increases slightly, consistent with increased segregation strength.[159] We note that the sensitivity of *d* on *r* in our samples is significantly less than in some PEO-containing block polymers incorporating Li salt.[92] Previous PIMS PEMs incorporating protic and aprotic ionic liquids showed only a slight increment in the *d* spacing as a function of ionic liquid content.[172] This is presumably a result of the non-equilibrium nature of the structure, as the gel point achieved during crosslinking interrupts further domain coarsening.

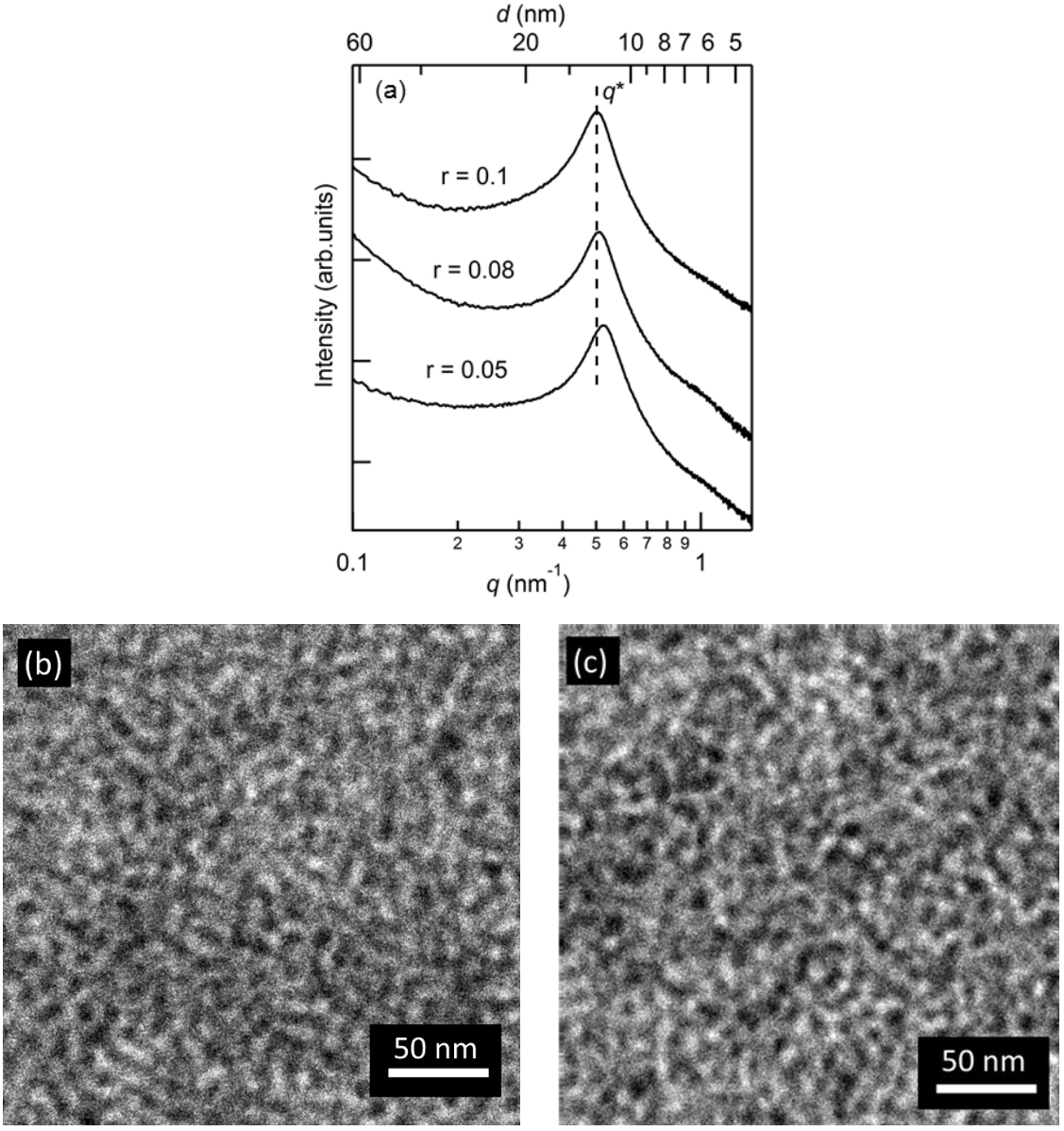
d (nm)
60
20
10 8 7 6 5
(a)
q*
r = 0.1
r = 0.08
r = 0.05
Intensity (arb.units)
0.1
2 3 4 5 6 7 8 9
1
q (nm-1)
(b)
50 nm
(c)
50 nm

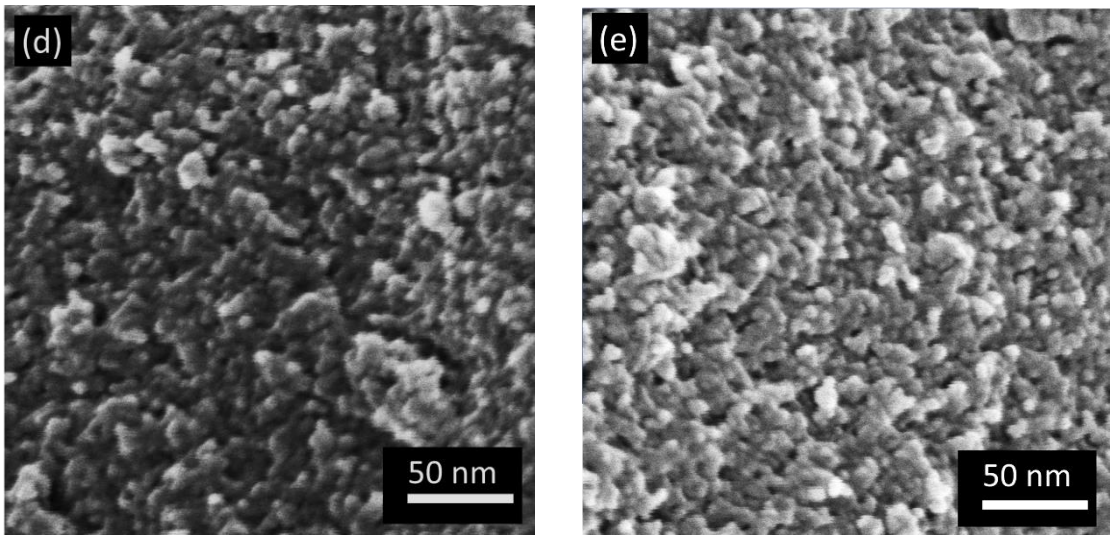

Figure 3.7: (a) SAXS for PIMS PEM samples prepared with varying Li salt content. The length scale of compositional heterogeneities increases slightly with increasing *r*. (b) TEM micrograph of PEM-0.05. The cross-linked PS domain appears dark after staining with RuO_4. (c)TEM micrograph of PEM-0.08. (d) SEM micrograph of PEM-0.05 after etching the conducting phase. The bright regions in the micrograph are the unetched PS domains. (e) SEM micrograph of PEM-0.08.

A representative transmission electron microscopy (TEM) image (Figure 3.7c) of PEM-0.08 reveals a disordered structure, corroborating the SAXS results in terms of the domain spacing. The conducting PEO + LiTFSI + SN phase appears bright in the image due to preferential RuO_4 staining of the cross-linked PS.[173] The TEM data are consistent with a percolating network structure. Treating the PEM-0.08 with 57 wt% hydroiodic acid to chemically etch the conducting phase created contrast for direct observation of the morphology by scanning electron microscopy (SEM). Figure 3.7e depicts a disordered porous structure validating the bicontinuous morphology of interpenetrating domains of conducting phase and cross-linked PS.

Ionic Conductivity

The ionic conductivity of PEMs depends on the connectivity of the nanoscale conducting channels, the ion mobility, and the concentration of dissociated ions. A major concern for PEO-based PEMS is poor room-temperature conductivity arising from high PEO crystallinity.[174] Previous attempts to suppress crystallinity include cross-linking and incorporation of plasticizers such as cyclic carbonates, ionic liquids and poly(ethylene glycol) oligomers.[12,41,175] Incorporation of succinonitrile (SN), a non-ionic molecule, in PEO-based PEMs also plasticizes the PEO and suppresses crystallinity.[61,176] In PEO + Li-salt mixtures, strong cation-oxygen complexation leads to transient physical cross-linking of the PEO segments.[92,177] It is likely that the addition of SN mitigates complexation of Li^+ cations by the PEO ether oxygen, thereby plasticizing the polymer chains. DSC experiments reveal that addition of SN lowers the T_g of PEO + LiTFSI mixture from –51 °C to –70 °C, consistent with PEO plasticization (Table 3.2, Figure 3.11). The incorporation of SN also increases the concentration of the free Li^+ cations owing to its high solvating ability, thus enhancing the ionic conductivity.[178–182]

SN is reported to be compatible with graphite and Li_xCoO_2 cathode materials. Kim et al. studied SN as an additive to ethylene carbonate (EC)-based electrolytes for lithium-ion batteries (LIBs) and observed no change in the LIB performance in terms of cyclability and capacity.[182] The authors reported that SN greatly improved the thermal stability of the LIBs as observed by increase in the onset temperature of exothermic reactions, and reduction in the amount of gas emitted upon battery failure. Strong complexation between the surface metal atoms of the Li_xCoO_2 cathode and the nitrile (-CN) of SN is considered to be reason for the improved thermal stability. Similarly, Alarco et al.[177] and Choi et al.[178] develpoed safety-reinforced electrolytes for LIBs using SN as an solvent matrix for Li salts.

Table 3.2: Thermal properties of polymer electrolyte samples.

Sample name	glass transition temperature[a] T_g (°C)	Crystallinity [b] (%)	Melting temperature[c] T_m (°C)
PEO + LiTFSI (r = 0.05)	–55	25	42
PEO + LiTFSI (r = 0.08)	–51	19	42
PEO + LiTFSI (r = 0.1)	–51	10	35
PEO + LiTFSI + SN (r = 0.05, z = 5)	–61	nd	–
PEO + LiTFSI + SN (r = 0.08, z = 6)	–70	nd	–
PEO + LiTFSI + SN (r = 0.1, z = 6)	–70	nd	–
PEM-0.05	–58	nd	–
PEM-0.08	–70	nd	–
PEM-0.1	– 71	nd	–

[a] Glass transition temperature of the conducting phase of the PEM (PEO + LiTFSI + SN)
[b] Crystallinity – nd – not detected by DSC, sample is amorphous
[c] Crystal melting temperature of the PEO/LiTFSI domains.

Figure 3.8 highlights the increase in the ionic conductivity of PEO + LiTFSI mixtures upon addition of SN. The PEO + LiTFSI mixture exhibits very low conductivity below 50 °C, consistent with crystalline PEO domains that melt at 42 °C (Table 3.2). Upon addition of SN, the conductivity of the system at 30 °C improves by a remarkable factor of 25 in the case of r = 0.08. We attribute this to a combination of complete suppression of crystallization in the electrolyte, as evident from the differential scanning calorimetry (DSC) experiments (Figure 3.11), and an increase in the free ion concentration due to increased polarity of the system.

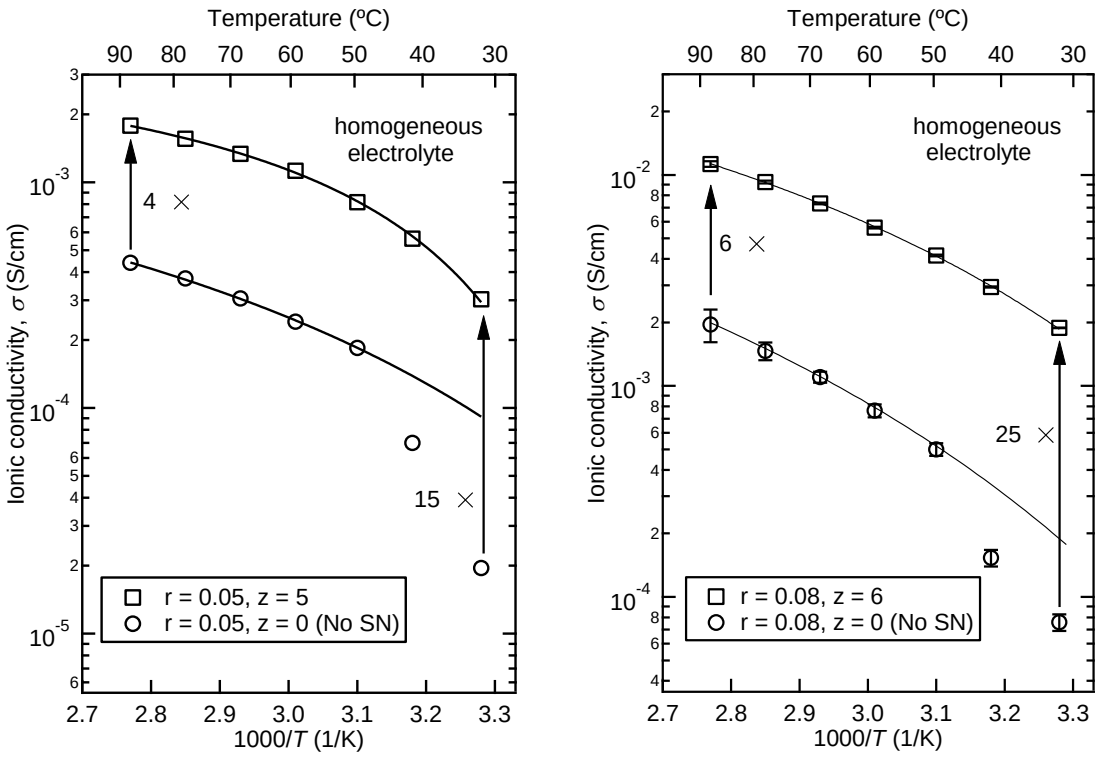

Figure 3.8: Enhancement of the ionic conductivity of PEO + LiTFSI mixtures upon incorporation of SN plasticizer. Solid lines are fits to the VFT functional form; VFT parameters are provided in Table 3.3. Error bars (in some cases smaller than the data points) are one standard deviation based on at least three measurements.

The conductivity data were fit to the Vogel–Fulcher–Tammann (VFT) equation

$$\sigma = \sigma_0 \exp\left(\frac{-B}{T - T_0}\right) \tag{3.2}$$

where the prefactor, σ_0, is proportional to the free ion concentration, B is a pseudoactivation energy term, and T_0 is the Vogel temperature. As mentioned, the addition of SN lowers the T_g of PEO + LiTFSI mixture from –51 °C to –70 °C for mixtures with r = 0.08. Faster polymer relaxation enhances the ionic mobility as reflected by the six-fold increase in conductivity (Figure 3.8b) and the larger diffusion coefficients of the ionic species in the mixtures incorporating SN as measured by PFG NMR (Figure 3.9). In comparison to mixtures with r = 0.08, a smaller amount of SN is added to the mixtures with r = 0.05 (Table 3.1). As a result, a relatively smaller drop in T_g from –55 °C to –61 °C is observed

upon addition of SN for r = 0.05 mixtures. Similarly, the conductivity of PEO + LiTFSI + SN mixture with r = 0.05 decreases with temperature at much pronounced rate owing to the higher T_g (Figure 3.8a).

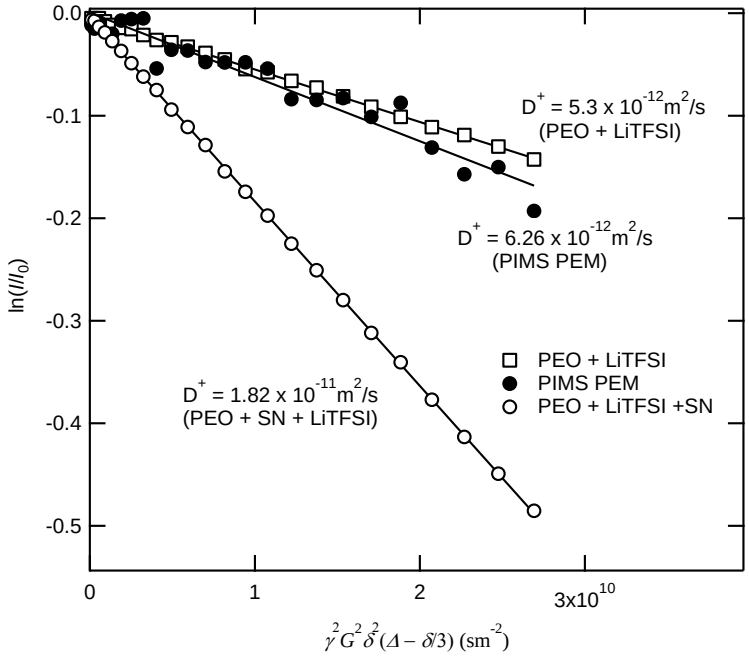

Figure 3.9: PFG NMR data and fits for the Li^+ cation at 75 °C for the three systems studied (r = 0.08, z = 6). Addition of SN facilitated the cation transport in the conducting phase.

In addition, incorporation of the highly polar SN leads to further ionization of the Li-salt increasing the free-ion concentration, as evident by the increase in the σ_0 value (Table 3.3).

Table 3.3: VFT Parameters of the conductivity profiles

r value	VFT Parameters		
	σ_0 (S/cm)	B (K)	T_0 (K)
PEO + LiTFSI + SN (r =0.08)	1.08	944	153
PEO + LiTFSI (r = 0.08)	0.35	981	172
PEM-0.1	0.25	994	152
PEM-0.08	0.22	1025	153
PEM-0.05	0.01	1175	165

The ionic conductivity of solid PEMs (Figure 3.10) increases with both temperature and *r*. PEMs with *r* = 0.08 and 0.1 exhibited conductivity in excess of 0.1 mS/cm at 30 °C, a benchmark proposed for PEMs to function in commercial batteries.[30]

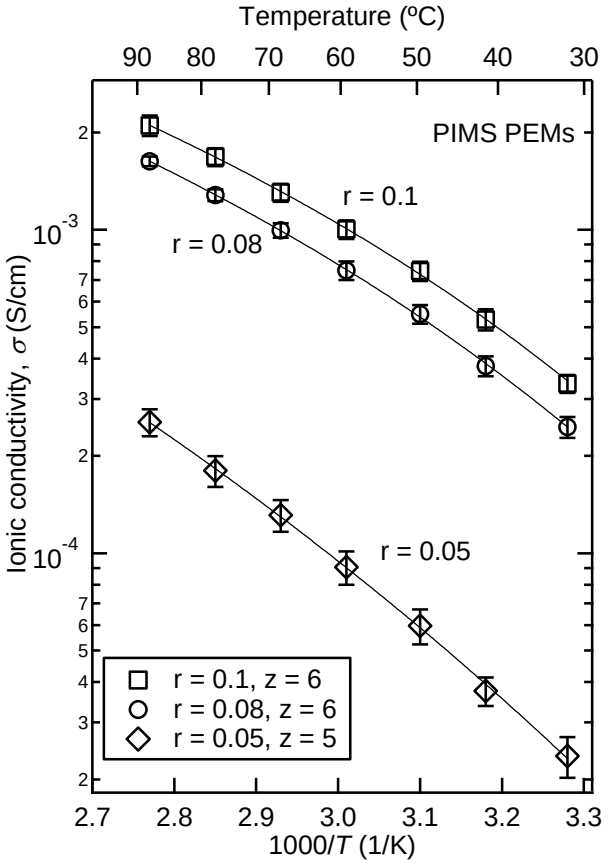

Figure 3.10: Temperature dependence of ionic conductivity of PIMS PEM samples with varying LiTFSI content. Solid lines are fits to the VFT function.

The conducting phase in all three PEMs is completely homogeneous and amorphous as indicated by DSC (Figure 3.11). The increase in PEM conductivity with increasing salt content is a cumulative effect of the increased free-ion concentration (σ_0 values, Table 3.3) due to the presence of SN, and rapid ion transport enabled by faster chain relaxation dynamics (the T_g of the conducting phase determined by DSC decreases with salt content, Figure 3.11).

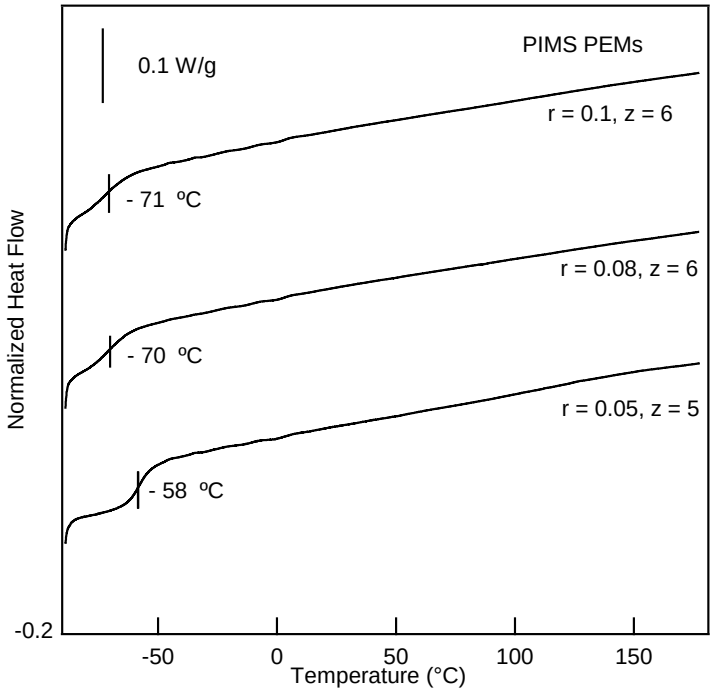

Figure 3.11: DSC thermograms for PEMs with varying salt content. The traces represent the second heating cycle (exothermic flow down). PEO crystallization is suppressed in all the sample and the glass transition temperature decreases with the salt content. A distinct glass transition is not observed for the cross-linked PS phase up to 180 °C. The lack of distinct T_g is likely a result of the high cross-link density.

The PEM ionic conductivity can also be used to gauge the extent of connectivity in the conducting nanochannels. In the absence of network defects, the σ_{PEM} can be expressed as a function of σ_h (the conductivity of the PEO + LiTFSI + SN mixture), ϕ_c (the volume fraction of the conducting phase), and τ (the tortuosity), as

$$\sigma_{PEM} = \sigma_h \frac{\phi_c}{\tau} \tag{3.3}$$

Based on previous studies of small molecule transport in media with bicontinuous morphologies, τ is expected to be between 1.5 and 3.[110,160,161] For PEM-0.08, the conductivity is slightly less than the lower limit given by the tortuosity model (Figure 3.12); the average tortuosity value inferred from eqn 3.3 is $\tau \approx 3.5$. However, eqn 3.3 assumes the PEM conducting phase to behave identically to that of a homogeneous PEO + Li salt + SN electrolyte mixture. In contrast, the PFG-NMR experimental results (Table 3.4) indicate

that the mobility of both the ionic species in the PEM is lower by a factor of 3 – 4 in comparison to the homogeneous electrolyte. Therefore, the inconsistency between the measured ionic conductivity and the predictions of the tortuosity model likely stem from the lowered flexibility of the PEO chains that are tethered to the densely cross-linked PS domains.[102] Nevertheless, the fact that σ_{PEM} approaches the tortuosity model predictions corroborates the SAXS and microscopy results (Figure 3.7).

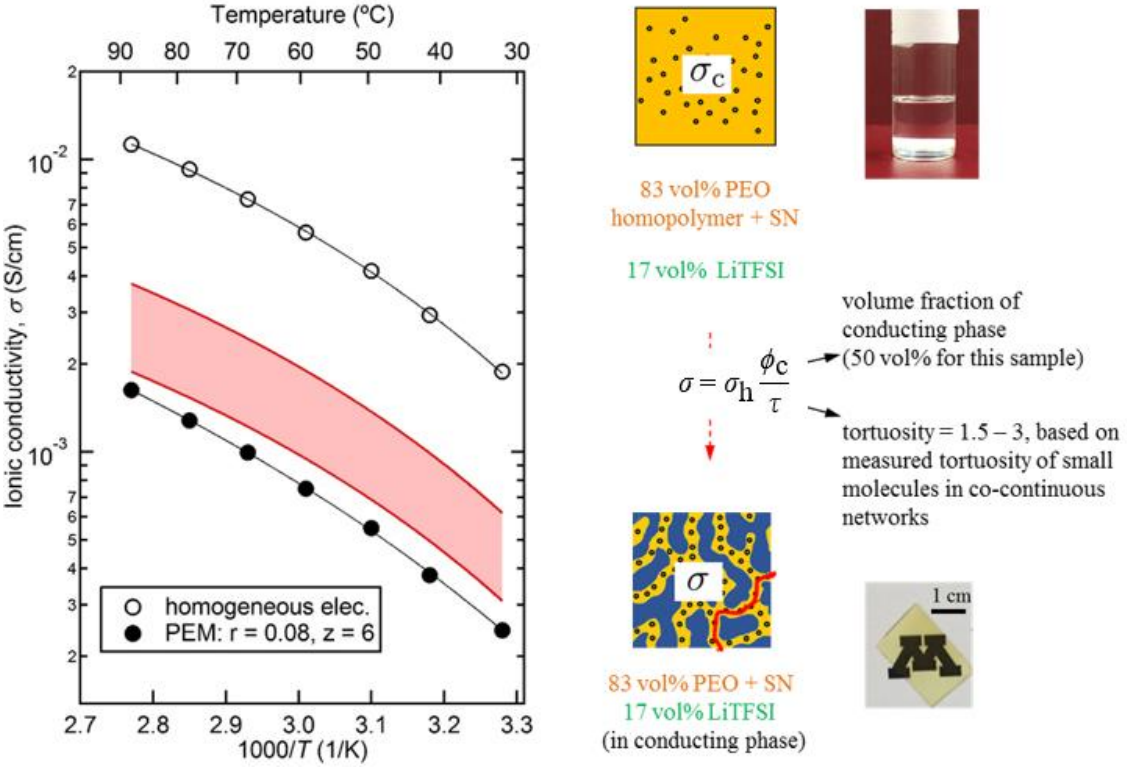

Figure 3.12: Comparison of PEM-0.08 conductivity (●) to the tortuosity model (eq. 3.3). The homogeneous electrolyte (○) was prepared with a 5 kg/mol PEO homopolymer + SN + LiTFSI mixture with the same composition as the conducting phase in PEM-0.08. The red region is defined according to eq. 3.3 with $\phi_c = 0.5$ (vol. fraction conducting phase in PEM-0.08) and $1.5 \leq \tau \leq 3$.

Lithium Transference Number

Impedance spectroscopy reflects the contributions of both Li^+ cation and the $TFSI^-$ anion to the overall ionic conductivity of the PEM sample. The Li-transference number, t^+, is the fraction of total current accounted by the transport of Li^+ cations, and is calculated as

$$t^+ = \frac{D^+}{D^+ + D^-} \tag{3.4}$$

where D^+ and D^- are the diffusion coefficients of the Li^+ cation and the $TFSI^-$ anion, respectively, measured using PFG-NMR.

The measured diffusion coefficient for both Li^+ and $TFSI^-$ increases upon addition of SN to PEO + LiTFSI, but not proportionately. SN addition allows enhanced diffusion of the free Li^+ cations. However, similar diffusion coefficient enhancement is absent in the case of Li^+ cations bound to PEO backbone. The oxygen in PEO has a higher Gutmann donor number (measure of Lewis basicity), 22, compared to the nitrile group of SN, 15.[178,183,184] The PEO chains thus act as a better "solvating medium" for the Li^+ cations.

In the case of PIMS PEM, a t^+ value of 0.17 was observed (Table 3.4). Similar observations have been made by other researchers investigating effects of addition of plasticizers on PEO + LiTFSI mixtures. Computational studies by Wu and Wick[185] and experiments by Kim and Smotkin[63] indicated that the t^+ of a PEO/LiTFSI mixture decreased from ≈ 0.48 to ≈ 0.26 upon addition of propylene carbonate.

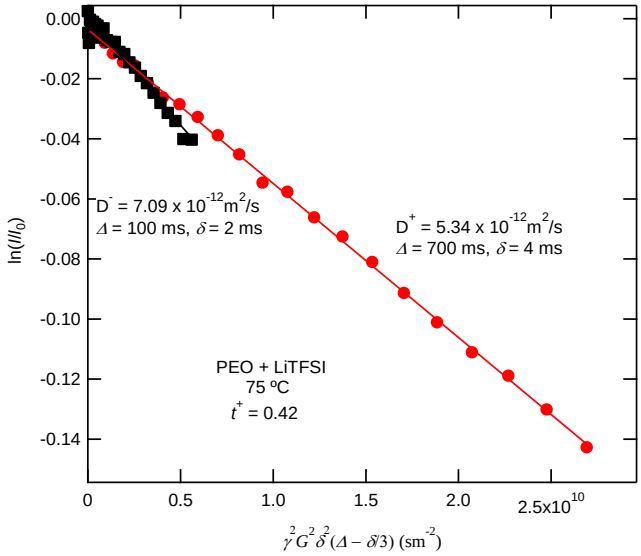

Figure 3.13: PFG-NMR data and fits for the Li^+ cation and $TFSI^-$ anion at 75 °C in PEO + LiTFSI electrolyte mixtures.

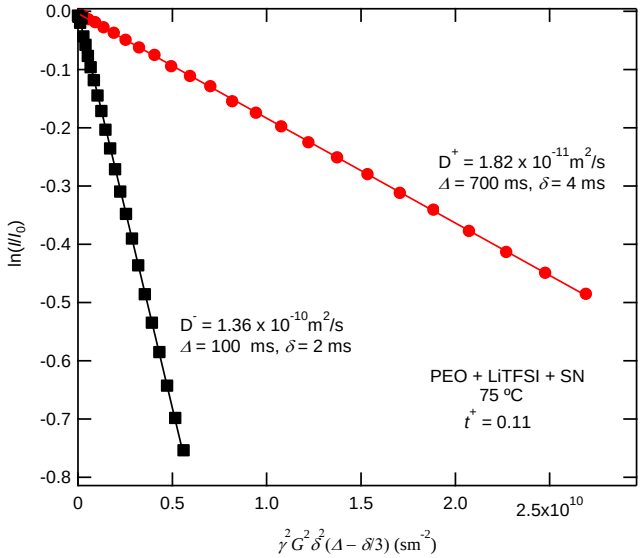

Figure 3.14: PFG-NMR data and fits for the Li^+ cation and $TFSI^-$ anion at 75 °C in PEO + LiTFSI + SN electrolyte mixtures. Addition of SN increases the ionic mobility of both the species.

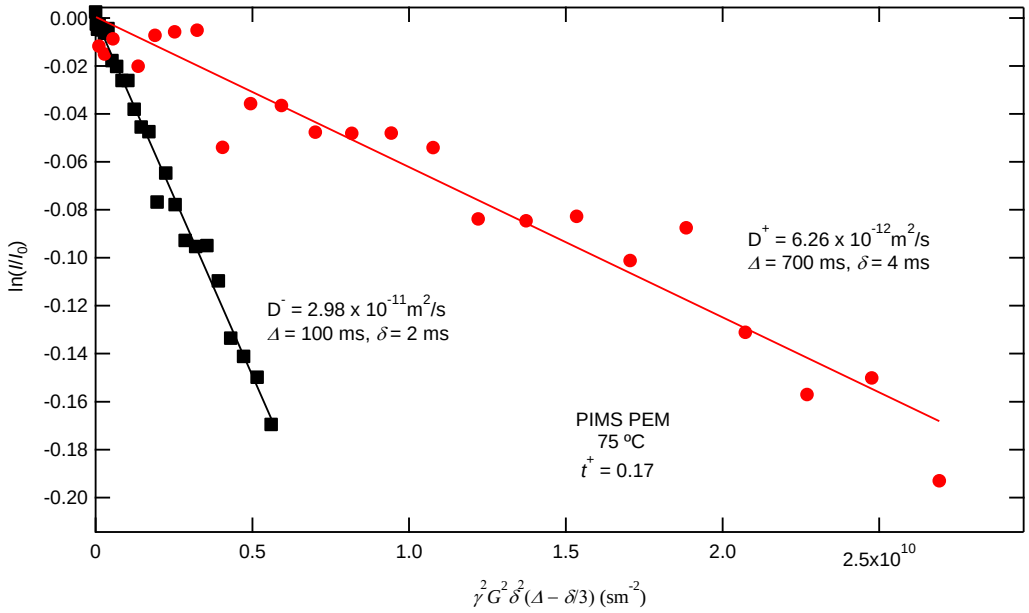

Figure 3.15: PFG-NMR data and fits for the Li^+ cation and $TFSI^-$ anion at 75 °C in the conducting phase of PIMS PEM-0.08. The relatively low concentration of the ionic species resulted in the increased noise.

Table 3.4: Li^+ cation and $TFSI^-$ anion diffusion coefficients at 75 °C

Sample name	D^+ (m^2/s) ($\times 10^{-11}$)	D^- (m^2/s) ($\times 10^{-11}$)	t^+
PEO + LiTFSI (r = 0.08)	0.53	0.7	0.42
PEO + LiTFSI + SN (r = 0.08, z = 6)	1.82	13.6	0.11
PEM-0.08	0.63	2.98	0.17

Mechanical Response and Thermal Stability

The percolating, chemically cross-linked PS scaffold endows PIMS PEMs with far superior mechanical properties in comparison to analogous block polymer systems and commercial battery separators.[34,186] PEM-0.08 exhibited a modulus $E' \approx 0.35$ GPa at 30 °C and 1.6 Hz (Figure 3.16), an ultimate tensile strength of 6 MPa, and an ultimate elongation of 3.5% (Figure 3.17). These mechanical properties are consistent with other PEMs

prepared via PIMS in the absence of SN, thus indicating that the PS phase is not significantly plasticized by SN.[12,172]

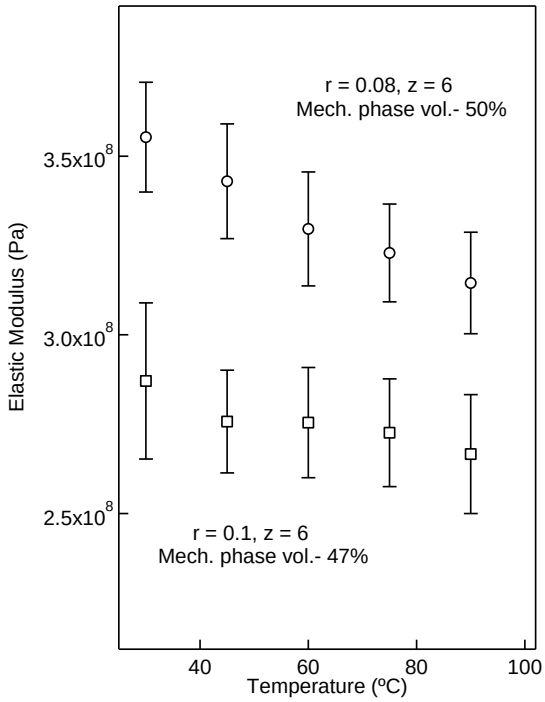

Figure 3.16: Linear elastic tensile modulus of PIMS PEMs (r = 0.08 and 0.1). Data points represent elastic modulus at 10 rad/s, and were extracted from isothermal frequency sweeps. Error bars are one standard deviation based on at least three measurements.

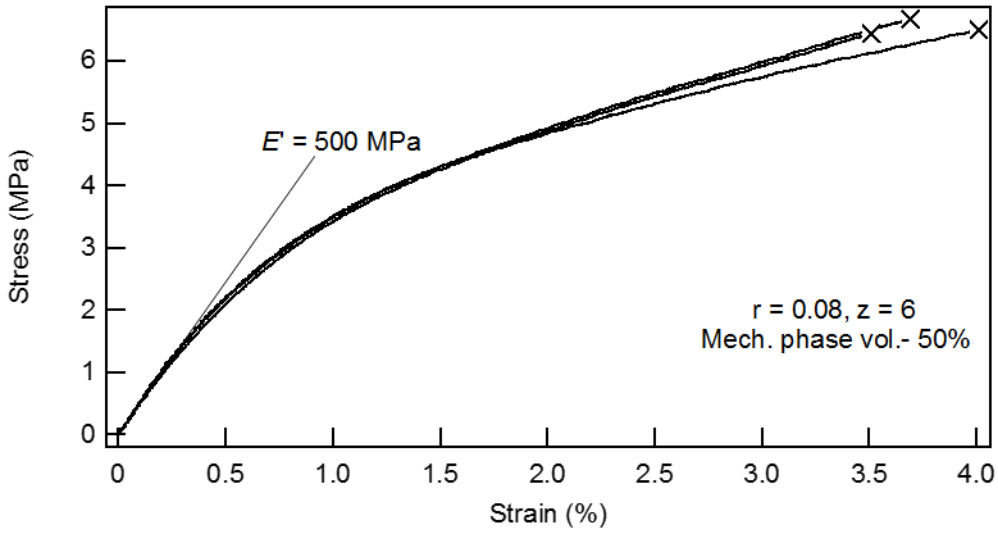

Figure 3.17: Stress-strain curve for PEM-0.08. Young's modulus was estimated from the

initial slope.

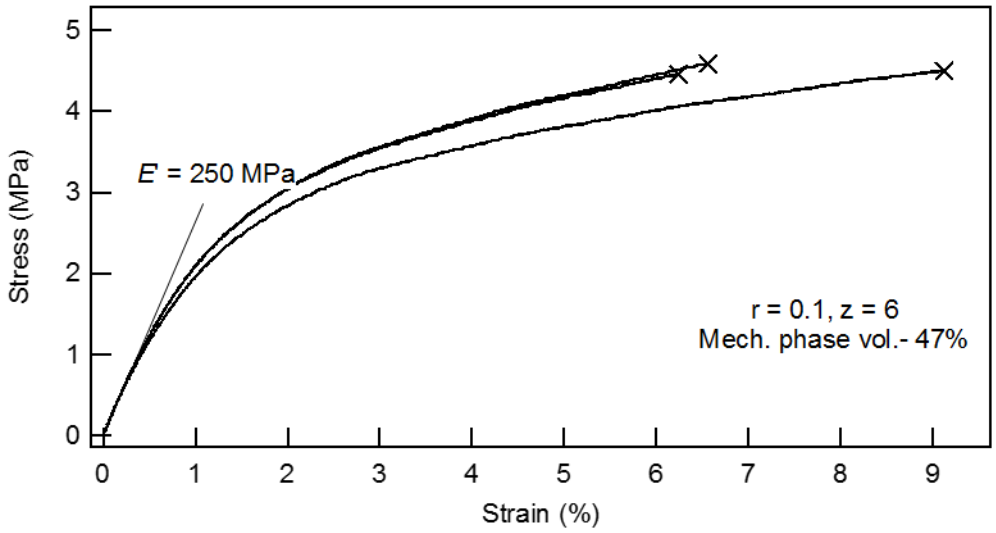

Figure 3.18: Stress-strain curve for PEM-0.1. Young's modulus was estimated from the initial slope.

Thus PIMS PEMs with tortuous nanoscale conducting channels are expected to offer appreciable resistance to growth of lithium dendrites. The mechanical robustness of the PEMs is also highlighted by consistent ionic conductivity measurements during the heating and cooling cycles (Figure 3.19).

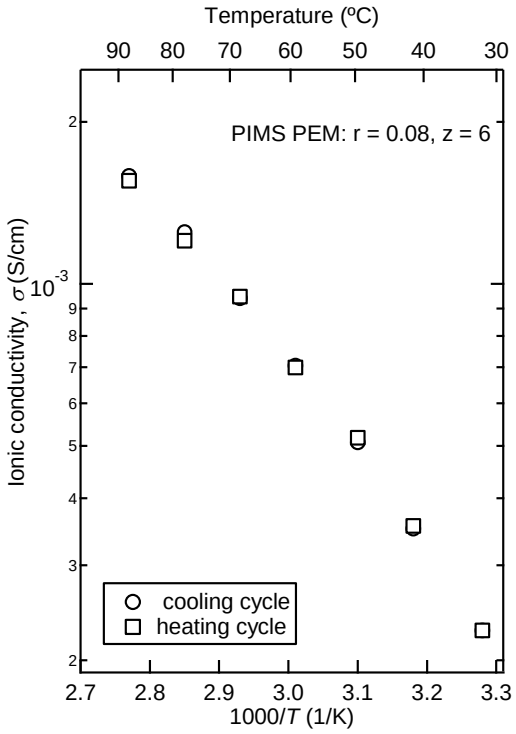

Figure 3.19: Ionic conductivity of the PEM-0.08 sample during the heating and cooling cycles. Temperature varied from 30 to 90 °C.

The thermal stability of PIMS PEMs was studied using thermogravimetric analysis under nitrogen atmosphere. Neat PIMS PEMs (without LiTFSI) exhibit excellent thermal stability up to 400 °C, whereas PEMs incorporating LiTFSI and SN retain their mass up to about 130 °C (Figure 3.20). First residual weight plateau indicates that evaporation of SN determines the thermal stability of PIMS PEMs. Neat PEO and LiTFSI are thermally stable upto 380 °C.[187] PIMS PEMs exhibit a gradual weight loss between 300 – 380 °C, losing PEO + Li salt. The cross-linked PS phases undergoes degradation around 400 °C, as observed in all the four samples.

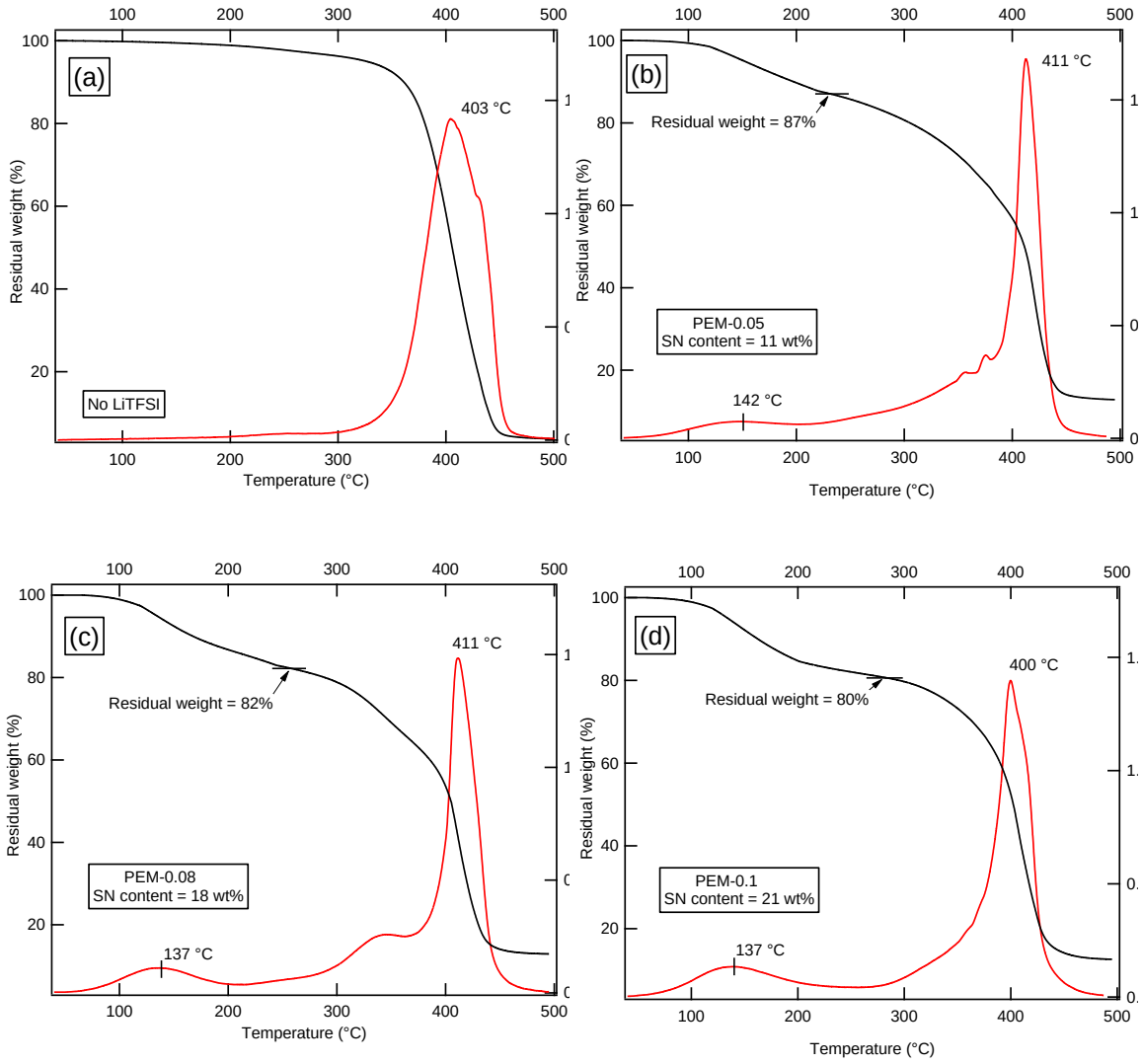

Figure 3.20: Thermogravimetric curves under nitrogen of the PIMS PEM samples with varying salt content (heating rate: 10 °C/min). (a) PEM without Li salt, (b) r = 0.05, (c) r = 0.08, and (d) r = 0.1.

3.4 Conclusions

In summary, we showcase a facile synthetic approach to design PEMs that exhibit high ionic conductivity without compromising mechanical robustness. The outstanding bulk performance was enabled by the long-range continuity of the conducting nanochannels and chemically cross-linked mechanical phase. A completely amorphous conducting phase

facilitated by SN plasticization allowed the PIMS PEMs to furnish excellent conductivity even at room temperature. Besides the high-modulus, Li-ion conducting materials discussed here, we envision the versatile PIMS synthesis strategy to be applicable to other polymer systems and applications where bicontinuous morphology and independent tunability of the mechanical and conducting phase is desirable.

Chapter 4 – Self-supporting, Hydrophobic, Ionic Liquid-Based Reference Electrodes[a,b]

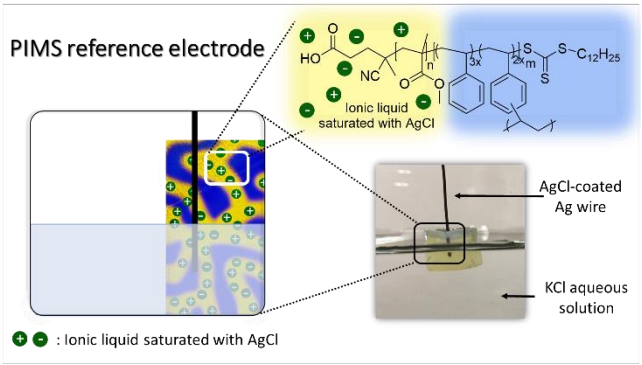

IL-based reference electrodes via polymerization-induced microphase separation (PIMS)

This chapter explores facile, single-pot synthesis of ready-to-use reference electrodes that incorporate ion conducting nanochannels filled with 1-octyl-3-methylimidazolium bis(trifluoromethylsulfonyl)imide ionic liquid, supported by a mechanically robust crosslinked polystyrene phase. The polymerization-induced microphase separation synthesis procedure allows for the straightforward design of various reference electrode geometries. These reference electrodes exhibit a low resistance as well as good reference potential stability and reproducibility when immersed into aqueous solutions, while requiring no correction for liquid junction potentials.

[a]Reproduced with permission from Chopade, S. A.; Anderson, E. L.; Schmidt, P. W.; Lodge, T. P.; Hillmyer, M. A.; Bühlmann, P. *ACS Sens.* **2017,** *2*, 1498-1504. Copyright 2017 American Chemical Society. This is an open access article published under an ACS AuthorChoice License, which permits copying and redistribution of the article or any adaptations for non-commercial purposes.
https://pubs.acs.org/doi/10.1021/acssensors.7b00512
[b]This work was conducted in collaboration with Evan L. Anderson and Phil Bühlmann.

4.1 Introduction

Ionic liquids (ILs) have attracted much attention owing to their unique combination of high ionic conductivity, non-volatility, chemical and thermal stability, and wide electrochemical windows.[48,49] This combination of properties has led to the use of ILs for numerous electrochemical applications.[5,188–191] Of particular interest is the use of hydrophobic ionic liquids to interface aqueous samples with reference electrodes.[192] So-called IL salt bridges have been studied using both neat ILs[193–196] and ILs dissolved in polymer supports.[81,197–199] IL salt bridges are characterized by stable and sample-independent electrical potentials at their interface to aqueous samples when immersed into solutions of ions that are more hydrophilic than either the IL cation or anion.

The stable potentials that develop at the interfaces of hydrophobic ILs (sparingly soluble) and aqueous solutions are established by local partitioning of IL cations and anions across the interface of the sample and the IL phase (Figure 4.1). This equilibrium has been described in the literature quantitatively, and a thorough description of the topic is available.[193] Due to the formation of stable interfacial potentials in solutions of varying ionic strength and electrolyte composition, IL-based reference electrodes provide many experimental benefits as compared to commercial KCl/porous-frit-based electrodes.[192] For example, IL-based reference electrodes have been shown to have stable potentials even in weakly buffered and low ionic strength solutions,[200] whereas porous-frit-based reference electrodes may have reference potentials that vary with the ionic strength of sample solutions and the pore size of the frit material.[201,202]

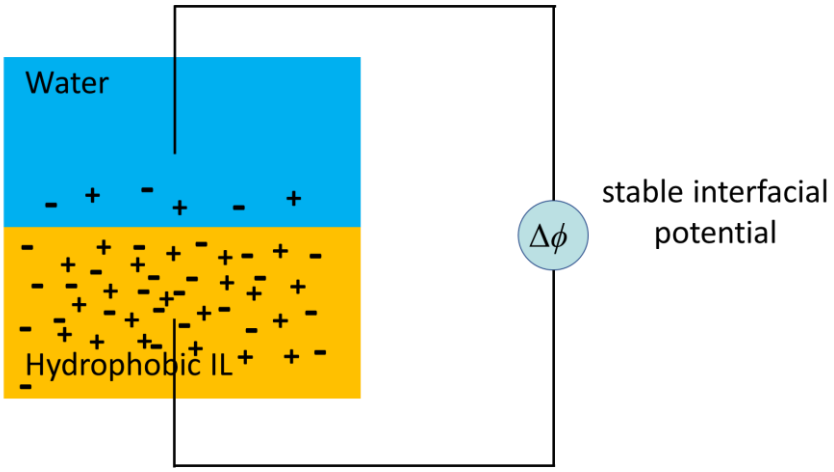

Figure 4.1: Stable potential developed at the interface of hydrophobic IL and aqueous solutions as a result of local partitioning of the IL ions across the interface.

Significant variation in potential for reference electrodes with conventional porous glass frits have been observed in solutions with low ionic strength.[201,202] These huge shifts in the potential response, more than 50 mV in some cases, have been traced back to the electrostatic screening of ion transfer through the frit due to the negatively charged surfaces of the glass nanopores (Figure 4.2).[201,202] In a high-ionic strength solution, the Debye length is smaller than the pore diameter of the glass frit, and ion transport occurs freely through the pores (Figure 4.2a). However, at low ionic strengths, if the Debye length becomes larger than the pore size, electrostatic charges impede free-transport of the electrolyte ions (Figure 4.2b).[201,202] Nevertheless, to the best of our knowledge, IL-based reference electrodes are not yet commercially available, even though their potential stability and reproducibility have been shown to be superior to commercial frit-based reference electrodes in a number of cases.[81,194,197–199,203,204] We suspect that this is due, at least in part, to the cumbersome preparation of previously reported IL-based reference electrodes.

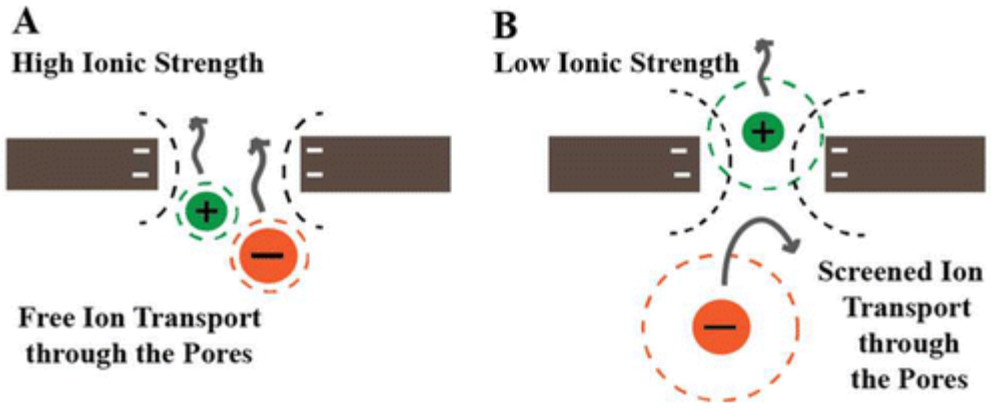

Figure 4.2: Ion transport through porous glass network. The brown rectangles represent the glass frit porous network that have developed negative electrostatic charge. The Debye length is represented by dashed lines. Screening of the ions at low ionic strength leads to huge shifts in the measured potentials. Reproduced with permission from Ref 200. Copyright 2016 American Chemical Society.

Recently, a polymerization-induced microphase separation (PIMS) strategy has been implemented to synthesize nanostructured polymers,[205] and to develop robust solid-state ion-conducting polymer composites targeted for next-generation lithium-ion batteries and fuel cells.[172,206] Nanostructured polymer/IL composites, developed by incorporating an IL into one domain of a microphase-separated and cross-linked block copolymer, exhibit high ionic conductivity and excellent thermal and mechanical robustness. PIMS is a facile, one-pot synthetic strategy that transforms a homogeneous liquid precursor consisting of monofunctional and bifunctional monomers, IL-miscible polymer macro-chain-transfer agent (macro-CTA), and IL into a solid, robust monolith with bicontinuous morphology.[155] The solvent-free feature of the PIMS strategy enables access to robust polymer/IL monoliths of any desired shape and form. The easy-to-process liquid reaction precursor (viscosity ca. 25 cP at room temperature) undergoes polymerization and simultaneous in-situ cross-linking, thereby solidifying to adopt the shape of the reaction container.

Here, we use the PIMS design strategy to develop polymer/IL-composite reference electrodes by incorporating hydrophobic ILs such as 1-octyl-3-methylimidazolium

bis(trifluoromethyl sulfonyl)imide, [C_8mim][Ntf_2], and 1-dodecyl-3-methylimidazolium bis(trifluoromethyl sulfonyl)imide, [C_{12}mim][Ntf_2], into an IL-miscible poly(methyl methacrylate) (PMMA) domain. In this chapter, [C_8mim][Ntf_2] and [C_{12}mim][Ntf_2] are referred to as C_8-IL and C_{12}-IL, respectively. The PMMA/IL phase allows for ion transport in the nanostructured junction between the sample and the inner reference Ag/AgCl electrode (Figure 4.3) and controls the phase boundary potential at the interface to the aqueous sample, whereas styrene and divinylbenzene are used as the monofunctional and difunctional monomers to develop the IL-immiscible, cross-linked mechanical framework. This facile design strategy, in addition to the combination of excellent electrochemical response and mechanical robustness, makes the PIMS polymer/IL composites promising candidates for miniaturized solid-state reference electrodes and measurements in solutions of low and moderate ionic strength.

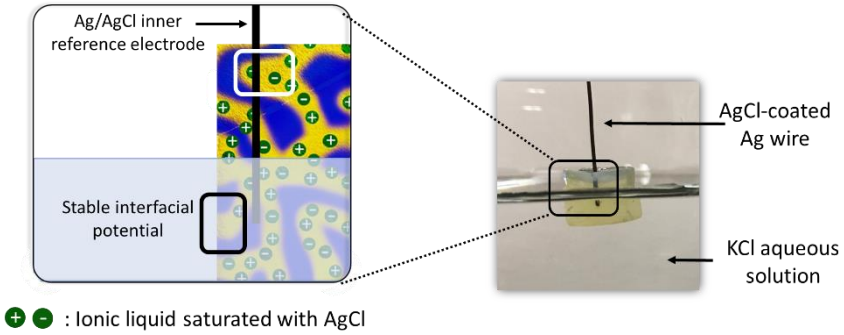

Figure 4.3: PIMS reference electrode used in a KCl aqueous solution. The AgCl coated silver wire plays role of inner reference electrode. The PMMA/IL ionic nanochannels act as a junction between the KCl aqueous solution and Ag/AgCl reference electrode.

4.2 Experimental Section

Materials

Styrene (S, 99%), divinylbenzene (DVB, tech. grade 80%), methyl methacrylate (MMA, 99%), benzoyl peroxide (BPO), 4,4´-azobis(4-cyanovaleric acid) (ACVA), 4-cyano-4-[(dodecylsulfanylthiocarbonyl)sulfanyl]pentanoic acid (CDTPA), silver chloride

(AgCl, 98%), and poly(vinylidene fluoride-*co*-hexafluoropropylene) (P(VdF-*co*-HFP), average molar mass 400 kg/mol) were purchased from Sigma-Aldrich. Other chemicals were of reagent grade. The ionic liquids [C_8mim][Ntf_2], and [C_{12}mim][Ntf_2] were purchased from Ionic Liquid Technologies (Tuscaloosa, AL). Ag wires (0.5 mm diameter, ≥ 99.9 %) were purchased from Alfa Aesar.

PMMA-CTA synthesis

PMMA-CTA was synthesized from the commercially available reversible addition-fragmentation chain-transfer (RAFT) chain transfer agent CDTPA (Figure 4.4). MMA (30 g, 0.3 mol, filtered through activated neutral alumina to remove inhibitor), CDTPA (150 mg, 0.37 mmol), and ACVA (10.4 mg, 0.04 mmol) were dissolved in 85 g dioxane in a Schlenk flask. The reaction mixture was degassed in three freeze-pump-thaw cycles and placed in an oil bath at 80 °C. After 12 h, the reaction flask was removed from the heat and the reaction stopped by cooling in an ice bath and opening the flask to the atmosphere. The polymer was then precipitated twice from hexanes and collected via filtration, yielding the PMMA macro-CTA as a yellowish powder. Polymers were characterized by ^{1}H NMR spectroscopy and size exclusion chromatography (SEC). NMR measurements were made on a 500 MHz Bruker HD-500 spectrometer equipped with a cryoprobe. SEC measurements were carried out on a system equipped with an Agilent 1260 pump, multiangle light-scattering detector (Wyatt Dawn DSP-F), and refractive index detector (Wyatt Optilab DSP) for absolute determination of the polymer molecular weights. SEC results: M_n = 40 kg/mol, $Đ$ = 1.08 (Figure 4.6).

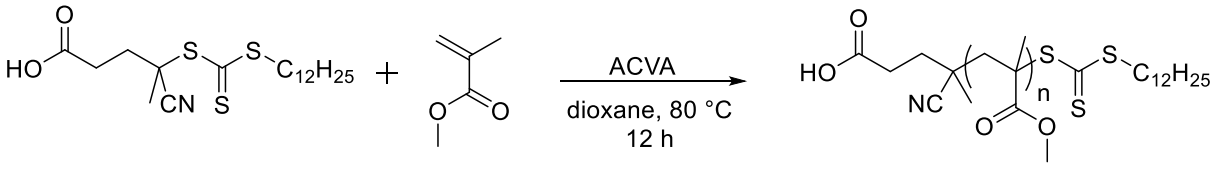

Figure 4.4: Synthesis of macro-chain transfer agent PMMA-CTA.

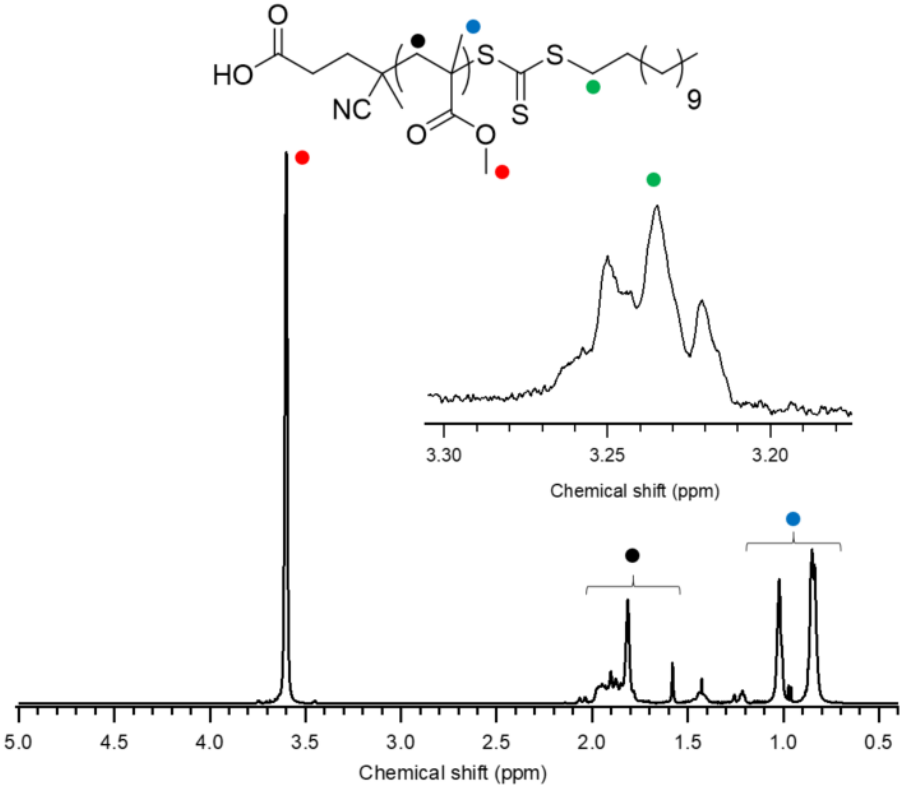

Figure 4.5: ^{1}H NMR ($CDCl_3$, 500 MHz Bruker HD-500 spectrometer) spectrum of PMMA-CTA.

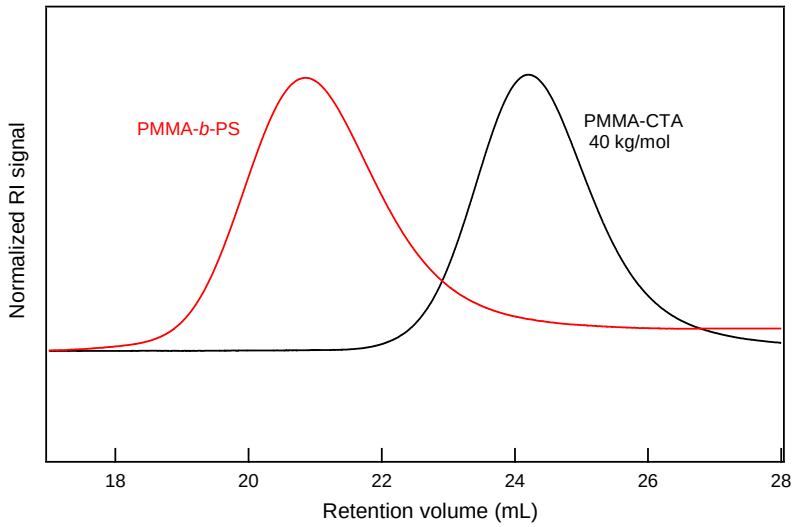

Figure 4.6: SEC chromatograms of PMMA-CTA (40 kg/mol, $Đ$ = 1.08) and linear PMMA-*b*-PS ($Đ$ = 1.2) diblock polymer. End-functionalization in PMMA-CTA was

confirmed through the controlled growth of PMMA-*b*-PS linear diblocks, as indicated by the shift to higher molecular weight.

Preparation of AgCl-coated Ag wires

Ag wires (0.5 mm diameter) were cleaned with 3 M nitric acid for 30 s and rinsed using deionized, purified water. The cleaned Ag wires were placed in a 0.1 M HCl solution with a Ag/AgCl porous frit reference electrode and a Pt mesh counter electrode. A current of 0.4 mA/cm^2 was applied for 45 min. The AgCl-coated wires were cleaned with deionized water and allowed to age for at least 24 h in air. AgCl-coated Ag wires were then directly used for the preparation of PIMS reference electrodes.

Preparation and characterization of PIMS reference electrode material

To develop PIMS reference electrodes, a liquid reaction precursor was prepared containing 12.5% w/w PMMA-CTA, a 3:2 molar mixture of styrene to divinylbenzene (37.5% w/w), AgCl-saturated IL (50% w/w) and BPO (a radical initiator, 0.05 eq. with respect to PMMA-CTA); see Figure 4.7.

Table 4.1: Composition of PIMS reference electrodes

	Composition (% w/w)			Composition (% v/v)*		
	Mechanically robust phase (cross-linked PS)	Ionic liquid	Conducting phase (PMMA + IL)	Mechanically robust phase (cross-linked PS)	Ionic liquid	Conducting phase (PMMA + IL)
PIMS/C_8-IL (40% IL content)	45	40	55	50	35	50
PIMS/C_8-IL (50% IL content)	37.5	50	62.5	41	46	59

*Composition was calculated based on the following densities (g/cm^3): ρ_{PSDVB} = 1.05, ρ_{PMMA} = 1.18, $\rho_{C8\text{-}IL}$ = 1.32. Except for the SAXS experiments, the composition of PIMS reference electrodes was 50 wt% IL content.

Prior to the mixture preparation, styrene and divinylbenzene were filtered through activated alumina, and the ionic liquids were saturated with AgCl by stirring an IL + AgCl

mixture at 50 °C for 24 h. The reaction mixture was warmed to 40 °C and stirred for 30 min to ensure uniform mixing. About 0.75 mL of the homogeneous reaction mixture was then transferred to a 1.5 mL glass vial, which was subsequently crimp-sealed using an aluminum cap prefitted with a rubber septum.

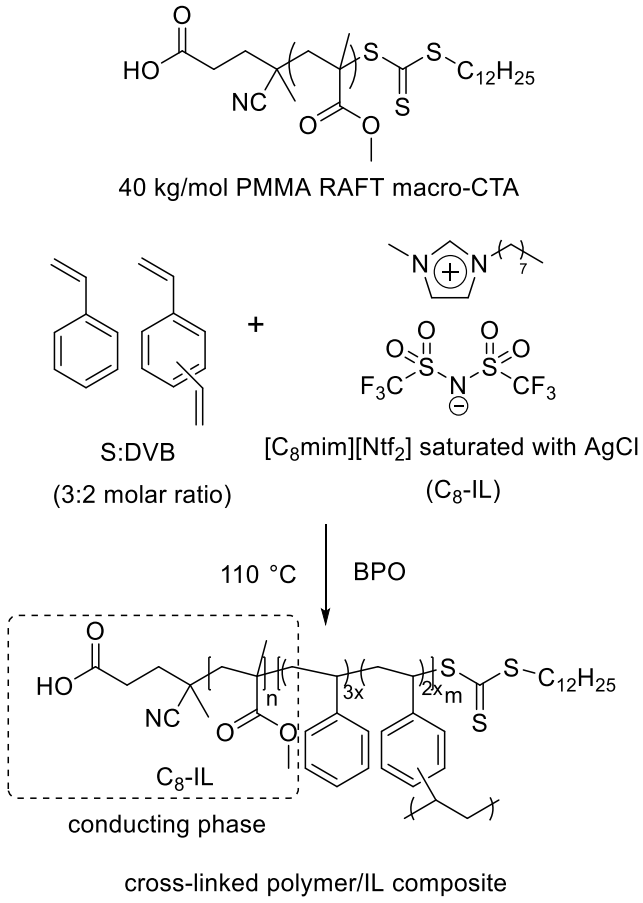

Figure 4.7: Reaction scheme used to synthesize polymerization-induced microphase separation reference electrodes.

A AgCl-coated Ag wire was inserted through the rubber septum and suspended in the reaction mixture (Figure 4.8a). The glass vial was then immersed in a sand bath maintained at 110 °C for 24 h. The resulting solid PIMS reference electrode was removed from its mold by breaking the glass vial (Figure 4.8b). Subsequently, the samples were dried at room temperature under reduced pressure for 24 h to remove any minor amounts of

unreacted monomer. The reference electrodes were directly used for electrochemical measurements.

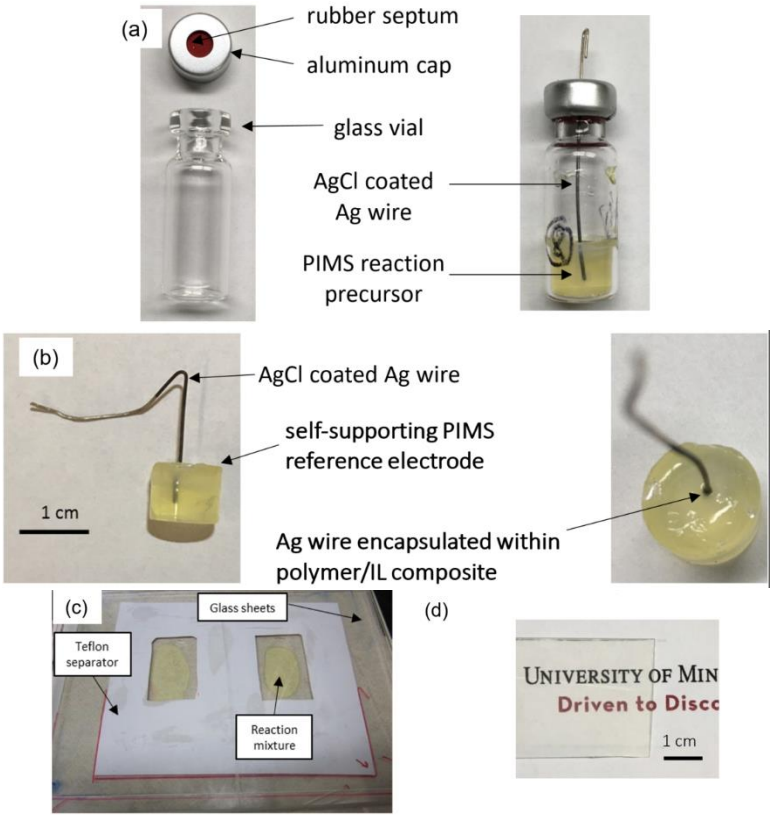

Figure 4.8: (a) Sealed vials used to prepare PIMS reference electrodes. A AgCl-coated Ag wire was inserted through the rubber septum and suspended in the reaction mixture. (b) Self-supporting PIMS reference electrode obtained by breaking the glass vial. The Ag wire is firmly encapsulated within the PIMS polymer/IL composite. (c) Setup used to design thin PIMS samples for mechanical testing. Sample thickness was determined by the Teflon separator thickness. (d) PIMS/C_8-IL sample, thickness = 0.4 mm, was used to design rectangular tensile bars for mechanical testing. The RAFT-CTA imparts the yellow color to the reaction mixture and the PIMS reference electrodes.

To study the mechanical properties of the PIMS/C_8-IL material, rectangular tensile bars measuring ≈ 50×10×0.4 mm^3 were prepared. A thin sheet (thickness ≈ 0.4 mm) of the PIMS/C_8-IL material was prepared by casting the reaction mixture onto a glass plate. Another glass plate covered the bottom glass plate, separated by a thin Teflon sheet mask with a square cut-out (Figure 4.8c). The glass plate/mask sandwich was sealed using vacuum grease applied to the Teflon mask, and the assembly placed in an oven at 110 °C

for 24 h. Subsequently, the sample was carefully removed from the glass plates and dried at room temperature under reduced pressure.

The mechanical strength of the samples was measured by stress-strain tests at a tensile speed of 1 mm/min using a TA Instruments RSA-G2 Solid Analyzer. Differential scanning calorimetry (DSC) measurements were performed on samples prepared with aluminum T-zero pans and hermetic lids using a TA Instruments Discovery DSC. The samples were cooled to –90 °C, equilibrated for 10 min, and then ramped up to 180 °C at the heating rate of 10 °C/min. Thermogravimetric analysis (TGA) of the samples was performed using a TA Instruments Q500 under a nitrogen atmosphere at a heating rate of 10 °C/min from room temperature to 500 °C.

Morphological Characterization

SAXS experiments were performed on the PIMS/C_8-IL samples with beamline 5-ID-D at the Advanced Photon Source, Argonne National Laboratory, using X-rays with a wavelength (λ) of 0.76 Å, yielding scattering wavevectors q in the range of 0.022–1.35 nm^{-1} ($q = 4\pi \sin(\theta/2)/\lambda$, where θ is the scattering angle). One-dimensional intensity, I, versus q profiles were obtained by azimuthally integrating isotropic, two-dimensional scattering data.

The nanostructured morphology of PIMS/C_8-IL sample was imaged by TEM. Thin sections with a nominal thickness of 70 nm were obtained by cryomicrotoming at –80 °C on a Leica UC6 ultramicrotome and transferred onto a 300 mesh copper grid. TEM imaging was performed without staining on a FEI Tecnai G2 Spirit Bio-TWIN using an accelerating voltage of 120 kV.

Preparation of P(VdF-*co*-HFP)/C_8-IL gel reference electrodes

For comparison, reference electrodes were also prepared following the procedure previously described by Kakiuchi and co-workers.[81] P(VdF-*co*-HFP), AgCl-saturated IL,

and acetone were mixed 1:1:5 by weight, and a AgCl-coated Ag wire was briefly dipped into this polymer/IL solution. The newly coated wire was then air-dried for 15 min before re-immersing it into the solution. This procedure was repeated until a layer of ≈ 2 mm thick polymer/IL gel was deposited onto the wire, followed by drying of the reference electrode under reduced pressure prior to potentiometric measurements. To compensate for poor gel coverage at the bottom tip of the wire, commercial silicone sealant was used to insulate the tip (Figure 4.9).

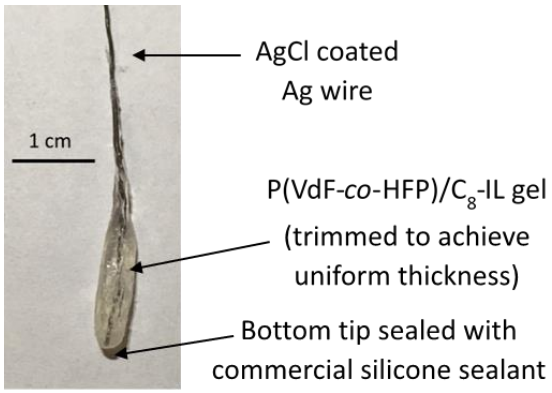

Figure 4.9: P(VdF-*co*-HFP)/C_8-IL gel reference electrodes were prepared by sequential gel deposition onto a Ag wire. The gel deposit was trimmed using a razor blade to achieve a uniform thickness. To compensate for the poor gel coverage at the bottom tip of the wire, commercial silicone sealant was used to insulate the tip.

Potentiometric measurements

Potential measurements were performed using a Lawson Labs EMF 16 channel potentiometer (Malvern, PA) controlled by EMF Suite 1.02 software. All measurements were performed in stirred solutions at room temperature (23 ± 2 °C). KCl solutions were prepared by standard addition to deionized, purified water (18.2 MΩ cm specific resistance, EMD Millipore, Philadelphia, PA) from 0.030, 0.30, and 3.0 M KCl stock solutions. Samples were not exposed to ILs before electrochemical measurements, and EMF measurements were started 5–10 minutes after the electrodes were exposed to aqueous solutions. Potentials were measured relative to a conventional Mettler Toledo DX200 free-flowing double junction reference electrode (with a 1.0 M LiOAc bridge electrolyte and

AgCl saturated 3.0 M KCl inner reference electrolyte).[207] No changes in reference potentials were noted when the contact area of the PIMS reference electrodes with aqueous solutions was varied. Activity coefficients were calculated using a two-parameter Debye-Hückel approximation,[208] and all electromotive force (EMF) values were corrected for liquid junction potentials using the Henderson equation.

Cl^- calibrations were performed using a AgCl-coated Ag wire (prepared as described above), inserted into solutions of the appropriate Cl^- activity. EMF values were measured relative to Mettler Toledo DX200, PIMS/C_8-IL, PIMS/C_{12}-IL and P(VdF-*co*-HFP)/C_8-IL reference electrodes. Reference potential stability measurements were performed by placing PIMS/C_8-IL and PIMS/C_{12}-IL reference electrodes into stirred deionized water. Potentials were measured for 24 h relative to a conventional Mettler Toledo DX200 free-flowing double junction reference electrode (with a 1.0 M LiOAc bridge electrolyte and AgCl saturated 3.0 M KCl inner reference electrolyte).

Conductivity and impedance measurements

All impedance measurements were performed on a Solartron 1255B frequency response analyzer with an SI 1287 electrochemical interface (Farnborough, Hampshire, U.K.) controlled by ZPlot software (Scribner Associates, Southern Pines, NC). Measurements were performed over the frequency range from 100 kHz to 0.1 Hz at frequencies separated by 0.1 units on the logarithmic scale. Measurements were performed at the open circuit potential with an AC amplitude of 100 mV. PIMS/C_8-IL, PIMS/C_{12}-IL, and P(VdF-*co*-HFP)/C_8-IL impedance spectra were measured using a three-electrode cell with a AgCl-coated Ag wire reference and Pt gauze (5.08 × 1.27 cm^2) counter electrode.[209] All electrodes were immersed in 0.10 M KCl solutions.

Conductivity measurements were performed on PIMS/C_8-IL, PIMS/C_{12}-IL, and P(VdF-*co*-HFP)/C_8-IL using a custom made two-electrode cell at 25 °C. Sheets of each

material were cut into known areas and thicknesses. Conductivity was calculated as $l/(RA)$, where l is the sample thickness, A is the sample area, and R is the bulk resistance. Bulk resistances were determined from the frequency independent plateaus of the real components of the impedance. Each measurement was repeated with three different values of l/A ranging from 0.06–0.32 cm^{-1} to determine if interfacial resistance significantly contributed to the measured resistance.

4.3 Results and Discussion

Characterization of nanostructured morphology

The macroscopic performance of the PIMS reference electrodes is enabled by the distinct nanostructured morphology of the polymer/IL composite. Heating the homogeneous PIMS reaction mixture at 110 °C leads to a controlled growth of divinylbenzene-crosslinked polystyrene blocks (i.e., P(S-*co*-DVB)) from the PMMA macro-chain-transfer agent by RAFT polymerization. During this reaction, the IL partitions into the IL-miscible phase (PMMA in this case). The simultaneous cross-linking by DVB kinetically traps the system in a bicontinuous morphology of cross-linked polystyrene and sample-spanning conducting nanochannels.[155] The DSC results (Figure 4.10) indicate that the glass temperature (T_g) for the PMMA/IL phase of the crosslinked nanostructured material matches the T_g of a PMMA+IL mixture of the same concentration, thus supporting the complete partitioning of the IL to the PMMA-rich microphase to form a conducting domain.

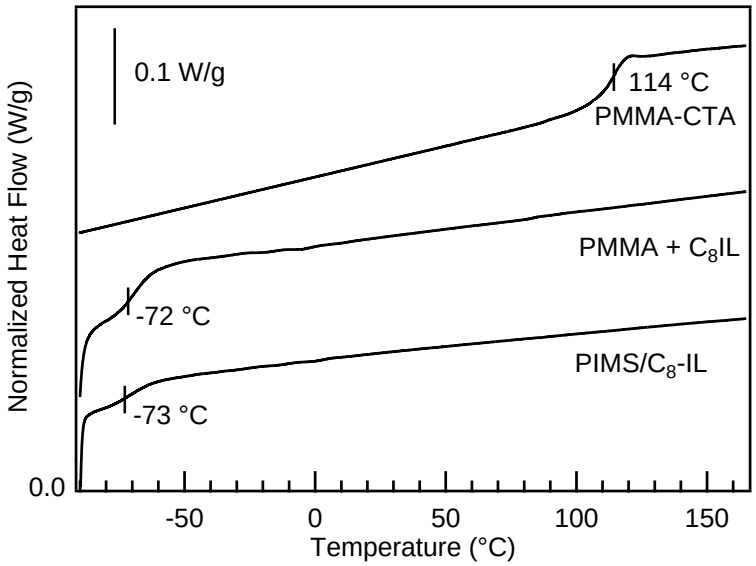

Figure 4.10: DSC thermograms for PMMA-CTA, PMMA+C_8-IL, and PIMS/C_8-IL composites. The traces represent the second heating cycle (exothermic flow down). The IL plasticizes the conducting phase of the PIMS polymer/IL composite.

We studied the PIMS/C_8-IL morphology with SAXS. The typical scattering profile (Figure 4.11b) exhibits a broad principal scattering peak at q^* and a secondary shoulder at $2q^*$. As shown previously, this scattering profile is typical for a microphase-separated morphology lacking long-range order.[12,206] The lengthscale of compositional heterogeneities is approximately 40 nm. The average domain spacing, d, determined by the position of q^* ($d = 2\pi/q^*$) slightly increases with increasing IL content, which is consistent with the behavior of the IL as a selective solvent for PMMA.[140,210] The PMMA/IL phase occupies about 60% v/v; therefore, the characteristic size of the PMMA/IL nanochannels is approximately 24 nm (40 nm × 0.6).

TEM imaging (Figure 4.11c) corroborates the SAXS results, indicating the formation of a disordered morphology. In the image, the bright regions are cross-linked polystyrene domains, whereas the denser PMMA/IL regions appear dark. The TEM images depicting inter-penetrating domains of cross-linked polystyrene and PMMA/IL along with the SAXS

profile are consistent with other reported systems exhibiting a microphase-separated bicontinuous network morphology without long-range order.[124,130]

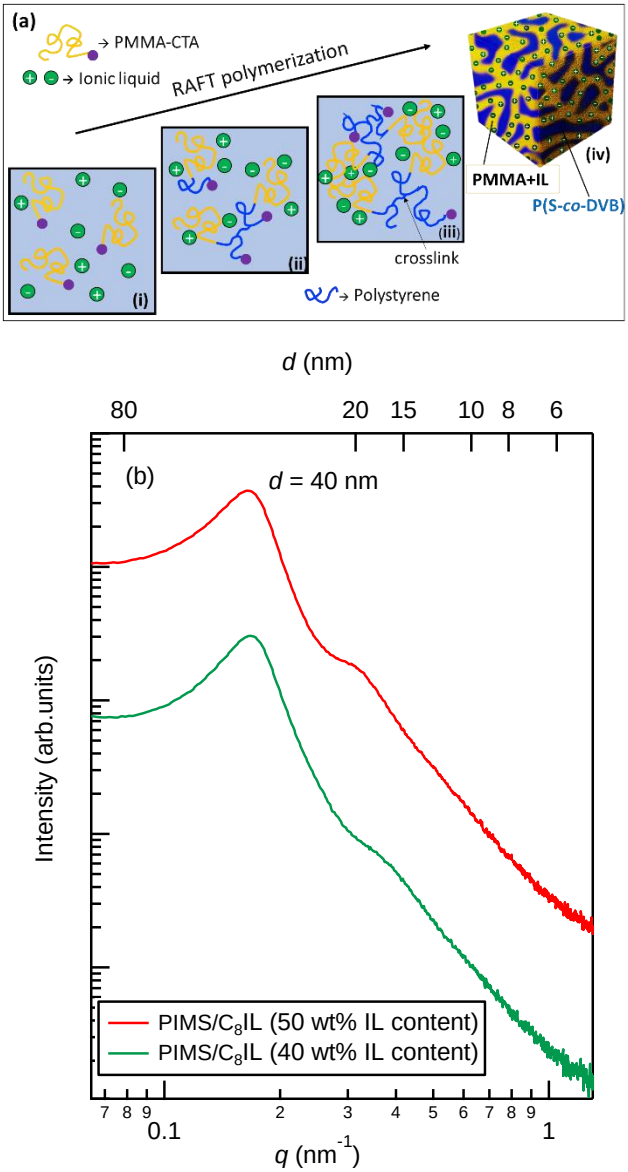

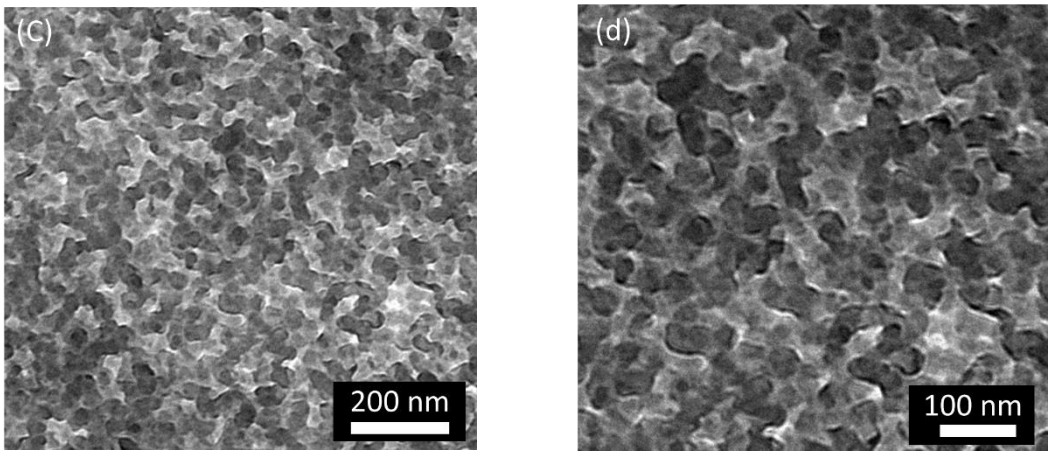

Figure 4.11: (a) Polymer chain growth and IL partitioning during PIMS. (i) PMMA-CTA is dissolved in a mixture of styrene and the crosslinker DVB (denoted by blue background), with IL. Heating the reaction mixture induces the growth of polystyrene chains (ii) and simultaneous cross-linking by DVB (iii), (iv) bicontinuous morphology of cross-linked polystyrene and sample-spanning conducting nanochannels (PMMA+IL). (b) SAXS for PIMS/C_8-IL samples prepared with varying IL content. The length scale of compositional heterogeneities increases slightly with increasing IL concentration. (c, d) TEM micrographs of PIMS/C_8-IL (50 wt% IL content) sample. The cross-linked polystyrene domain appears bright, whereas the denser PMMA/IL phase appears dark.

Electrode potentials in KCl electrolyte solutions

Electrode potentials were measured by immersion of the reference electrodes into aqueous solutions of varying mean K^+/Cl^- activity to determine the reproducibility and stability of the reference potentials relative to a conventional free-flowing liquid junction reference electrode[207] (Figure 4.12). Both the PIMS/C_8-IL and PIMS/C_{12}-IL reference electrodes had potentials that varied by less than 3 mV over almost five decades of mean K^+/Cl^- solution activity. These variations correspond to errors of less than 5% for potentiometric measurements of monovalent ions.[211] To compare the performance of the PIMS reference electrodes with a control system, we prepared three P(VdF-*co*-HFP)/C_8-IL gel reference electrodes, the only other reported example of a free-standing IL-based reference electrode. Each of the PIMS reference electrodes performed as well as the P(Vdf-*co*-HFP)/C_8-IL reference electrodes reported previously (Figure 4.12).[81] These results confirm that the PIMS reference electrodes are suitable for electrochemical measurements

in solutions over a wide range of hydrophilic electrolyte concentrations. This is important when measuring in solutions of low electrolyte concentrations, where nanoporous glass frit reference electrodes exhibit variations of up to 150 mV.[201] In fact, these reference electrodes also provided stable reference potential in deionized, purified water, as well as in the KCl solutions (Figure 4.12). This property is especially useful for measurements of environmental samples of low ionic strength, as pointed out by Kakiuchi and co-workers.[81]

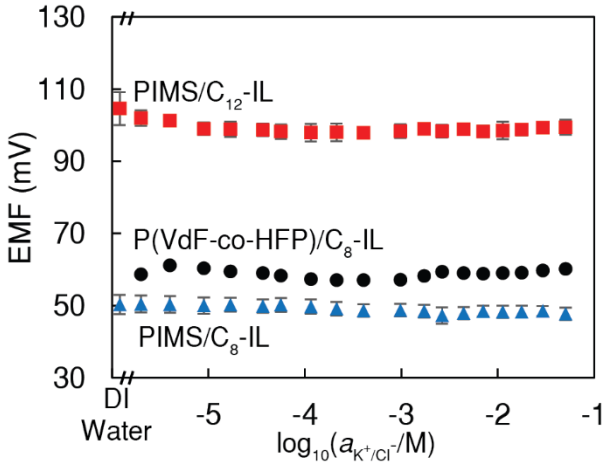

Figure 4.12: EMF of reference electrodes PIMS/C_8-IL, PIMS/C_{12}-IL, and P(VdF-*co*-HFP)/C_8-IL as a function of mean K^+/Cl^- activity. Left-most points for PIMS/C_8-IL and PIMS/C_{12}-IL are EMF values in deionized, purified water (18.2 MΩ cm specific resistance). EMF values were measured against a conventional reference electrode with a free-flowing double junction. All EMF values are corrected for liquid junction potentials at the conventional reference electrode. PIMS/C_8-IL and PIMS/C_{12}-IL error bars represent the standard deviation in the EMF of three reference electrodes samples, respectively.

Reproducibility of PIMS reference electrode potentials

Potentials from Figure 4.12 were used to calculate reference potentials for each PIMS reference electrode. PIMS/C_8-IL and PIMS/C_{12}-IL have standard potentials versus the standard hydrogen electrode of 0.262 ± 0.002 V and 0.313 ± 0.002 V, respectively. It is noteworthy that the potentials for P(VdF-*co*-HFP)/C_8-IL and PIMS/C_8-IL reference electrodes differ by only 0.008 V, which is within the magnitude of uncertainty of the

electrode-to-electrode potential reproducibility.[81] This result suggests that the AgCl-saturated C_8-IL and C_8-IL/water interfaces in both studies are equivalent, independent of the IL distribution within the bulk composite material.

The PIMS/C_{12}-IL standard reference potential differs from that of PIMS/C_8-IL by 0.051 V. However, the difference between the standard ion-transfer potentials of 1-octyl-3-methylimidazolium and 1-dodecyl-3-methylimidazolium when transferred from the pure ionic liquid (paired with [Ntf_2]) to water is 0.15 V, which should correspond directly to the difference in standard reference potentials of the two reference electrodes.[192,196] This result indicates that the potentials between the AgCl-coated Ag wires and the corresponding AgCl-saturated ionic liquids differ. This may reflect different solubilities of AgCl in the two ionic liquids.

Comparison of PIMS and free-flow reference electrodes

To assess the performance of the PIMS reference electrodes, a potentiometric experiment was conducted using AgCl-coated Ag wires to measure the mean Cl^- activity in aqueous KCl solutions. Figure 4.13 summarizes the cell potentials measured against PIMS/C_8-IL, PIMS/C_{12}-IL, and free-flowing double-junction reference electrodes. Each of the three reference electrodes provided a Nernstian response to the mean Cl^- activity. However, it should be noted that unlike the free-flowing double-junction reference electrodes, the PIMS reference electrodes do not require corrections for liquid junction potentials. Whereas such corrections are feasible for samples of relatively well-known content, they are typically not possible for samples of unknown composition.[192] Under such circumstances, PIMS reference electrodes appear better suited than free-flowing reference electrodes.

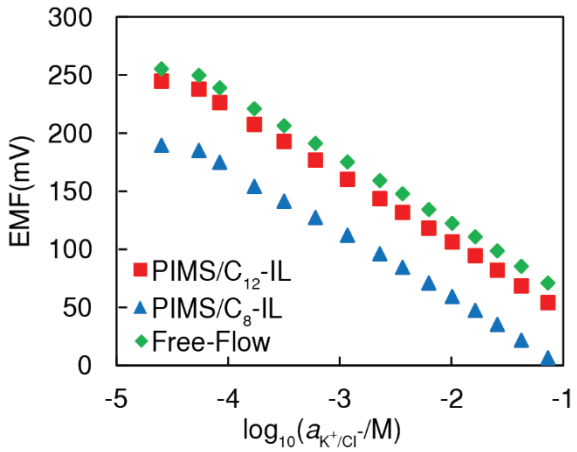

Figure 4.13: EMF of a AgCl-coated Ag wire in KCl solutions of varying mean Cl^- activity measured against PIMS/C_8-IL, PIMS/C_{12}-IL, and free-flowing double-junction reference electrodes. Potentials measured using the free-flowing double-junction reference electrode are corrected for liquid junction potentials.

Stability of PIMS reference electrode potentials in deionized water

One of the particularly promising applications of ionic liquid reference electrodes is in the measurement of potentials in solutions of low ionic strength.[196] Therefore, we determined the reference potential stability of PIMS reference electrodes when exposed for a total of 24 h to deionized water that was not previously exposed to ionic liquid. Over the initial 1 h, reference potentials of electrodes based on PIMS/C_8-IL or PIMS/C_{12}-IL changed by approximately 2 and 6 mV, respectively (Figure 4.14). Subsequently, potentials began to rise slowly, with the PIMS/C_8-IL and PIMS/C_{12}-IL reference electrodes exhibiting potential drifts of 1.5 mV/h and 0.7 mV/h, respectively, over 24 h. These results indicate that the PIMS based reference electrode potentials are stable for routine measurements over a period of a few hours. However, more studies will need to be conducted to assess and further improve the long-term performance.

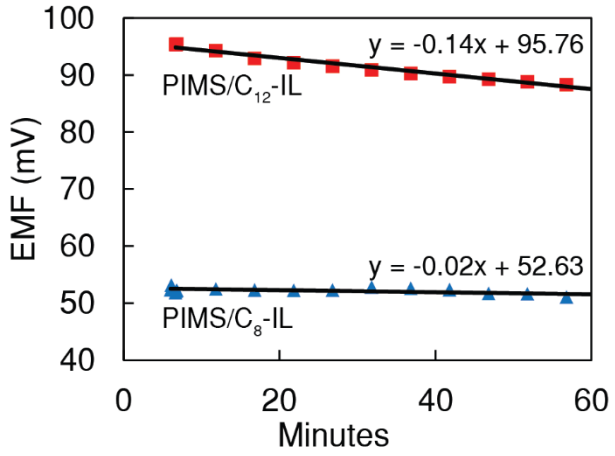

Figure 4.14: EMF of PIMS/C_8-IL and PIMS/C_{12}-IL reference electrodes as a function of time in deionized water (18.2 MΩ cm specific resistance). EMF values were measured against a conventional reference electrode with a free-flowing double junction. Solid lines indicate data fitted to a line.

Ionic conductivity

The long-range continuity of the conducting nanochannels (Figure 4.11c) enables efficient transport of ions, which allows for a high conductivity between the AgCl-coated Ag wire and the aqueous sample solution. Such high ionic conductivity is required for the design of miniaturized reference electrodes, where the resistance of the polymer/IL material may be limiting the total resistance of the reference electrode. To compare the different IL-doped materials with one another, the conductivities of PIMS/C_8-IL, PIMS/C_{12}-IL, and P(VdF-*co*-HFP)/ C_8-IL composites were determined. All three materials have ionic conductivities on the order of tens of μS/cm: PIMS/C_8-IL ≈ 66 μS/cm, PIMS/C_{12}-IL ≈ 34 μS/cm, and P(VdF-*co*-HFP)/C_8-IL ≈ 15 μS/cm. This shows that the conductivities of all three composites fall in a range that allows for the design and fabrication of reference electrodes that are more than adequate for measurements with commercially available voltmeters with high input impedance (~10^{15} Ω), discussed in further detail in the next section.

To characterize the electrochemical properties of the PIMS reference electrodes further, impedance measurements were performed with the fully assembled PIMS reference electrodes in 100 mM KCl solutions, using a three-electrode cell. Bulk resistance was determined from the minimum in the Nyquist plot of the negative imaginary component of the impedance, Z'', versus the real component of the impedance, Z' (Figure 4.15). Qualitative assessment of these spectra shows bulk resistances that varied from 75–150 kΩ, a relatively small variability that can be explained by the lack of careful control of the reference electrode geometry. As noted previously, this resistance is much lower than the input resistance of commercially available voltmeters (~10^{15} Ω).

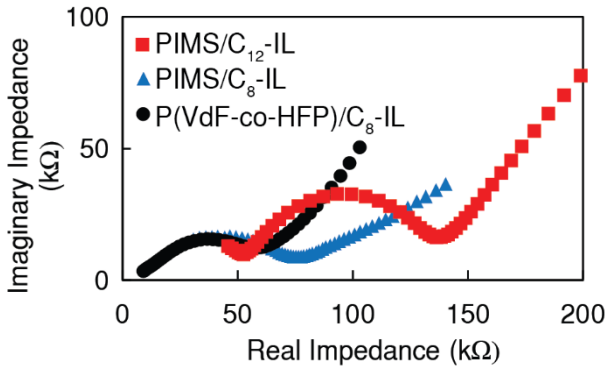

Figure 4.15: Impedance spectra of PIMS/C_8-IL, PIMS/C_{12}-IL, and P(VdF-*co*-HFP)/ C_8-IL reference electrodes. Data were taken from 10^5 to 1 Hz using a three-electrode cell. The reference electrode was a AgCl-coated Ag wire, and the counter electrode was a Pt gauze.

Practical preparation of PIMS reference electrodes

The PIMS design strategy, which involves solidification of a liquid reaction precursor, permits efficient control of not only the nanostructure of the ion-doped block copolymer but also the external shape of the reference electrodes. In the course of the reaction, the AgCl-coated wire is firmly encapsulated within the solid polymer/IL composite.

In contrast, the preparation of the P(VdF-*co*-HFP) gel reference electrodes[81] was, in our hands, not without difficulties. While solution casting of polymer/IL mixtures to

prepare planar ion gels for gate dielectrics for organic electronics, actuators, and gas separation membranes is a well-understood and widely-implemented technique,[190,212] sequential deposition of polymer/IL composites onto an Ag wire requires repeated dipping of the wire into a polymer/IL + acetone mixture and drying of the gel on the wire (ensuring no acetone is trapped into the system). To achieve substantially thick reference electrodes, the procedure needs to be repeated multiple times. Following this procedure, we obtained a tear-drop-shaped polymer/IL gel deposit onto the silver wire, similar to the one reported.[81] However, the bottom tip of the wire had to be insulated with commercial silicone sealant to compensate for the poor gel coverage (Figure 4.9).

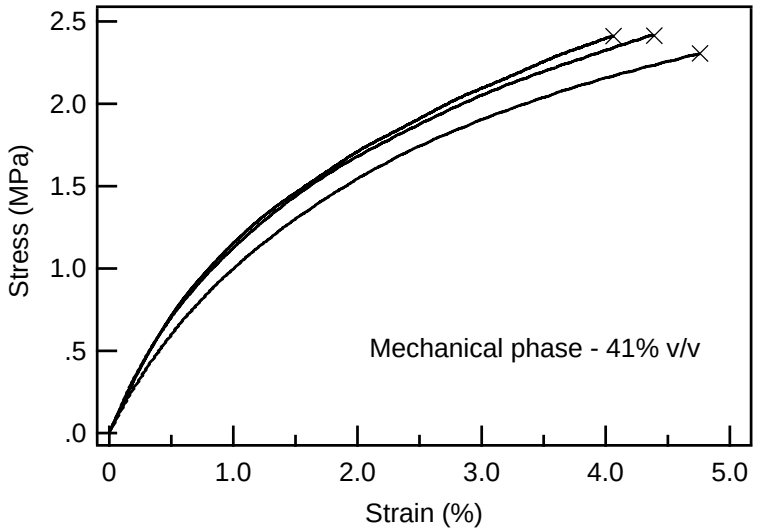

Figure 4.16: Stress-strain curves for three PIMS/C_8-IL (50% w/w IL content) samples. × indicate break points.

In comparison, designing PIMS reference electrodes involves a solvent-free, one-step synthetic strategy with excellent control over the shape as well as ensuring that the AgCl-coated wire is completely covered by PIMS/IL composite. In addition, PIMS/C_8-IL composites exhibit excellent mechanical robustness, with an ultimate tensile strength of ≈ 2.5 MPa (Figure 4.16) and thermal stability up to 350 °C (Figure 4.17). The thermal stability of the PIMS/IL composites would allow for their use with sensing electrodes that

are able to withstand high temperatures[213] and cleaning-in-place and sterilization treatments.[214]

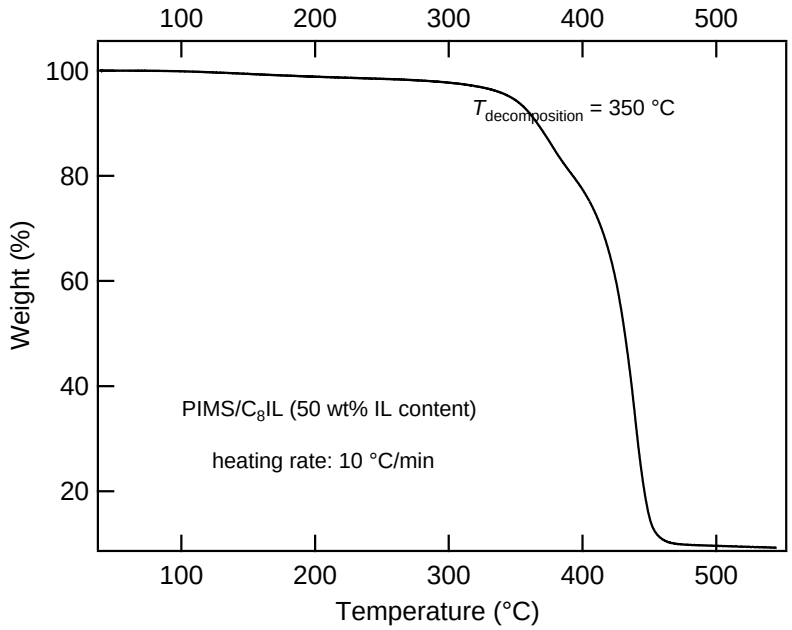

Figure 4.17: Thermogravimetric curve of the PIMS/C_8-IL sample (50 wt% IL content) under nitrogen (heating rate: 10 °C/min). The sample decomposed at 350 °C.

This robustness allows for free-standing reference electrodes to be designed in almost any geometry to meet the needs of the electrochemical problem. The PIMS design strategy permits control of the reference electrode shape. The easy-to-process liquid reaction precursor undergoes polymerization and simultaneous in-situ cross-linking, thereby solidifying to adopt the shape of the reaction container or mold. In the current study, glass molds were obtained by use of the bottom section (approximately 3 cm) of nuclear magnetic resonance (NMR) spectroscopy tubes (5 mm outer diameter). The reaction mixture was poured into the glass mold, which was then sealed using a rubber septum. Miniaturized reference electrodes (Figure 4.18b) were obtained by breaking the glass mold.

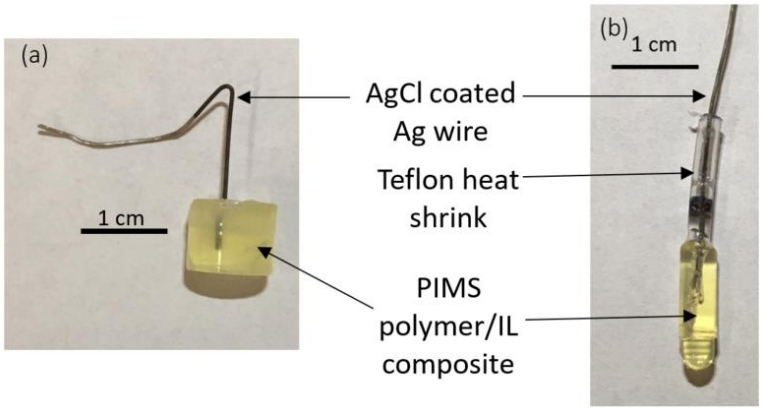

Figure 4.18: (a) PIMS reference electrode samples prepared using glass vials. (b) Samples prepared using NMR tube glass molds.

4.4 Conclusions

The preparation of ready-to-use ionic liquid-based reference electrodes using a polymerization-induced microphase separation strategy has been described. The merits of the PIMS strategy include that it (i) is solvent-free, (ii) allows fabrication in a single step, (iii) results in self-supporting, mechanically robust reference electrodes, and (iv) offers control over the size and shape of the reference electrode.

Reference electrodes based on both PIMS/C_8-IL and PIMS/C_{12}-IL showed stable and reproducible potentials that vary by less than 3 mV when exposed to solutions ranging from deionized, purified water to 100 mM KCl solutions. These results indicate that these electrodes are well suited for electrochemical measurements in solutions containing hydrophilic electrolytes and in solutions of low ionic strength. PIMS/C_8-IL and PIMS/C_{12}-IL reference electrodes showed reproducible potentials for replicates of 0.262 ± 0.002 V and 0.313 ± 0.002 V versus the standard hydrogen electrode, respectively. This potential reproducibility is especially useful when striving for calibration-free electrochemical sensors.[215] Moreover, ionic-liquid based reference electrodes are not only beneficial for their potential reproducibility, but also for their ease of maintenance.[194]

Chapter 5 – Concluding Remarks

5.1 Summary

The goal of this thesis is to develop a framework for building nanostructured high-conductive polymer electrolyte membranes (PEMs) that simultaneously manifest high-temperature stability and mechanical robustness. In particular, the thesis details development of three PEM systems: (i) high-temperature, anhydrous proton conducting PEMs, (ii) PEMs with high Li^+ conductivity at ambient temperature, and (iii) ionic liquid (IL)-based reference electrodes with a hydrophobic polymeric matrix. A simple, yet versatile polymerization route – termed polymerization-induced microphase separation (PIMS) – facilitated PEMs with bicontinuous morphology and cross-linked mechanical domains that enabled the PEMs to exhibit a combination of high modulus and high ionic conductivity.

Work detailed in Chapter 2 revealed that PIMS PEMs are glassy solids at room-temperature, and soften only moderately at elevated temperatures as high as 200 °C. High-temperature mechanical stability furnished by the cross-linked polystyrene (PS) scaffold enables a much wider operation-temperature window than diblock polymer electrolytes that rely on the glassy block for structural integrity. Similarly, work in Chapter 3 highlighted that ionic conductivity of PIMS PEMs is not limited by network defects such as grain boundaries that compromise performance of self-assembled diblock polymer electrolytes. Incorporation of succinonitrile (SN) rendered the poly(ethylene oxide)/lithium (Li) salt conducting domains completely amorphous, resulting in outstanding conductivities (~ 0.35 mS/cm) at 30 °C. Another advantage of the PIMS strategy is the ease of processing the liquid reaction mixture, followed by *in situ* solidification to obtain solid PEMs. This aspect was utilized in developing a solvent-free, one-step design of IL-based reference electrodes, as detailed in Chapter 4.

5.2 Proposed Future Directions

High-temperature proton conducting PEMs

Proton conducting PEO/IL PIMS PEMs, discussed in Chapter 2, exhibit an outstanding combination of high conductivity and superior thermal and mechanical robustness. However, the conductivity of PIMS PEMs falls short in comparison to commercial high-temperature fuel cell technologies – phosphoric acid (PA)-polybenzimidazole (PBI) membranes (Figure 5.1a).[16] The conductivity of the PIMS PEMs is ultimately limited by the inherent conductivity of the protic ILs.

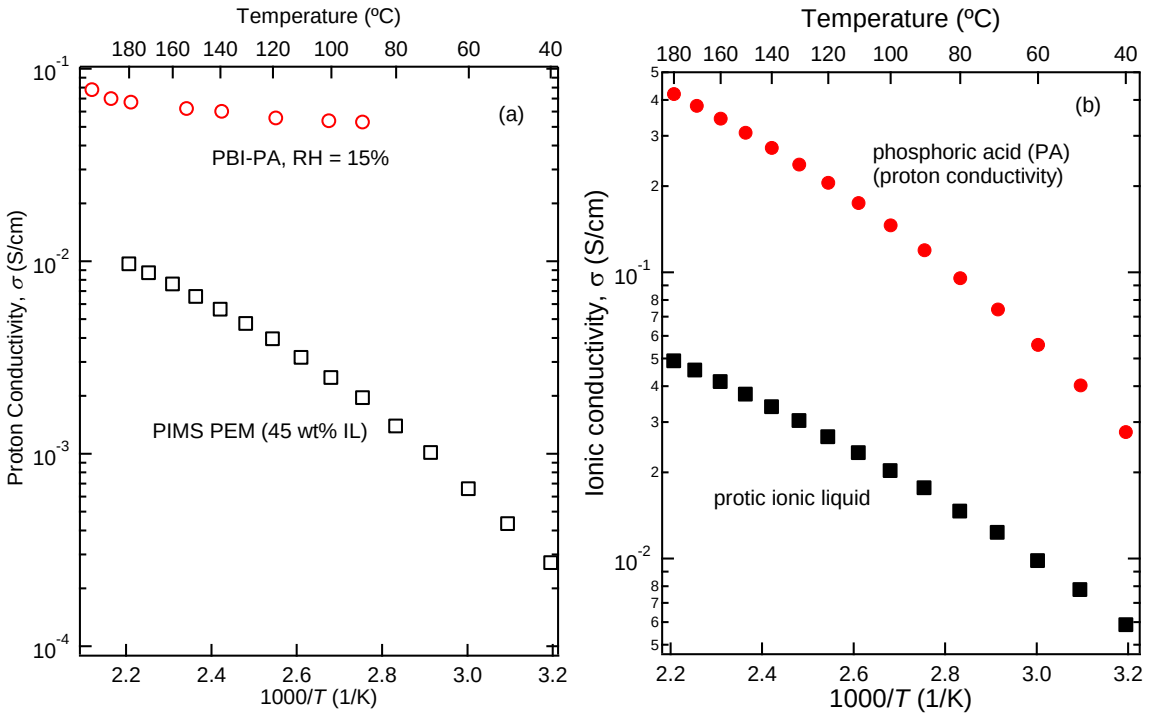

Figure 5.1: (a) Proton conductivity of PBI-PA membranes[16] and PEO/IL PIMS PEMs. (b) Ionic conductivity of bulk PA[16] and protic IL, [HEIm][TFSI].

One strategy to improve conductivity of PIMS PEMs would be to replace PA as the electrolyte and use polymers with basic moieties such as poly(vinylpyridine) (P2VP or P4VP) as the conducting phase matrix. PA exhibits proton conductivity an order of magnitude higher than protic ILs (Figure 5.1b) as well as a high proton transference number

($t^+ \approx 0.98$).[16] However, the one-pot strategy used to develop protic IL PEMs would not work, as PA is immiscible with styrene (S)/divinylbenzene (DVB) monomer mixture.

One approach to designing PA-PIMS PEMs could be to prepare neat P2VP/cross-linked PS membranes (no IL) and dope them with PA. However, as observed in preliminary experiments, neat P2VP cross-linked monoliths typically uptake just 4 wt% PA, probably due to the restriction on volume expansion imposed by the chemically cross-linked PS framework. A better approach would be to design IL PEMs and then replace the IL with an equivalent amount of PA (Figure 5.2). In general, this strategy could be used to incorporate other protic electrolytes such as phosphotungstic acid and silicotungstic acid, which also face immiscibility issues with S/DVB monomer mixture.[17]

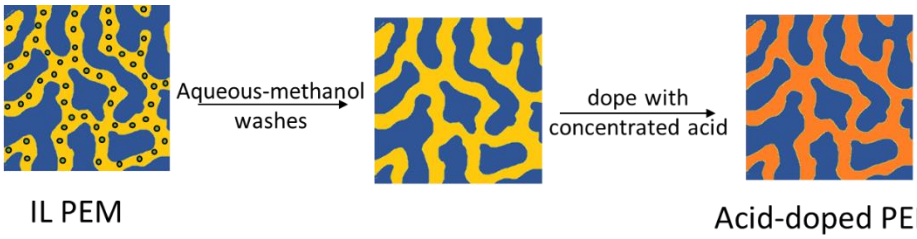

Figure 5.2: Preparation of PA PIMS PEMs. The proposed strategy involves removing the IL from PEMs and then swelling them with phosphoric acid.

Figure 5.3a shows results of a proof-of-concept test of the PA-PIMS PEMs idea. At first, IL-PEMs were prepared via RAFT polymerization of S/DVB off a P2VP macro chain -transfer agent (P2VP macro-CTA) (see Appendix A for details) and 35 wt% [HEIm][TFSI]. PA-PIMS PEMs were prepared as per the protocol shown in Figure 5.2. IL was removed by washing the IL-PEMs with water/methanol mixture several times. IL removal was confirmed by gravimetric analysis. The porous PEMs were then immersed in concentrated PA solution (≥85 wt%). PA content in the PEMs depended on several factors such as concentration of the doping PA solution, temperature and doping time.[17]

Figure 5.3a compares the conductivity of the PA-PEM (45 wt% PA) with that of bulk protic IL and IL-PEM (35 wt% IL). PA-PEM exhibits 3 times higher conductivity than its

IL counterpart. Proton transport in PA-PEMs prominently occurs via a fast Grotthuss mechanism, whereas vehicular transport of the $HEIm^+$ contributes to proton conductivity of IL-PEMs.[19] In addition, t^+ in PA-PEMs is expected to be ≈ 0.98,[16] thus it exhibits even higher proton conductivity compared to IL-PEMs where $t^+ \approx 0.65$.[172]

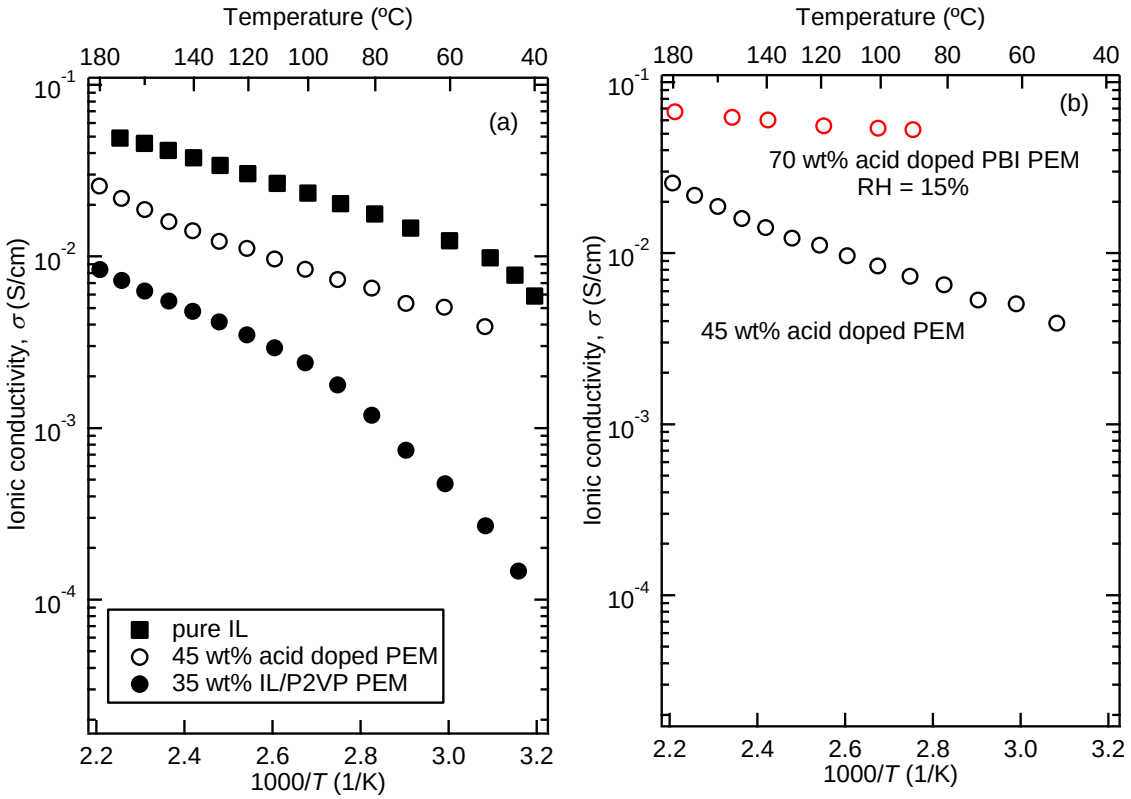

Figure 5.3: (a) Ionic conductivity of bulk protic IL [HEIm][TFSI], P2VP/PA-PIMS PEMs, and P2VP IL-PEMs. (b) Comparison of ionic conductivity observed in PBI/PA membranes (RH = 15%)[16] and PA-PIMS PEMs measured under anhydrous conditions.

However, ionic conductivity of the proof-of-concept PA-PEM (45 wt% PA) still falls short of PBI-PA membranes (70 wt% PA), about 3 times lower at 200 °C (Figure 5.3b). PBI-PA membranes typically have high acid loading (> 65% wt%).[17] Figure 5.3b shows the conductivity of a 70 wt% acid doped membrane. In the case of PA-PIMS PEMs, highest acid content achieved was 45 wt%. At higher acid loadings (> 45 wt%), acid leakage was observed. It should also be noted that the reported conductivity measurements for PBI-PA

membranes were performed at relative humidity (RH) = 15%, whereas PA-PIMS PEMs conductivity experiments were conducted under anhydrous conditions. Humidity has a huge influence on PA conductivity.[19] Under similar experimental conditions (RH = 15%), PA-PEMs could potentially exhibit better proton conductivity.

The performance of the proposed PA-PIMS PEMs could be improved by optimizing the volume fraction of P2VP domains and maximizing the acid content with a better understanding of the acid uptake step. Further study in terms of developing membrane electrode assemblies and measuring current densities and fuel crossover rates would be necessary to establish the true potential of the PIMS PEM as proton exchange membranes for high-temperature fuel cells.

Li^+ conducting PEMs

Given the promising conductivity and superior mechanical properties exhibited by PIMS PEMs, the natural progression is to investigate the performance of these PEMs in a Li-ion battery (LIB) setup. However, this is not necessarily straightforward. One of the major challenges in developing LIBs with solid PEMs is to achieve a good interfacial contact between the PEM and the electrodes.[30] In the case of PIMS PEMs, this issue could be resolved to some extent by developing the PEM directly on top of the cathode as depicted in Figure 5.4a, instead of preparing the PEM independently and then stacking it on the cathode. The proposed strategy involves reacting the PIMS reaction mixture on the surface of the cathode material, punching out the solid PEM + cathode composite, and followed by cell assembly procedures.

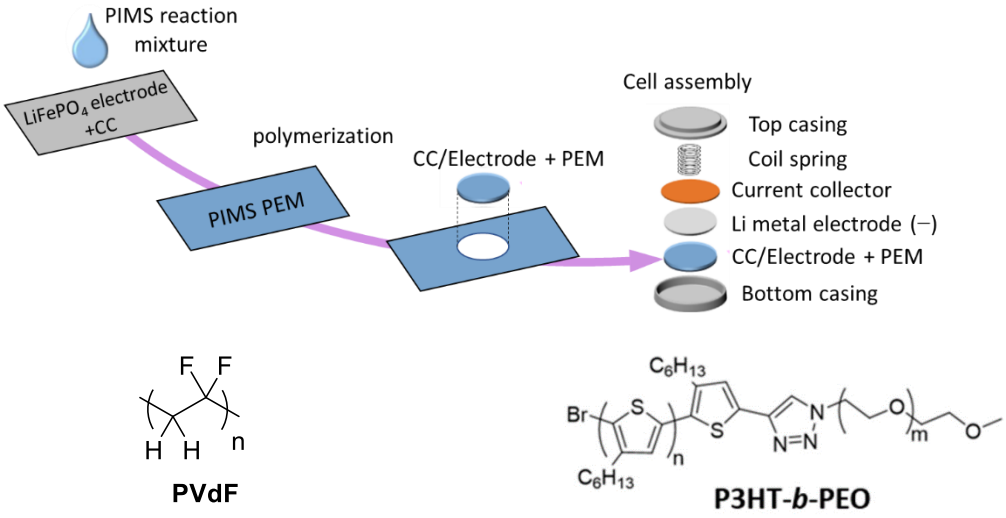

Figure 5.4: (a) Preparation of the PIMS PEM + electrode composite and coin cell assembly. (b) Binders used for electrode assembly – PVdF and P3HT-*b*-PEO.

The cathode + current collector (CC) composite films (grey panel in Figure 5.4a) used in LIBs are prepared by depositing a thin layer of cathode materials with doctor blade technique on aluminum CCs. The cathode materials are typically composed of 80 wt% electroactive materials ($LiFePO_4$ or $LiCoO_2$), 10 wt% PVdF (binder), and 10 wt % carbon black.[32] In the proposed process of developing PIMS PEMs on the cathode which is composed of highly hydrophobic components such as PVdF (Figure 5.4a), there is a strong possibility that the styrene and divinylbenzene monomers would preferentially wet the cathode surface. Such compositional inhomogeneity could lead to formation of an undesirable insulating PS skin layer.

The non-uniform wetting of the cathode surface by the PIMS reaction mixture could be resolved by employing the newly developed poly(3-hexylthiophene)-*block*-PEO (P3HT-*b*-PEO) binder (Figure 5.4b) in lieu of hydrophobic PVdF. Patel et al. reported that P3HT-*b*-PEO binder facilitated an excellent $LiFePO_4$ cathode performance (high charge/discharge capacities), and exhibited excellent compatibility with other electroactive materials such as V_2O_5 and $LiCoO_2$.[216] Tailoring the molar mass and the composition of

the P3HT-*b*-PEO binder would be critical in achieving a good PEM-cathode interfacial contact and homogenous PEMs. Upon successful assembly of the LIBs following the proposed strategy, the performance of the PIMS PEMs could be investigated in terms of electrochemical stability window, resistance to Li-metal dendrite growth, specific cell capacity, and battery lifetime, i.e., number of charge-discharge cycles.

References

(1) Goodenough, J. B.; Kim, Y. Challenges for Rechargeable Li Batteries. *Chem. Mater.* **2010**, *22*, 587–603.

(2) Houchins, C.; Kleen, G.; Spendelow, J.; Kopasz, J.; Peterson, D.; Garland, N.; Ho, D.; Marcinkoski, J.; Martin, K.; Tyler, R. U.S. DOE Progress Towards Developing Low-Cost, High Performance, Durable Polymer Electrolyte Membranes for Fuel Cell Applications. *Membranes* **2012**, *2*, 855–878.

(3) Young, W.-S.; Kuan, W.-F.; Epps, T. H., III. Block Copolymer Electrolytes for Rechargeable Lithium Batteries. *J. Polym. Sci. Part B Polym. Phys.* **2014**, *52*, 1–16.

(4) Morris, M. A.; An, H.; Lutkenhaus, J. L.; Epps, T. H., III. Harnessing the Power of Plastics: Nanostructured Polymer Systems in Lithium-Ion Batteries. *ACS Energy Lett.* **2017**, *2*, 1919–1936.

(5) Kim, S. Y.; Kim, S.; Park, M. J. Enhanced Proton Transport in Nanostructured Polymer Electrolyte/ionic Liquid Membranes under Water-Free Conditions. *Nat. Commun.* **2010**, *1*, 88.

(6) Kim, O.; Jo, G.; Park, Y. J.; Kim, S.; Park, M. J. Ion Transport Properties of Self-Assembled Polymer Electrolytes: The Role of Confinement and Interface. *J. Phys. Chem. Lett.* **2013**, *4*, 2111–2117.

(7) Virgili, J. M.; Nedoma, A. J.; Segalman, R. A.; Balsara, N. P. Ionic Liquid Distribution in Ordered Block Copolymer Solutions. *Macromolecules* **2010**, *43*, 3750–3756.

(8) Singh, M.; Odusanya, O.; Balsara, N. P. Nanostructured Polymer Electrolytes: Decoupling Ion Conduction and Mechanical Properties. *Polym. Mater. Sci. Eng.* **2006**, *95*, 846.

(9) Hoarfrost, M. L.; Segalman, R. A. Conductivity Scaling Relationships for Nanostructured Block copolymer/Ionic Liquid Membranes. *ACS Macro Lett.* **2012**, *1*, 937–943.

(10) Hoarfrost, M. L.; Segalman, R. A. Ionic Conductivity of Nanostructured Block Copolymer/Ionic Liquid Membranes. *Macromolecules* **2011**, *44*, 5281–5288.

(11) Hallinan, D. T.; Balsara, N. P. Polymer Electrolytes. *Annu. Rev. Mater. Res.* **2013**, *43*, 503–525.

(12) Schulze, M. W.; McIntosh, L. D.; Hillmyer, M. A.; Lodge, T. P. High-Modulus, High-Conductivity Nanostructured Polymer Electrolyte Membranes via Polymerization-Induced Phase Separation. *Nano Lett.* **2014**, *14*, 122–126.

(13) Wang, Y.; Chen, K. S.; Mishler, J.; Cho, S. C.; Adroher, X. C. A Review of Polymer Electrolyte Membrane Fuel Cells: Technology, Applications, and Needs on Fundamental Research. *Appl. Energy* **2011**, *88*, 981–1007.

(14) Chandan, A.; Hattenberger, M.; El-kharouf, A.; Du, S.; Dhir, A.; Self, V.; Pollet, B. G.; Ingram, A.; Bujalski, W. High Temperature (HT) Polymer Electrolyte Membrane Fuel Cells (PEMFC) – A Review. *J. Power Sources* **2013**, *231*, 264–278.

(15) Yasuda, T.; Watanabe, M. Protic Ionic Liquids: Fuel Cell Applications. *MRS Bull.* **2013**, *38*, 560–566.

(16) Li, Q.; Jensen, J. O.; Savinell, R. F.; Bjerrum, N. J. High Temperature Proton Exchange Membranes Based on Polybenzimidazoles for Fuel Cells. *Prog. Polym. Sci.* **2009**, *34*, 449–477.

(17) Li, Q.; He, R.; Jensen, J. O.; Bjerrum, N. J. Approaches and Recent Development of Polymer Electrolyte Membranes for Fuel Cells Operating above 100 °C. *Chem. Mater.* **2003**, *15*, 4896–4915.

(18) Li, Q.; He, R.; Gao, J.-A.; Jensen, J. O.; Bjerrum, N. J. The CO Poisoning Effect in PEMFCs Operational at Temperatures up to 200°C. *J. Electrochem. Soc.* **2003**, *150*, A1599–A1605.

(19) Vilčiauskas, L.; Tuckerman, M. E.; Bester, G.; Paddison, S. J.; Kreuer, K.-D. The Mechanism of Proton Conduction in Phosphoric Acid. *Nat. Chem.* **2012**, *4*, 461–466.

(20) Li, Q.; He, R.; Jensen, J. O.; Bjerrum, N. J. PBI-Based Polymer Membranes for High Temperature Fuel Cells - Preparation, Characterization and Fuel Cell Demonstration. *Fuel Cells* **2004**, *4*, 147–159.

(21) Bara, J. E.; Camper, D. E.; Gin, D. L.; Noble, R. D. Room-Temperature Ionic Liquids and Composite Materials: Platform Technologies for Carbon Dioxide Capture. *Acc. Chem. Res.* **2010**, *43*, 152–159.

(22) Noda, A.; Susan, M. A. B. H.; Kudo, K.; Mitsushima, S.; Hayamizu, K.; Watanabe, M. Brønsted Acid - Base Ionic Liquids as Proton-Conducting Nonaqueous Electrolytes. *J. Phys. Chem. B* **2003**, *107*, 4024–4033.

(23) Fernicola, A.; Panero, S.; Scrosati, B.; Tamada, M.; Ohno, H. New Types of Brönsted Acid-Base Ionic Liquids-Based Membranes for Applications in PEMFCs. *Chemphyschem* **2007**, *8*, 1103–1107.

(24) Green, M. D.; Long, T. E. Designing Imidazole-Based Ionic Liquids and Ionic Liquid Monomers for Emerging Technologies. *Polym. Rev.* **2009**, *49*, 291–314.

(25) Lee, S.-Y.; Ogawa, A.; Kanno, M.; Nakamoto, H.; Yasuda, T.; Watanabe, M. Nonhumidified Intermediate Temperature Fuel Cells Using Protic Ionic Liquids. *J. Am. Chem. Soc.* **2010**, *132*, 9764–9773.

(26) Ohno, H.; Yoshizawa, M. Ion Conductive Characteristics of Ionic Liquids Prepared by Neutralization of Alkylimidazoles. *Solid State Ionics* **2002**, *154*, 303–309.

(27) Hubner, G.; Roduner, E. EPR Investigation of HO• Radical Initiated Degradation Reactions of Sulphonated Aromatics as Model Compounds for Fuel Cell Proton Conducting Membranes. *J. Mater. Chem.* **1999**, *9*, 409–418.

(28) Castro, E. De. PBI-Phosphoric Acid Based Membrane Electrode Assemblies. *Fuel Cells* **2009**, *3*, 5–20.

(29) Steele, B.; Heinzel, A. Materials for Fuel-Cell Technologies. *Nature* **2001**, *414*, 345–352.

(30) Tarascon, J.-M. M.; Armand, M. Issues and Challenges Facing Rechargeable Lithium Batteries. *Nature* **2001**, *414*, 359–367.

(31) Quartarone, E.; Mustarelli, P.; Links, D. A. Electrolytes for Solid-State Lithium Rechargeable Batteries: Recent Advances and Perspectives. *Chem. Soc. Rev.* **2011**, *40*, 2525–2540.

(32) Wakihara, M.; Yamamoto, O. Lithium Ion Batteries: Fundamentals and Performance. *J. Power Sources* **2011**, *140*, 24–38.

(33) Zhang, H.; Zhou, M.-Y.; Lin, C.-E.; Zhu, B.-K. Progress in Polymeric Separators for Lithium Ion Batteries. *RSC Adv.* **2015**, *5*, 89848–89860.

(34) Halalay, I. C.; Lukitsch, M. J.; Balogh, M. P.; Wong, C. A. Nanoindentation Testing of Separators for Lithium-Ion Batteries. *J. Power Sources* **2013**, *238*, 469–477.

(35) Yamaki, J. Design of the Lithium Anode and Electrolytes in Lithium Secondary Batteries. *RSC Adv.* **2015**, *5*, 89872–89890.

(36) Goodenough, J. B.; Park, K.-S. The Li-Ion Rechargeable Battery: A Perspective. *J. Am. Chem. Soc.* **2013**, *135*, 1167–1176.

(37) Monroe, C.; Newman, J. Dendrite Growth in Lithium/Polymer Systems: A Propagation Model for Liquid Electrolytes under Galvanostatic Conditions. *J. Electrochem. Soc.* **2003**, *150*, A1377–A1384.

(38) Monroe, C.; Newman, J. The Effect of Interfacial Deformation on Electrodeposition Kinetics. *J. Electrochem. Soc.* **2004**, *151*, A880–A886.

(39) Monroe, C.; Newman, J. The Impact of Elastic Deformation on Deposition Kinetics at Lithium/Polymer Interfaces. *J. Electrochem. Soc.* **2005**, *152*, A396–A404.

(40) Hallinan, D. T.; Mullin, S. A.; Stone, G. M.; Balsara, N. P. Lithium Metal Stability in Batteries with Block Copolymer Electrolytes. *J. Electrochem. Soc.* **2013**, *160*, A464–A470.

(41) Xue, Z.; He, D.; Xie, X. Poly(ethylene oxide)-Based Electrolytes for Lithium-Ion Batteries. *J. Mater. Chem. A* **2015**, *3*, 19218–19253.

(42) Lobaugh, J.; Voth, G. A. The Quantum Dynamics of an Excess Proton in Water. *J. Chem. Phys.* **1998**, *104*, 2056–2063.

(43) Chen, H. P.; Fergus, J. W.; Jang, B. Z. The Effect of Ethylene Carbonate and Salt Concentration on the Conductivity of Propylene Carbonate/Lithium Perchlorate Electrolytes. *J. Electrochem. Soc.* **2000**, *147*, 399–409.

(44) Xu, K. Nonaqueous Liquid Electrolytes for Lithium-Based Rechargeable Batteries. *Chem. Rev.* **2004**, *104*, 4303–4418.

(45) Narayanan, S. R.; Yen, S. P.; Liu, L.; Greenbaum, S. G. Anhydrous Proton-Conducting Polymeric Electrolytes for Fuel Cells. *J. Phys. Chem. B* **2006**, *110*, 3942–3948.

(46) Sangoro, J. R.; Serghei, A.; Naumov, S.; Galvosas, P.; Kärger, J.; Wespe, C.; Bordusa, F.; Kremer, F. Charge Transport and Mass Transport in Imidazolium-Based Ionic Liquids. *Phys. Rev. E* **2008**, *77*, 51202.

(47) Welton, T. Room-Temperature Ionic Liquids. Solvents for Synthesis and Catalysis. *Chem. Rev.* **1999**, *99*, 2071–2084.

(48) Armand, M.; Endres, F.; MacFarlane, D. R.; Ohno, H.; Scrosati, B. Ionic-Liquid Materials for the Electrochemical Challenges of the Future. *Nat. Mater.* **2009**, *8*, 621–629.

(49) Mousavi, M. P. S.; Dittmer, A. J.; Wilson, B. E.; Hu, J.; Stein, A.; Bühlmann, P. Unbiased Quantification of the Electrochemical Stability Limits of Electrolytes and Ionic Liquids. *J. Electrochem. Soc.* **2015**, *162*, A2250–A2258.

(50) Tokuda, H.; Hayamizu, K.; Ishii, K.; Susan, M. A. B. H.; Watanabe, M. Physicochemical Properties and Structures of Room Temperature Ionic Liquids. 2. Variation of Alkyl Chain Length in Imidazolium Cation. *J. Phys. Chem. B* **2005**, *109*, 6103–6110.

(51) Tokuda, H.; Ishii, K.; Tsuzuki, S.; Hayamizu, K.; Susan, M. A. B. H.; Watanabe, M. Physicochemical Properties and Structures of Room-Temperature Ionic Liquids . 3 . Variation of Cationic Structures. *J. Phys. Chem. B* **2006**, *110*, 2833–2839.

(52) Kim, S. Y.; Lee, J.; Park, M. J. Proton Hopping and Diffusion Behavior of Sulfonated Block Copolymers Containing Ionic Liquids. *Macromolecules* **2014**, *47*, 1099–1108.

(53) Lu, J.; Yan, F.; Texter, J. Advanced Applications of Ionic Liquids in Polymer Science. *Prog. Polym. Sci.* **2009**, *34*, 431–448.

(54) Anderson, J. L.; Ding, J.; Welton, T.; Armstrong, D. W. Characterizing Ionic Liquids On the Basis of Multiple Solvation Interactions. *J. Am. Chem. Soc.* **2002**, *124*, 14247–14254.

(55) Fenton, D. E.; Parker, J. M.; Wright, P. V. Complexes of Alkali Metal Ions with Poly(ethylene oxide). *Polymer* **1973**, *14*, 589–594.

(56) Armand, M. B.; Chabagno, J. M.; Duclot, M. Poly-Ethers as Solid Electrolytes. In *Fast Ion Transport in Solids*; New York, 1979; pp 131–136.

(57) Epps, T. H., III.; Bailey, T. S.; Pham, H. D.; Bates, F. S. Phase Behavior of Lithium Perchlorate-Doped Poly(styrene-*b*-isoprene-*b*-ethylene oxide) Triblock Copolymers. *Chem. Mater.* **2002**, *14*, 1706–1714.

(58) Lascaud, S.; Perrier, M.; Vallee, A.; Besner, S.; Prud'homme, J.; Armand, M.

Phase Diagrams and Conductivity Behavior of Poly(ethylene oxide)-Molten Salt Rubbery Electrolytes. *Macromolecules* **1994**, *27*, 7469–7477.

(59) Albinsson, I.; Mellander, B. E.; Stevens, J. R. Ionic-Conductivity in Poly(propylene glycol) Complexed with Lithium and Sodium Triflate. *J. Chem. Phys.* **1992**, *96*, 681–690.

(60) Panday, A.; Mullin, S.; Gomez, E. D.; Wanakule, N.; Chen, V. L.; Hexemer, A.; Pople, J.; Balsara, N. P. Effect of Molecular Weight and Salt Concentration on Conductivity of Block Copolymer Electrolytes. *Macromolecules* **2009**, *42*, 4632–4637.

(61) Fan, L.-Z.; Wang, X. X.-L.; Long, F.; Wang, X. X.-L. Enhanced Ionic Conductivities in Composite Polymer Electrolytes by Using Succinonitrile as a Plasticizer. *Solid State Ionics* **2008**, *179*, 1772–1775.

(62) Vignarooban, K.; Dissanayake, M. A. K. L.; Albinsson, I.; Mellander, B.-E. Effect of TiO_2 Nano-Filler and EC Plasticizer on Electrical and Thermal Properties of Poly(ethylene Oxide) (PEO) Based Solid Polymer Electrolytes. *Solid State Ion.* **2014**, *266*, 25–28.

(63) Kim, Y.-T.; Smotkin, E. S. The Effect of Plasticizers on Transport and Electrochemical Properties of PEO-Based Electrolytes for Lithium Rechargeable Batteries. *Solid State Ionics* **2002**, *149*, 29–37.

(64) Soo, P.; Huang, B.; Jang, Y.-I.; Chiang, Y.-M.; Sadoway, D. R.; Mayes, A. M. Rubbery Block Copolymer Electrolytes for Solid-State Rechargeable Lithium Batteries. *J. Electrochem. Soc.* **1999**, *146*, 32.

(65) Kuan, W.-F.; Remy, R.; Mackay, M. E.; Epps, T. H., III. Controlled Ionic Conductivity via Tapered Block Polymer Electrolytes. *RSC Adv.* **2015**, *5*, 12597–12604.

(66) Kido, R.; Ueno, K.; Iwata, K.; Kitazawa, Y.; Imaizumi, S.; Mandai, T.; Dokko, K.; Watanabe, M. Li^+ Ion Transport in Polymer Electrolytes Based on a Glyme-Li Salt Solvate Ionic Liquid. *Electrochim. Acta* **2015**, *175*, 5–12.

(67) Ghosh, A.; Wang, C.; Kofinas, P. Block Copolymer Solid Battery Electrolyte with High Li-Ion Transference Number. *J. Electrochem. Soc.* **2010**, *157*, A846–A851.

(68) Ueno, K.; Yoshida, K.; Tsuchiya, M.; Tachikawa, N.; Dokko, K.; Watanabe, M. Glyme-Lithium Salt Equimolar Molten Mixtures: Concentrated Solutions or Solvate Ionic Liquids? *J. Phys. Chem. B* **2012**, *116*, 11323–11331.

(69) Zugmann, S.; Fleischmann, M.; Amereller, M.; Gschwind, R. M.; Wiemhöfer, H. D.; Gores, H. J. Measurement of Transference Numbers for Lithium Ion Electrolytes via Four Different Methods, A Comparative Study. *Electrochim. Acta* **2011**, *56*, 3926–3933.

(70) Zhang, H.; Li, C.; Piszcz, M.; Coya, E.; Rojo, T.; Rodriguez-Martinez, L. M.; Armand, M.; Zhou, Z. Single Lithium-Ion Conducting Solid Polymer Electrolytes: Advances and Perspectives. *Chem. Soc. Rev.* **2017**, *46*, 797–815.

(71) Jo, G.; Jeon, H.; Park, M. J. Synthesis of Polymer Electrolytes Based on

Poly(ethylene oxide) and an Anion-Stabilizing Hard Polymer for Enhancing Conductivity and Cation Transport. *ACS Macro Lett.* **2015**, *4*, 225–230.

(72) Rolland, J.; Poggi, E.; Vlad, A.; Gohy, J. F. Single-Ion Diblock Copolymers for Solid-State Polymer Electrolytes. *Polymer* **2015**, *68*, 344–352.

(73) Meziane, R.; Bonnet, J.-P.; Courty, M.; Djellab, K.; Armand, M. Single-Ion Polymer Electrolytes Based on a Delocalized Polyanion for Lithium Batteries. *Electrochim. Acta* **2011**, *57*, 14–19.

(74) Porcarelli, L.; Shaplov, A. S.; Salsamendi, M.; Nair, J. R.; Vygodskii, Y. S.; Mecerreyes, D.; Gerbaldi, C. Single-Ion Block Copoly(ionic Liquid)s as Electrolytes for All-Solid State Lithium Batteries. *ACS Appl. Mater. Interfaces* **2016**, *8*, 10350–10359.

(75) Lee, K. H.; Kang, M. S.; Zhang, S.; Gu, Y.; Lodge, T. P.; Frisbie, C. D. "Cut and Stick" rubbery Ion Gels as High Capacitance Gate Dielectrics. *Adv. Mater.* **2012**, *24*, 4457–4462.

(76) Chopade, S. A.; Anderson, E. L.; Schmidt, P. W.; Lodge, T. P.; Hillmyer, M. A.; Bühlmann, P. Self-Supporting, Hydrophobic, Ionic Liquid-Based Reference Electrodes Prepared by Polymerization-Induced Microphase Separation. *ACS Sensors* **2017**, *2*, 1498–1504.

(77) Ueki, T.; Watanabe, M. Polymers in Ionic Liquids: Dawn of Neoteric Solvents and Innovative Materials. *Bull. Chem. Soc. Jpn.* **2012**, *85*, 33–50.

(78) Lee, H.-N.; Lodge, T. P. Lower Critical Solution Temperature (LCST) Phase Behavior of Poly(ethylene oxide) in Ionic Liquids. *J. Phys. Chem. Lett.* **2010**, *1*, 1962–1966.

(79) Freire, M. G.; Santos, L. M. N. B. F.; Fernandes, A. M.; Coutinho, J. A. P.; Marrucho, I. M. An Overview of the Mutual Solubilities of Water–imidazolium-Based Ionic Liquids Systems. *Fluid Phase Equilib.* **2007**, *261*, 449–454.

(80) Swatloski, R. P.; Spear, S. K.; Holbrey, J. D.; Rogers, R. D. Dissolution of Cellose with Ionic Liquids. *J. Am. Chem. Soc.* **2002**, *124*, 4974–4975.

(81) Kakiuchi, T.; Yoshimatsu, T.; Nishi, N. New Class of Ag/AgCl Electrodes Based on Hydrophobic Ionic Liquid Saturated with AgCl. *Anal. Chem.* **2007**, *79*, 7187–7191.

(82) Seki, S.; Susan, M. A. B. H.; Kaneko, T.; Tokuda, H.; Noda, A.; Watanabe, M. Distinct Difference in Ionic Transport Behavior in Polymer Electrolytes Depending on the Matrix Polymers and Incorporated Salts. *J. Phys. Chem. B* **2005**, *109*, 3886–3892.

(83) Tang, B.; White, S. P.; Frisbie, C. D.; Lodge, T. P. Synergistic Increase in Ionic Conductivity and Modulus of Triblock Copolymer Ion Gels. *Macromolecules* **2015**, *48*, 4942–4950.

(84) Hirotsu, S.; Hirokawa, Y.; Tanaka, T. Volume-phase Transitions of Ionized *N*-isopropylacrylamide Gels. *J. Chem. Phys.* **1987**, *87*, 1392–1395.

(85) Holbrey, J. D.; Reichert, W. M.; Nieuwenhuyzen, M.; Sheppard, O.; Hardacre, C.; Rogers, R. D. Liquid Clathrate Formation in Ionic Liquid–aromatic Mixtures. *Chem. Commun.* **2003**, *1*, 476–477.

(86) Ueki, T.; Yamaguchi, A.; Ito, N.; Kodama, K.; Sakamoto, J.; Ueno, K.; Kokubo, H.; Watanabe, M. Photoisomerization-Induced Tunable LCST Phase Separation of Azobenzene-Containing Polymers in an Ionic Liquid. *Langmuir* **2009**, *25*, 8845–8848.

(87) Hayamizu, K.; Akiba, E.; Bando, T.; Aihara, Y. Nuclear Magnetic Resonance and Ionic Conductivity Studies for Liquid Electrolytes Composed of Glymes and Polyetheneglycol Dimethyl Ethers. *J. Chem. Phys.* **2002**, *117*, 5929–5939.

(88) Doyle, M.; Fuller, T. F.; Newman, J. The Importance of the Lithium Ion Transference Number in Lithium/polymer Cells. *Electrochim. Acta* **1994**, *39*, 2073–2081.

(89) Thomas, K. E.; Sloop, S. E.; Newman, J. Comparison of Lithium-Polymer Cell Performance with Unity and Nonunity Transference Numbers. *J. Power Sources* **2000**, *89*, 132–138.

(90) Villaluenga, I.; Inceoglu, S.; Jiang, X.; Chen, X. C.; Chintapalli, M.; Wang, D. R.; Devaux, D.; Balsara, N. P. Nanostructured Single-Ion-Conducting Hybrid Electrolytes Based on Salty Nanoparticles and Block Copolymers. *Macromolecules* **2017**, *50*, 1998–2005.

(91) Zawodzinski, T. A. Water Uptake by and Transport Through Nafion® 117 Membranes. *J. Electrochem. Soc.* **1993**, *140*, 1041–1047.

(92) Singh, M.; Odusanya, O.; Wilmes, G. M.; Eitouni, H. B.; Gomez, E. D.; Patel, A. J.; Chen, V. L.; Park, M. J. J.; Fragouli, P.; Iatrou, H.; Hadjichristidis, N.; Cookson, D.; Balsara, N. P. Effect of Molecular Weight on the Mechanical and Electrical Properties of Block Copolymer Electrolytes. *Macromolecules* **2007**, *40*, 4578–4585.

(93) Young, W.-S.; Epps, T. H., III. Ionic Conductivities of Block Copolymer Electrolytes with Various Conducting Pathways: Sample Preparation and Processing Considerations. *Macromolecules* **2012**, *45*, 4689–4697.

(94) Park, M. J.; Balsara, N. P. Anisotropic Proton Conduction in Aligned Block Copolymer Electrolyte Membranes at Equilibrium with Humid Air. *Macromolecules* **2010**, *43*, 292–298.

(95) He, Y.; Boswell, P. G.; Bühlmann, P.; Lodge, T. P. Ion Gels by Self-Assembly of a Triblock Copolymer in an Ionic Liquid. *J. Phys. Chem. B* **2007**, *111*, 4645–4652.

(96) Bates, F. S.; Fredrickson, G. H. Block Copolymers-Designer Soft Materials. *Phys. Today* **1999**, *52*, 32–38.

(97) Matsen, M. W. The Standard Gaussian Model for Block Copolymer Melts. *J. Phys. Condens. Matter* **2002**, *14*, R21–R47.

(98) Lee, S.; Bluemle, M. J.; Bates, F. S. Discovery of a Frank-Kasper Sigma Phase in Sphere-Forming Block Copolymer Melts. *Science* **2010**, *330*, 349–353.

(99) Young, N. P.; Devaux, D.; Khurana, R.; Coates, G. W.; Balsara, N. P. Investigating Polypropylene-Poly(ethylene oxide)-Polypropylene Triblock Copolymers as Solid Polymer Electrolytes for Lithium Batteries. *Solid State Ionics* **2014**, *263*, 87–94.

(100) Khurana, R.; Schaefer, J. L.; Archer, L. A.; Coates, G. W. Suppression of Lithium Dendrite Growth Using Cross-Linked Polyethylene/poly(ethylene oxide) Electrolytes: A New Approach for Practical Lithium-Metal Polymer Batteries. *J. Am. Chem. Soc.* **2014**, *136*, 7395–7402.

(101) Villaluenga, I.; Chen, X. C.; Devaux, D.; Hallinan, D. T.; Balsara, N. P. Nanoparticle-Driven Assembly of Highly Conducting Hybrid Block Copolymer Electrolytes. *Macromolecules* **2015**, *48*, 358–364.

(102) Bouchet, R.; Phan, T. N. T.; Beaudoin, E.; Devaux, D.; Davidson, P.; Bertin, D.; Denoyel, R. Charge Transport in Nanostructured PS–PEO–PS Triblock Copolymer Electrolytes. *Macromolecules* **2014**, *47*, 2659–2665.

(103) Young, W.-S.; Epps, T. H., III. Salt Doping in PEO-Containing Block Copolymers: Counterion and Concentration Effects. *Macromolecules* **2009**, *42*, 2672–2678.

(104) Kumar, Y.; Hashmi, S. A.; Pandey, G. P. Lithium Ion Transport and Ion-Polymer Interaction in PEO Based Polymer Electrolyte Plasticized with Ionic Liquid. *Solid State Ionics* **2011**, *201*, 73–80.

(105) Kim, S. Y.; Yoon, E.; Joo, T.; Park, M. J. Morphology and Conductivity in Ionic Liquid Incorporated Sulfonated Block Copolymers. *Macromolecules* **2011**, *44*, 5289–5298.

(106) Weber, R. L.; Ye, Y.; Schmitt, A. L.; Banik, S. M.; Elabd, Y. A.; Mahanthappa, M. K. Effect of Nanoscale Morphology on the Conductivity of Polymerized Ionic Liquid Block Copolymers. *Macromolecules* **2011**, *44*, 5727–5735.

(107) Gomez, E. D.; Panday, A.; Feng, E. H.; Chen, V.; Stone, G. M.; Minor, A. M.; Kisielowski, C.; Downing, K. H.; Borodin, O.; Smith, G. D.; Balsara, N. P. Effect of Ion Distribution on Conductivity of Block Copolymer Electrolytes. *Nano Lett.* **2009**, *9*, 1212–1216.

(108) Chintapalli, M.; Chen, X. C.; Thelen, J. L.; Teran, A. A.; Wang, X.; Garetz, B. A.; Balsara, N. P. Effect of Grain Size on the Ionic Conductivity of a Block Copolymer Electrolyte. *Macromolecules* **2014**, *47*, 5424–5431.

(109) Irwin, M. T.; Hickey, R. J.; Xie, S.; Bates, F. S.; Lodge, T. P. Lithium Salt-Induced Microstructure and Ordering in Diblock Copolymer/Homopolymer Blends. *Macromolecules* **2016**, *49*, 4839–4849.

(110) Phillip, W. A.; Amendt, M.; O'Neill, B.; Chen, L.; Hillmyer, M. A.; Cussler, E. L. Diffusion and Flow across Nanoporous Polydicyclopentadiene-Based Membranes. *ACS Appl. Mater. Interfaces* **2009**, *1*, 472–480.

(111) Dair, B. J.; Honeker, C. C.; Alward, D. B.; Avgeropoulos, A.; Hadjichristidis, N.; Fetters, L. J.; Capel, M.; Thomas, E. L. Mechanical Properties and Deformation Behavior of the Double Gyroid Phase in Unoriented Thermoplastic Elastomers.

Macromolecules **1999**, *32*, 8145–8152.

(112) Meuler, A. J.; Hillmyer, M. A.; Bates, F. S. Ordered Network Mesostructures in Block Polymer Materials. *Macromolecules* **2009**, *42*, 7221–7250.

(113) Zhang, S.; Lee, K. H.; Frisbie, C. D.; Lodge, T. P. Ionic Conductivity, Capacitance, and Viscoelastic Properties of Block Copolymer-Based Ion Gels. *Macromolecules* **2011**, *44*, 940–949.

(114) Zhang, S.; Lee, K. H.; Sun, J.; Frisbie, C. D.; Lodge, T. P. Viscoelastic Properties, Ionic Conductivity, and Materials Design Considerations for Poly(styrene-*b*-ethylene oxide-*b*-styrene)-Based Ion Gel Electrolytes. *Macromolecules* **2011**, *44*, 8981–8989.

(115) Bates, F. S. Network Phases in Block Copolymer Melts. *MRS Bull.* **2005**, *30*, 525–532.

(116) Akthakul, A.; Salinaro, R. F.; Mayes, A. M. Antifouling Polymer Membranes with Subnanometer Size Selectivity. *Macromolecules* **2004**, *37*, 7663–7668.

(117) Rolison, D. R. Catalytic Nanoarchitectures-the Importance of Nothing and the Unimportance of Periodicity. *Science* **2003**, *299*, 1698–1701.

(118) Widin, J. M.; Schmitt, A. K.; Schmitt, A. L.; Im, K.; Mahanthappa, M. K. Unexpected Consequences of Block Polydispersity on the Self-Assembly of ABA Triblock Copolymers. *J. Am. Chem. Soc.* **2012**, *134*, 3834–3844.

(119) Widin, J. M.; Schmitt, A. K.; Im, K.; Schmitt, A. L.; Mahanthappa, M. K. Polydispersity-Induced Stabilization of a Disordered Bicontinuous Morphology in ABA Triblock Copolymers. *Macromolecules* **2010**, *43*, 7913–7915.

(120) Bates, F. S.; Maurer, W.; Lodge, T. P.; Schulz, M. F.; Matsen, M. W.; Almdal, K.; Mortensen, K. Isotropic Lifshitz Behavior in Block Copolymer-Homopolymer Blends. *Phys. Rev. Lett.* **1995**, *75*, 4429–4432.

(121) Zhou, N.; Bates, F. S.; Lodge, T. P. Mesoporous Membrane Templated by a Polymeric Bicontinuous Microemulsion. *Nano Lett.* **2006**, *6*, 2354–2357.

(122) Jones, B. H.; Lodge, T. P. High-Temperature Nanoporous Ceramic Monolith Prepared from a Polymeric Bicontinuous Microemulsion Template. *J. Am. Chem. Soc.* **2009**, *131*, 1676–1677.

(123) Panyukov, S.; Rubinstein, M. Stress-Induced Ordering in Microphase-Separated Multicomponent Networks. *Macromolecules* **1996**, *29*, 8220–8230.

(124) Walker, C. N.; Bryson, K. C.; Hayward, R. C.; Tew, G. N. Wide Bicontinuous Compositional Windows from Co-Networks Made with Telechelic Macromonomers. *ACS Nano* **2014**, *8*, 12376–12385.

(125) Rosedale, J. H.; Bates, F. S. Rheology of Ordered and Disordered Symmetric Poly(ethylenepropylene)-Poly(ethylethylene) Diblock Copolymers. *Macromolecules* **1990**, *23*, 2329–2338.

(126) Bates, F. S.; Rosedale, J. H.; Fredrickson, G. H. Fluctuation Effects in a

Symmetric Diblock Copolymer near the Order–disorder Transition. *J. Chem. Phys.* **1990**, *92*, 6255–6270.

(127) Teran, A. A.; Mullin, S. A.; Daniel T. Hallinan, J.; Balsara, N. P. Discontinuous Changes in Ionic Conductivity of a Block Copolymer Electrolyte through an Order–Disorder Transition. *ACS Macro Lett.* **2012**, *1*, 305–309.

(128) Vidil, T.; Hampu, N.; Hillmyer, M. A. Nanoporous Thermosets with Percolating Pores from Block Polymers Chemically Fixed above the Order-Disorder Transition. *ACS Cent. Sci.* **2017**, *3*, 1114–1120.

(129) Wanakule, N. S.; Panday, A.; Mullin, S. a.; Gann, E.; Hexemer, A.; Balsara, N. P. Ionic Conductivity of Block Copolymer Electrolytes in the Vicinity of Order−Disorder and Order−Order Transitions. *Macromolecules* **2009**, *42*, 5642–5651.

(130) Seo, M.; Hillmyer, M. A. Reticulated Nanoporous Polymers by Controlled Polymerization-Induced Microphase Separation. *Science* **2012**, *336*, 1422–1425.

(131) Lee, S.; Gillard, T. M.; Bates, F. S. Fluctuations, Order, and Disorder in Short Diblock Copolymers. *AIChE J.* **2013**, *59*, 3502–3513.

(132) Garcia, B.; Lavallée, S.; Perron, G.; Michot, C.; Armand, M. Room Temperature Molten Salts as Lithium Battery Electrolyte. *Electrochim. Acta* **2004**, *49*, 4583–4588.

(133) Seki, S.; Kobayashi, Y.; Miyashiro, H.; Ohno, Y.; Mita, Y.; Usami, A.; Terada, N.; Watanabe, M. Reversibility of Lithium Secondary Batteries Using a Room-Temperature Ionic Liquid Mixture and Lithium Metal. *Electrochem. Solid-State Lett.* **2005**, *8*, A577–A578.

(134) Doyle, M.; Choi, S. K.; Proulx, G. High-Temperature Proton Conducting Membranes Based on Perfluorinated Ionomer Membrane-Ionic Liquid Composites. *J. Electrochem. Soc.* **2000**, *147*, 34–37.

(135) Xu, W. W.; Angell, C. A. Solvent-Free Electrolytes with Aqueous Solution-Like Conductivities. *Science* **2003**, *302*, 422–425.

(136) Belieres, J.-P.; Angell, C. A. Protic Ionic Liquids: Preparation, Characterization, and Proton Free Energy Level Representation. *J. Phys. Chem. B* **2007**, *111*, 4926–4937.

(137) Lee, S.-Y.; Yasuda, T.; Watanabe, M. Fabrication of Protic Ionic Liquid/sulfonated Polyimide Composite Membranes for Non-Humidified Fuel Cells. *J. Power Sources* **2010**, *195*, 5909–5914.

(138) Lee, J.; Panzer, M. J.; He, Y.; Lodge, T. P.; Frisbie, C. D. Ion Gel Gated Polymer Thin-Film Transistors. *J. Am. Chem. Soc.* **2007**, *129*, 4532–4533.

(139) Singh, B.; Sekhon, S. S. Ion Conducting Behaviour of Polymer Electrolytes Containing Ionic Liquids. *Chem. Phys. Lett.* **2005**, *414*, 34–39.

(140) Gwee, L.; Choi, J.-H.; Winey, K. I.; Elabd, Y. A. Block Copolymer/ionic Liquid Films: The Effect of Ionic Liquid Composition on Morphology and Ion

Conduction. *Polymer* **2010**, *51*, 5516–5524.

(141) Miranda, D. F.; Russell, T. P.; Watkins, J. J. Ordering in Mixtures of a Triblock Copolymer with a Room Temperature Ionic Liquid. *Macromolecules* **2010**, *43*, 10528–10535.

(142) Simone, P. M.; Lodge, T. P. Phase Behavior and Ionic Conductivity of Concentrated Solutions of Polystyrene-Poly(ethylene oxide) Diblock Copolymers in an Ionic Liquid. *ACS Appl. Mater. Interfaces* **2009**, *1*, 2812–2820.

(143) Virgili, J. M.; Hexemer, A.; Pople, J. A.; Balsara, N. P.; Segalman, R. A. Phase Behavior of Polystyrene- Block -poly(2-Vinylpyridine) Copolymers in a Selective Ionic Liquid Solvent. *Macromolecules* **2009**, *42*, 4604–4613.

(144) Wanakule, N. S.; Virgili, J. M.; Teran, A. A.; Wang, Z.-G.; Balsara, N. P. Thermodynamic Properties of Block Copolymer Electrolytes Containing Imidazolium and Lithium Salts. *Macromolecules* **2010**, *43*, 8282–8289.

(145) Wilkes, J. S. A Short History of Ionic Liquids—from Molten Salts to Neoteric Solvents. *Green Chem.* **2002**, *4*, 73–80.

(146) Hoarfrost, M. L.; Tyagi, M.; Segalman, R. A.; Reimer, J. A. Proton Hopping and Long-Range Transport in the Protic Ionic Liquid [Im][TFSI], Probed by Pulsed-Field Gradient NMR and Quasi-Elastic Neutron Scattering. *J. Phys. Chem. B* **2012**, *116*, 8201–8209.

(147) Susan, M. A. B. H.; Noda, A.; Mitsushima, S.; Watanabe, M. Brønsted Acid-Base Ionic Liquids and Their Use as New Materials for Anhydrous Proton Conductors. *Chem. Commun.* **2003**, *8*, 938–939.

(148) Nakamoto, H.; Watanabe, M. Brønsted Acid-Base Ionic Liquids for Fuel Cell Electrolytes. *Chem. Commun.* **2007**, *24*, 2539–2541.

(149) Yan, F.; Yu, S.; Zhang, X.; Qiu, L.; Chu, F.; You, J.; Lu, J. Enhanced Proton Conduction in Polymer Electrolyte Membranes as Synthesized by Polymerization of Protic Ionic Liquid-Based Microemulsions. *Chem. Mater.* **2009**, *21*, 1480–1484.

(150) Tang, Q.; Wu, J.; Tang, Z.; Li, Y.; Lin, J. High-Temperature Proton Exchange Membranes from Ionic Liquid Absorbed/doped Superabsorbents. *J. Mater. Chem.* **2012**, *22*, 15836–15844.

(151) Hoarfrost, M. L.; Tyagi, M. S.; Segalman, R. A.; Reimer, J. A. Effect of Confinement on Proton Transport Mechanisms in Block Copolymer/ionic Liquid Membranes. *Macromolecules* **2012**, *45*, 3112–3120.

(152) Wu, W.; Li, Y.; Chen, P.; Liu, J.; Wang, J.; Zhang, H. Constructing Ionic Liquid-Filled Proton Transfer Channels within Nanocomposite Membrane by Using Functionalized Graphene Oxide. *ACS Appl. Mater. Interfaces* **2016**, *8*, 588–599.

(153) Weber, R. L.; Ye, Y.; Banik, S. M.; Elabd, Y. A.; Hickner, M. A.; Mahanthappa, M. K. Thermal and Ion Transport Properties of Hydrophilic and Hydrophobic Polymerized Styrenic Imidazolium Ionic Liquids. *J. Polym. Sci. Part B Polym. Phys.* **2011**, *49*, 1287–1296.

(154) Price, S. C.; Ren, X.; Jackson, A. C.; Ye, Y.; Elabd, Y. A.; Beyer, F. L. Bicontinuous Alkaline Fuel Cell Membranes from Strongly Self-Segregating Block Copolymers. *Macromolecules* **2013**, *46*, 7332–7340.

(155) McIntosh, L. D.; Schulze, M. W.; Irwin, M. T.; Hillmyer, M. A.; Lodge, T. P. Evolution of Morphology, Modulus, and Conductivity in Polymer Electrolytes Prepared via Polymerization-Induced Phase Separation. *Macromolecules* **2015**, *48*, 1418–1428.

(156) Lai, J. T.; Filla, D.; Shea, R. Functional Polymers from Novel Carboxyl-Terminated Trithiocarbonates as Highly Efficient RAFT Agents. *Macromolecules* **2002**, *35*, 6754–6756.

(157) Mao, H.; Hillmyer, M. A. Nanoporous Polystyrene by Chemical Etching of Poly(ethylene oxide) from Ordered Block Copolymers. *Macromolecules* **2005**, *38*, 4038–4039.

(158) Wu, D.; Chen, A.; Johnson, C. S. An Improved Diffusion Ordered Spectroscopy Experiment Incorporating Bipolar Gradient Pulses. *J. Magn. Reson.* **1995**, *115*, 260–264.

(159) Lodge, T. P.; Pudil, B.; Hanley, K. J. The Full Phase Behavior for Block Copolymers in Solvents of Varying Selectivity. *Macromolecules* **2002**, *35*, 4707–4717.

(160) Milhaupt, J. M.; Lodge, T. P. Homopolymer and Small-molecule Tracer Diffusion in a Gyroid Matrix. *J. Polym. Sci. Part B Polym. Phys.* **2001**, *39*, 843–859.

(161) Chen, L.; Phillip, W. A; Cussler, E. L.; Hillmyer, M. A. Robust Nanoporous Membranes Templated by a Doubly Reactive Block Copolymer. *J. Am. Chem. Soc.* **2007**, *129*, 13786–13787.

(162) Gido, S. P.; Thomas, E. L. Lamellar Diblock Copolymer Grain Boundary Morphology. 4 . Tilt Boundaries. *Macromolecules* **1994**, *27*, 6137–6144.

(163) Zhang, H.; Wu, W.; Wang, J.; Zhang, T.; Shi, B.; Liu, J.; Cao, S. Enhanced Anhydrous Proton Conductivity of Polymer Electrolyte Membrane Enabled by Facile Ionic Liquid-Based Hoping Pathways. *J. Memb. Sci.* **2015**, *476*, 136–147.

(164) Rey, I.; Johansson, P.; Lindgren, J.; Lasse, J. C.; Lassègues, J. C.; Grondin, J.; Servant, L. Spectroscopic and Theoretical Study of Bis(trifluoromethane)sulfonimide. *J. Phys. Chem. A* **1998**, *102*, 3249–3258.

(165) Noda, A.; Hayamizu, K.; Watanabe, M. Pulsed-Gradient Spin - Echo ^{1}H and ^{19}F NMR Ionic Diffusion Coefficient , Viscosity , and Ionic Conductivity of Non-Chloroaluminate Room-Temperature Ionic Liquids. *J. Phys. Chem. B* **2001**, *105*, 4603–4610.

(166) Simone, P. M.; Lodge, T. P. Lyotropic Phase Behavior of Polybutadiene−Poly(ethylene oxide) Diblock Copolymers in Ionic Liquids. *Macromolecules* **2008**, *41*, 1753–1759.

(167) Williams, M. L.; Landel, R. F.; Ferry, J. D. The Temperature Dependence of Relaxation Mechanisms in Amorphous Polymers and Other Glass-Forming

Liquids. *J. Am. Chem. Soc.* **1955**, *77*, 3701–3707.

(168) Jones, G.; McGhie, A.; Farrington, G. Studies of the Stability of Poly (ethylene oxide) and PEO-Based Solid Electrolytes Using Thermogravimetry-Mass Spectrometry. *Macromolecules* **1991**, *24*, 3285–3290.

(169) Susan, M. A. B. H.; Kaneko, T.; Noda, A.; Watanabe, M. Ion Gels Prepared by in Situ Radical Polymerization of Vinyl Monomers in an Ionic Liquid and Their Characterization as Polymer Electrolytes. *J. Am. Chem. Soc.* **2005**, *127*, 4976–4983.

(170) Gido, S. P.; Gunther, J.; Thomas, E. L.; Hoffman, D. Lamellar Diblock Copolymer Grain Boundary Morphology. 1. Twist Boundary Characterization. *Macromolecules* **1993**, *26*, 4506–4520.

(171) Majewski, P. W.; Gopinadhan, M.; Jang, W. S.; Lutkenhaus, J. L.; Osuji, C. O.; Chinedum, O. Anisotropic Ionic Conductivity in Block Copolymer Membranes by Magnetic Field Alignment. *J. Am. Chem. Soc.* **2010**, *132*, 17516–17522.

(172) Chopade, S. A.; So, S.; Hillmyer, M. A.; Lodge, T. P. Anhydrous Proton Conducting Polymer Electrolyte Membranes via Polymerization-Induced Microphase Separation. *ACS Appl. Mater. Interfaces* **2016**, *8*, 6200–6210.

(173) Huang, P.; Zhu, L.; Cheng, S. Z. D.; Ge, Q.; Quirk, R. P.; Thomas, E. L.; Lotz, B.; Hsiao, B. S.; Liu, L.; Yeh, F. Crystal Orientation Changes in Two-Dimensionally Confined Nanocylinders in a Poly(ethylene oxide)-B-polystyrene/Polystyrene Blend. *Macromolecules* **2001**, *34*, 6649–6657.

(174) Berthier, C.; Gorecki, W.; Minier, M.; Armand, M. B.; Chabagno, J. M.; Rigaud, P. Microscopic Investigation of Ionic Conductivity in Alkali Metal Salts-Poly(ethylene oxide) Adducts. *Solid State Ionics* **1983**, *11*, 91–95.

(175) Wang, L.; Li, N.; He, X.; Wan, C.; Jiang, C. Macromolecule Plasticized Interpenetrating Structure Solid State Polymer Electrolyte for Lithium Ion Batteries. *Electrochim. Acta* **2012**, *68*, 214–219.

(176) Fan, L. Z.; Hu, Y. S.; Bhattacharyya, A. J.; Maier, J. Succinonitrile as a Versatile Additive for Polymer Electrolytes. *Adv. Funct. Mater.* **2007**, *17*, 2800–2807.

(177) Kakihana, M.; Schantz, S.; Torell, L. M. Raman Spectroscopic Study of Ion–ion Interaction and Its Temperature Dependence in a Poly(propylene-oxide)ased $NaCF_3SO_3$ –polymer electrolyte. *J. Chem. Phys.* **1990**, *92*, 6271–6277.

(178) Alarco, P.-J.; Abu-Lebdeh, Y.; Abouimrane, A.; Armand, M. The Plastic-Crystalline Phase of Succinonitrile as a Universal Matrix for Solid-State Ionic Conductors. *Nat. Mater.* **2004**, *3*, 476–481.

(179) Choi, K. H.; Cho, S. J.; Kim, S. H.; Kwon, Y. H.; Kim, J. Y.; Lee, S. Y. Thin, Deformable, and Safety-Reinforced Plastic Crystal Polymer Electrolytes for High-Performance Flexible Lithium-Ion Batteries. *Adv. Funct. Mater.* **2014**, *24*, 44–52.

(180) Fan, L. Z.; Wang, X. L.; Long, F. All-Solid-State Polymer Electrolyte with Plastic Crystal Materials for Rechargeable Lithium-Ion Battery. *J. Power Sources* **2009**, *189*, 775–778.

(181) Kim, G.-Y.; Petibon, R.; Dahn, J. R. Effects of Succinonitrile (SN) as an Electrolyte Additive on the Impedance of $LiCoO_2$/Graphite Pouch Cells during Cycling. *J. Electrochem. Soc.* **2014**, *161*, A506–A512.

(182) Kim, Y.-S.; Kim, T.-H.; Lee, H.; Song, H.-K. Electronegativity-Induced Enhancement of Thermal Stability by Succinonitrile as an Additive for Li Ion Batteries. *Energy Environ. Sci.* **2011**, *4*, 4038–4045.

(183) Gutmann, V. *The Donor-Acceptor Approach to Molecular Interactions*; Plenum Press: New York , 1978.

(184) Yue, R.; Niu, Y.; Wang, Z.; Douglas, J. F.; Zhu, X.; Chen, E. Suppression of Crystallization in a Plastic Crystal Electrolyte (SN/$LiClO_4$) by a Polymeric Additive (Polyethylene Oxide) for Battery Applications. *Polymer* **2009**, *50*, 1288–1296.

(185) Wu, H.; Wick, C. D. Computational Investigation on the Role of Plasticizers on Ion Conductivity in Poly(ethylene oxide) LiTFSI Electrolytes. *Macromolecules* **2010**, *43*, 3502–3510.

(186) Kono, M.; Hayashi, E.; Watanabe, M. Network Polymer Electrolytes with Free Chain Ends as Internal Plasticizer. *J. Electrochem. Soc.* **1998**, *145*, 1521–1527.

(187) Echeverri, M.; Kim, N.; Kyu, T. Ionic Conductivity in Relation to Ternary Phase Diagram of Poly(ethylene oxide), Succinonitrile, and Lithium Bis(trifluoromethane)sulfonimide Blends. *Macromolecules* **2012**, *45*, 6068–6077.

(188) Park, M. J.; Choi, I.; Hong, J.; Kim, O. Polymer Electrolytes Integrated with Ionic Liquids for Future Electrochemical Devices. *J. Appl. Polym. Sci.* **2013**, *129*, 2363–2376.

(189) Lodge, T. P.; Ueki, T. Mechanically Tunable, Readily Processable Ion Gels by Self-Assembly of Block Copolymers in Ionic Liquids. *Acc. Chem. Res.* **2016**, *49*, 2107–2114.

(190) Cho, J. H.; Lee, J.; Xia, Y.; Kim, B.; He, Y.; Renn, M. J.; Lodge, T. P.; Frisbie, C. D.; Daniel Frisbie, C. Printable Ion-Gel Gate Dielectrics for Low-Voltage Polymer Thin-Film Transistors on Plastic. *Nat. Mater.* **2008**, *7*, 900–906.

(191) Gu, Y.; Lodge, T. P. Synthesis and Gas Separation Performance of Triblock Copolymer Ion Gels with a Polymerized Ionic Liquid Mid-Block. *Macromolecules* **2011**, *44*, 1732–1736.

(192) Inzelt, G.; Lewenstam, A.; Scholz, F. *Handbook of Reference Electrodes*; Springer: Heidelberg, Germany, 2013.

(193) Kakiuchi, T.; Tsujioka, N.; Kurita, S.; Iwami, Y. Phase-Boundary Potential across the Nonpolarized Interface between the Room-Temperature Molten Salt and Water. *Electrochem. commun.* **2003**, *5*, 159–164.

(194) Zhang, T.; Lai, C.-Z.; Fierke, M. A.; Stein, A.; Bühlmann, P. Advantages and Limitations of Reference Electrodes with an Ionic Liquid Junction and Three-Dimensionally Ordered Macroporous Carbon as Solid Contact. *Anal. Chem.* **2012**, *84*, 7771–7778.

(195) Sakaida, H.; Kakiuchi, T. Determination of Single-Ion Activities of H^+ and Cl^- in Aqueous Hydrochloric Acid Solutions by Use of an Ionic Liquid Salt Bridge. *J. Phys. Chem. B* **2011**, *115*, 13222–13226.

(196) Kakiuchi, T.; Yoshimatsu, T. A New Salt Bridge Based on the Hydrophobic Room-Temperature Molten Salt. *Bull. Chem. Soc. Jpn.* **2006**, *79*, 1017–1024.

(197) Cicmil, D.; Anastasova, S.; Kavanagh, A.; Diamond, D.; Mattinen, U.; Bobacka, J.; Lewenstam, A.; Radu, A. Ionic Liquid-Based, Liquid-Junction-Free Reference Electrode. *Electroanalysis* **2011**, *23*, 1881–1890.

(198) Mamińska, R.; Dybko, A.; Wróblewski, W. All-Solid-State Miniaturised Planar Reference Electrodes Based on Ionic Liquids. *Sensors Actuators B Chem.* **2006**, *115*, 552–557.

(199) Zou, X. U.; Chen, L. D.; Lai, C.-Z.; Bühlmann, P. Ionic Liquid Reference Electrodes With a Well-Controlled Co(II)/Co(III) Redox Buffer as Solid Contact. *Electroanalysis* **2015**, *27*, 602–608.

(200) Kudo, Y.; Shibata, M.; Nomura, S.; Ogawa, N. Application of a pH Electrode Incorporating an Ionic Liquid Salt Bridge to the Measurement of Rainwater Samples. *Anal. Sci.* **2017**, *33*, 739–742.

(201) Mousavi, M. P. S.; Bühlmann, P. Reference Electrodes with Salt Bridges Contained in Nanoporous Glass: An Underappreciated Source of Error. *Anal. Chem.* **2013**, *85*, 8895–8901.

(202) Mousavi, M. P. S.; Saba, S. A.; Anderson, E. L.; Hillmyer, M. A.; Bühlmann, P. Avoiding Errors in Electrochemical Measurements: Effect of Frit Material on the Performance of Reference Electrodes with Porous Frit Junctions. *Anal. Chem.* **2016**, *88*, 8706–8713.

(203) Zhang, L.; Miyazawa, T.; Kitazumi, Y.; Kakiuchi, T. Ionic Liquid Salt Bridge with Low Solubility of Water and Stable Liquid Junction Potential Based on a Mixture of a Potential-Determining Salt and a Highly Hydrophobic Ionic Liquid. *Anal. Chem.* **2012**, *84*, 3461–3464.

(204) Kakiuchi, T.; Yamamoto, M. Current Stage and Perspectives of pH Measurements by Use of Ionic Liquid Salt Bridge. *Bunseki kagaku* **2016**, *65*, 181–191.

(205) Saba, S. A.; Mousavi, M. P. S. S.; Bühlmann, P.; Hillmyer, M. A. Hierarchically Porous Polymer Monoliths by Combining Controlled Macro- and Microphase Separation. *J. Am. Chem. Soc.* **2015**, *137*, 8896–8899.

(206) Chopade, S. A.; Au, J. G.; Li, Z.; Schmidt, P. W.; Hillmyer, M. A.; Lodge, T. P. Robust Polymer Electrolyte Membranes with High Ambient-Temperature Lithium-Ion Conductivity via Polymerization-Induced Microphase Separation. *ACS Appl. Mater. Interfaces* **2017**, *9*, 14561–14565.

(207) Dohner, R. E.; Wegmann, D.; Morf, W. E.; Simon, W. Reference Electrode with Free-Flowing Free-Diffusion Liquid Junction. *Anal. Chem.* **1986**, *58*, 2585–2589.

(208) Meier, P. C. Two-Parameter Debye-Hückel Approximation for the Evaluation of Mean Activity Coefficients of 109 Electrolytes. *Anal. Chim. Acta* **1982**, *136*, 363–

368.

(209) Anderson, E. L.; Bühlmann, P. Electrochemical Impedance Spectroscopy of Ion-Selective Membranes: Artifacts in Two-, Three-, and Four-Electrode Measurements. *Anal. Chem.* **2016**, *88*, 9738–9745.

(210) Simone, P. M.; Lodge, T. P. Micellization of PS-PMMA Diblock Copolymers in an Ionic Liquid. *Macromol. Chem. Phys.* **2007**, *208*, 339–348.

(211) Bakker, E.; Bühlmann, P.; Pretsch, E. The Phase-Boundary Potential Model. *Talanta* **2004**, *63*, 3–20.

(212) Fukushima, T.; Asaka, K.; Kosaka, A.; Aida, T. Fully Plastic Actuator through Layer-by-Layer Casting with Ionic-Liquid-Based Bucky Gel. *Angew. Chemie* **2005**, *117*, 621–629.

(213) Carey, J. L.; Whitcomb, D. R.; Chen, S.; Penn, R. L.; Bühlmann, P. Potentiometric *in Situ* Monitoring of Anions in the Synthesis of Copper and Silver Nanoparticles Using the Polyol Process. *ACS Nano* **2015**, *9*, 12104–12114.

(214) Lugert-Thom, E. C.; Gladysz, J. A.; Rábai, J.; Bühlmann, P. Cleaning of pH Selective Electrodes with Ionophore-Doped Fluorous Membranes in NaOH Solution at 90 °C. *Electroanalysis* **2018**, *30*, 611–618.

(215) Bakker, E. Can Calibration-Free Sensors Be Realized? *ACS Sensors* **2016**, *1*, 838–841.

(216) Patel, S. N.; Javier, A. E.; Balsara, N. P. Electrochemically Oxidized Electronic and Ionic Conducting Nanostructured Block Copolymers for Lithium Battery Electrodes. *ACS Nano* **2013**, *7*, 6056–6068.

Appendix

A. Phosphoric Acid PIMS PEMs

This section describes preparation and characterization of P2VP-phosphoric acid (PA) PEMs. Characterization of the PEMs, including ionic conductivity measurements, SAXS, and TEM studies, were performed following the procedures detailed in Chapter 2.

P2VP-CTA synthesis

Poly(2-vinylpyridine) macro chain-transfer agent (P2VP-CTA) was synthesized from the reversible addition-fragmentation chain-transfer (RAFT) chain transfer agent *S*-dodecyl-*S*′-(*α*,*α*′-dimethyl-*α*′′-acetic acid) trithiocarbonate (DDMAT) (Figure A.1). 2VP (30 g, 0.285 mol, filtered through activated basic alumina to remove inhibitor), DDMAT (600 mg, 0.148 mmol), and 2,2′-azobisisobutyronitrile (AIBN, 10.4 mg, 0.04 mmol) were dissolved in 85 g mixture of toluene and ethanol (3:2 w/w) in a Schlenk flask. The reaction mixture was degassed in three freeze-pump-thaw cycles and placed in an oil bath at 70 °C. After 24 h, the reaction flask was removed from the heat and the reaction stopped by cooling in an ice bath and opening the flask to the atmosphere. The polymer was then precipitated twice from hexanes and collected via filtration, yielding the P2VP macro-CTA as a yellowish powder. SEC: M_n = 10 kg/mol, $Đ$ = 1.05. The macro-CTA exhibited $T_g \approx$ 72 °C (Figure A.2) and $T_d \approx$ 310 °C (Figure A.3).

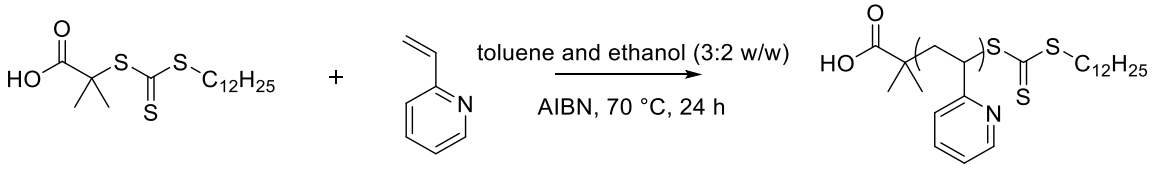

Figure A.1: Synthesis of macro-chain transfer agent P2VP-CTA

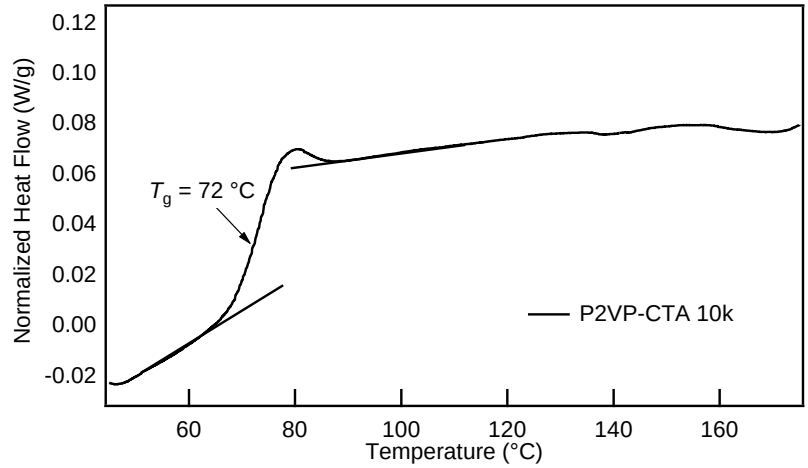

Figure A.2: DSC thermograms for P2VP-CTA

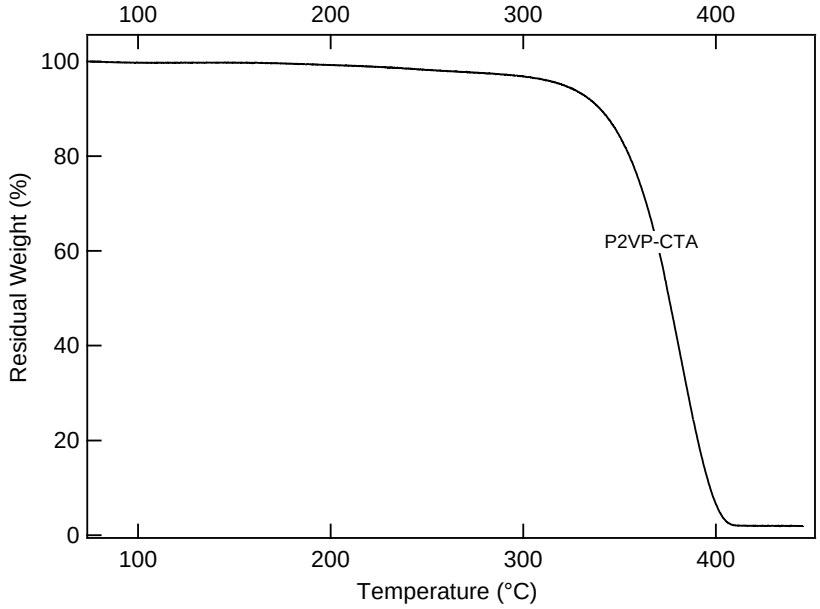

Figure A.3: Thermogravimetric curves under nitrogen of the P2VP-CTA

Preparation of IL PIMS PEMs

IL PEMs were prepared following the procedures in Section 2.2. Briefly, reaction mixtures were prepared gravimetrically, typically containing 32 wt % P2VP-CTA in a 4:1 molar mixture of styrene to divinylbenzene. A varying amount of IL [HEIm][TFSI] was added to this reaction solution to achieve a 0–35 overall wt% IL concentration in the resultant PEM. Cross-linked P2VP monoliths (no IL) are thermally stable up to 350 °C, similar to PEO-based cross-linked monoliths studied in Chapter 2 (Figure A.4a). P2VP PEM with 25 wt% exhibit two-step thermal degradation (Figure A.4b). Unlike PEO PEMs that exhibit accelerated degradation in the presence of protic IL, the polymeric matrix of P2VP PEMs is thermally stable up to 350 °C. The second step in the TGA profile corresponds to the thermal degradation of the IL.

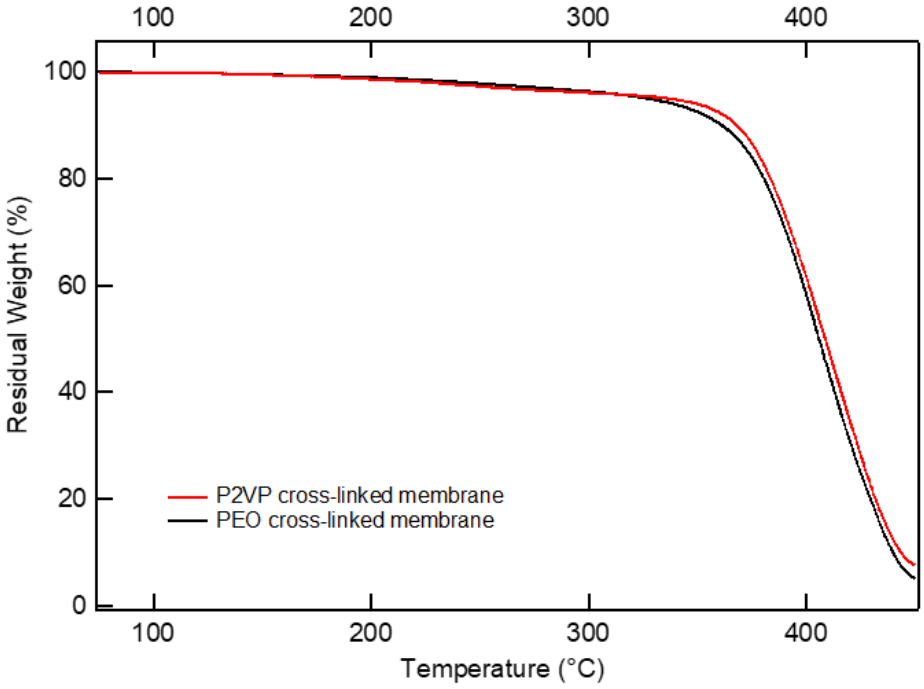

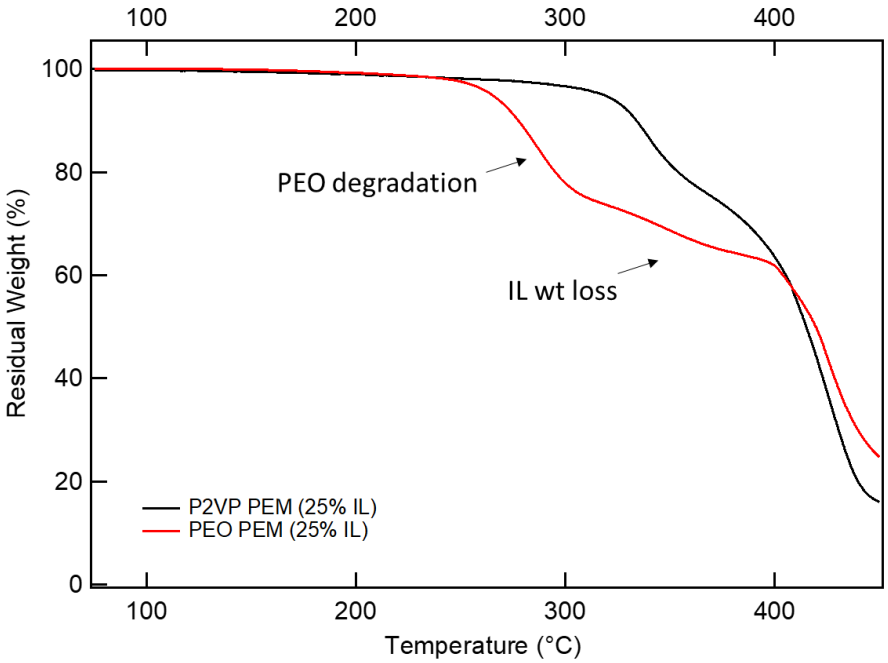

Figure A.4: (a) Thermogravimetric curves under nitrogen of the cross-linked PEMs (no IL). (b) P2VP and PEO IL PEMs (IL content 25 wt%). The first degradation step corresponds to loss of PEO/P2VP macro-CTA.

Morphological Characterization of P2VP-IL PEMs

Small-angle X-ray scattering (SAXS) profiles as shown in Figure A.5a exhibit a broad principal scattering peak at q^* and a weak higher order shoulder at approximately $2q^*$, characteristic of a structured morphology with microphase separated domains, but without long-range periodic order. Thus the observed morphology is consistent with other PIMS PEMs studied in Chapters 2, 3, and 4. The SAXS profiles indicate that the characteristic length scale between the P2VP/IL and P(S-*co*-DVB) domains is 22 – 34 nm. On increasing the IL concentration in the PEM, an increase in the average domain spacing between the conducting phase and the cross-linked PS phase was observed, consistent with selective swelling of the P2VP domains by the IL and increasing chain stretching at the (P2VP+IL)/P(S-*co*-DVB) interface to reduce the unfavorable interactions.[142,159]

A transmission electron microscopy (TEM) image (Figure A.5b) of P2VP-IL PEM (25 wt% IL) reveals a disordered structure, corroborating the SAXS results. The conducting P2VP + IL phase appears dark in the image due to preferential iodine staining of the imidazolium cation.[173] The TEM image depicts a disordered percolating network structure.

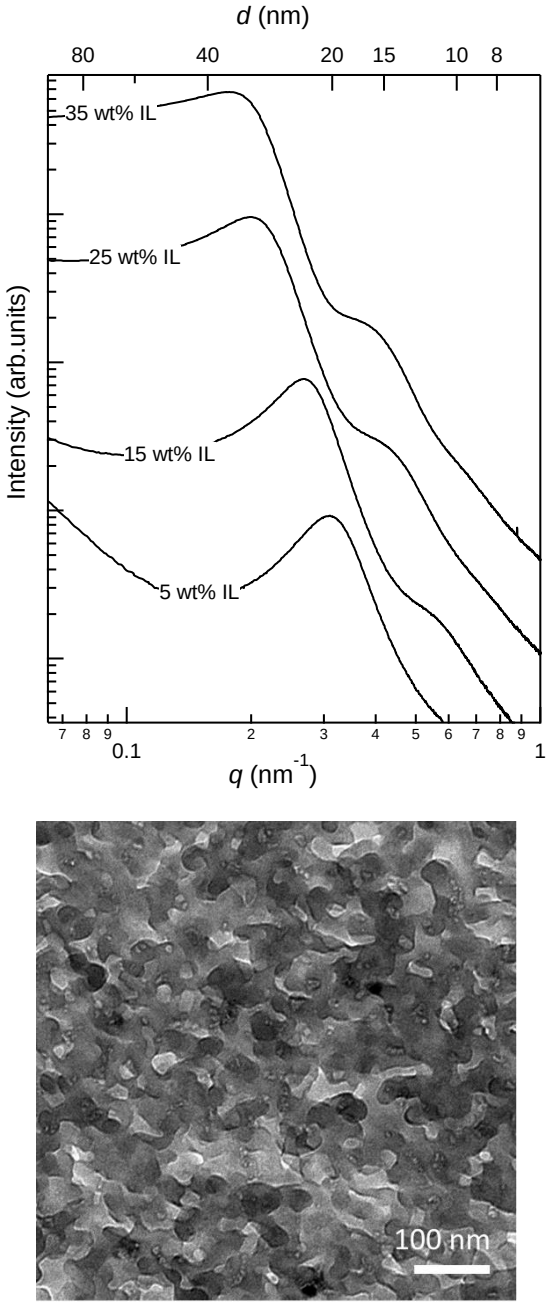

Figure A.5: (a) Small angle X-ray scattering for PIMS PEM samples prepared with 10 kg/mol P2VP-CTA and varying protic IL [HEIm][TFSI] content. The length scale of

compositional heterogeneities increases with IL content (reported as overall wt %). (b) TEM micrograph of P2VP-IL PEM (25 wt% IL) after iodine staining. The IL-P2VP domain appears dark after staining with iodine.

Ionic Conductivity

Figure A.6 summarizes the ionic conductivity of P2VP-IL PEMs in comparison to the protic IL.

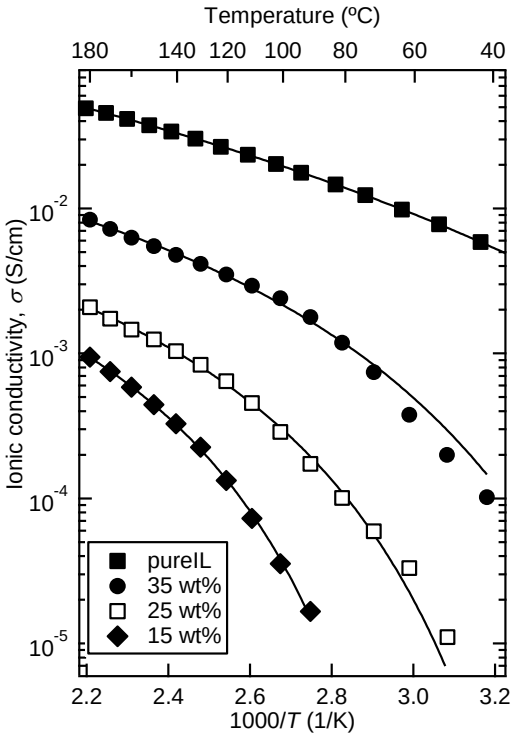

Figure A.6: Ionic conductivity of P2VP-IL PEM samples with varying content of the protic IL, [HEIm][TFSI] (reported as overall wt %). Solid lines are fits to the VFT functional form. The IL conductivity (■) of pure [HEIm][TFSI] is also shown for reference.

Preparation of PA PIMS PEMs

PA-PIMS PEMs were prepared as per the protocol shown in Figure A.5. IL was removed by washing the IL-PEMs with water/methanol mixture several times. IL-PEMs were soaked in a large excess of water/methanol mixture (≈ 40 mL for 0.5 g PEM) for 72 h, during which the water/methanol mixture was changed every 24 h. IL removal was confirmed by gravimetric analysis. The porous PEMs were then immersed in concentrated

PA aqueous solution (≥85 wt%). PA content in the PEMs depended on several factors such as concentration of the doping PA solution, temperature, and doping time.[17] Table A.1 lists the composition of the PA PEMs and the corresponding IL-PEMs used for preparation. It should be noted that neat P2VP cross-linked monoliths (no IL) typically uptake just 4 wt% PA, presumably due to the restriction on volume expansion imposed by the chemically cross-linked PS framework.

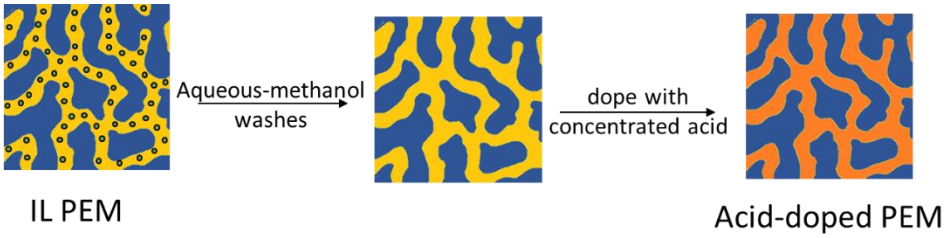

Figure A.7: Preparation of PA PIMS PEMs. The proposed strategy involves removing the IL from PEMs and then swelling them with phosphoric acid.

Table A.1: Composition of P2VP-IL PEMs and corresponding P2VP-PA PEMs

P2VP-IL PEM IL content (wt%)	P2VP-PA PEM Acid loading (wt%)
No IL	4
5	13
25	30 (average over 3 samples)
35	45

Figure A.8a compares the conductivity of the PA-PEM (45 wt% PA) with that of bulk protic IL and IL-PEM (35 wt% IL). PA-PEM exhibits 3 times higher conductivity than its IL counterpart. Proton transport in PA-PEMs prominently occurs via a fast Grotthuss mechanism, whereas vehicular transport of the $HEIm^+$ contributes to proton conductivity of IL-PEMs.[19] In addition, t^+ in PA-PEMs is expected to be ≈ 0.98,[16] thus it exhibits even higher proton conductivity compared to IL-PEMs where $t^+ \approx 0.65$.[172]

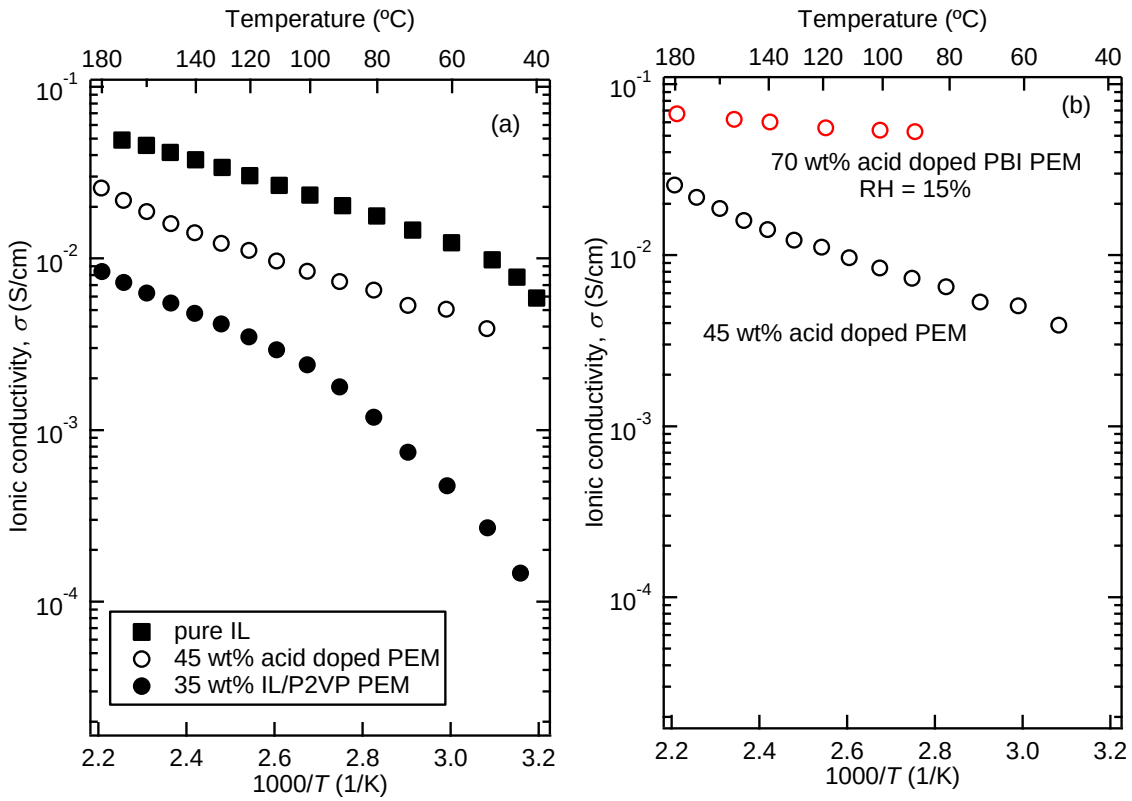

Figure A.8: (a) Ionic conductivity of bulk protic IL [HEIm][TFSI], P2VP/PA-PIMS PEMs, and P2VP IL-PEMs. (b) Comparison of ionic conductivity observed in PBI/PA membranes (RH = 15%)[16] and PA-PIMS PEMs measured under anhydrous conditions.

However, ionic conductivity of the proof-of-concept PA-PEM (45 wt% PA) still falls short of PBI-PA membranes (70 wt% PA), about 3 times lower at 200 °C (Figure A.8b). PBI-PA membranes typically have high acid loading (> 65% w/w).[17] Figure A.8b shows conductivity of a 70 wt% acid doped membrane. In the case of PA-PIMS PEMs, highest acid content achieved was 45 wt%. At higher acid loadings (> 45 wt%), acid leakage was observed. It should also be noted that the reported conductivity measurements for PBI-PA membranes were performed at relative humidity (RH) = 15%, whereas PA-PIMS PEMs conductivity experiments were conducted under anhydrous conditions.